


Winter 2000

# Detection and Modeling of Radiation Induced Effects in Tissues by Dielectric Spectroscopy

Dorin A. Todor  
*Old Dominion University*

Follow this and additional works at: [https://digitalcommons.odu.edu/physics\\_etds](https://digitalcommons.odu.edu/physics_etds)

 Part of the [Biophysics Commons](#), and the [Radiation Medicine Commons](#)

---

## Recommended Citation

Todor, Dorin A.. "Detection and Modeling of Radiation Induced Effects in Tissues by Dielectric Spectroscopy" (2000). Doctor of Philosophy (PhD), dissertation, Physics, Old Dominion University, DOI: 10.25777/42wg-ap17  
[https://digitalcommons.odu.edu/physics\\_etds/88](https://digitalcommons.odu.edu/physics_etds/88)

This Dissertation is brought to you for free and open access by the Physics at ODU Digital Commons. It has been accepted for inclusion in Physics Theses & Dissertations by an authorized administrator of ODU Digital Commons. For more information, please contact [digitalcommons@odu.edu](mailto:digitalcommons@odu.edu).

**DETECTION AND MODELING OF RADIATION INDUCED EFFECTS  
IN TISSUES BY DIELECTRIC SPECTROSCOPY**

by

Dorin A. Todor

B.S., June 1985, University of Bucharest, Romania

A Dissertation Submitted to the Faculty of Old Dominion University  
in Partial Fulfillment of the Requirement for the Degree of

**DOCTOR OF PHILOSOPHY**

**PHYSICS**

**OLD DOMINION UNIVERSITY**

**December 2000**

 Approved by 

  
Gary E. Copeland (Director)

  
Gail E. Dodge (Member)

  
Raymond K. Wu (Member)

  
Charles E. Hyde-Wright (Member)

  
Frank A. Lattanzio (Member)

  
Linda L. Vahala (Member)

**UMI Number: 9999654**

**UMI<sup>®</sup>**

---

**UMI Microform 9999654**

**Copyright 2001 by Bell & Howell Information and Learning Company.**

**All rights reserved. This microform edition is protected against  
unauthorized copying under Title 17, United States Code.**

---

**Bell & Howell Information and Learning Company  
300 North Zeeb Road  
P.O. Box 1346  
Ann Arbor, MI 48106-1346**

## **ABSTRACT**

### **DETECTION AND MODELING OF RADIATION INDUCED EFFECTS IN TISSUES BY DIELECTRIC SPECTROSCOPY**

**Dorin A. Todor**

**Old Dominion University, 1999**

**Director: Dr. Gary E. Copeland**

The work presented here is applied physics research in the field of radiation treatment. We address the development of a new and innovative method, in vivo and possibly non-invasive, for tumor and healthy tissues control during and after the radiation treatment. The radiation treatment is delivered in an almost standardized manner for particular classes of tumors. The large variance in the individual radiosensitivity of healthy tissues and tumors often leads to local recurrence of neoplastic growth and/or distant metastatic disease which often remains untreated. The method is based on the measurement and analysis of electrical impedance data in the frequency domain from 50 mHz to 1 MHz. The dielectric signature of the tissue carries information about the integrity of the plasma membrane, as well as about the tissue micro-architecture. We present dielectric models for biological materials and correlate their parameters with the subtle changes characterizing oncosis or apoptosis occurring as result of radiation or excision. Five tissue types (blood, kidney, liver, lung and heart) were studied and specific impedance models were created for each of them. Based on these models, analysis of freshly excised tissue and radiation-induced effects in excised tissue was carried out and model parameters extracted. The data we present shows correlation between known mechanisms of cellular death and the delivery of radiation, thus making possible a quantification of the individual response. Further work will be needed in order to correlate early impedance changes with late tissue changes characterizing the side effects of the radiotherapy.

*This thesis is dedicated to my family.*

## ACKNOWLEDGMENTS

It was a real privilege to have worked with so many amazing people in the last five years. I am very thankful to all and each of you for the great gifts I received, whether knowledge, or support, leadership, friendship, generosity or any of their linear combinations.

It is customary to express gratitude to the thesis committee members. I was extremely fortunate to have had in my committee members so much more than what they are supposed to be: I had mentors and collaborators and friends. Gail Dodge was a constant presence in my work, somebody ready to answer any question, to critically review articles, proposals, letters and to always come with a fresh, sharp and thorough view, with tactful suggestions that made my thinking and writing evolve. Her cleverness, focus, and efficiency, together with immeasurable generosity and kindness made her not only a remarkable professor but also a great friend. I am particularly grateful to Raymond Wu, from Virginia Beach General Hospital and Eastern Virginia Medical School. Without his altruism, none of our experiments would have been possible. I learned a great deal from him; he is a dedicated and meticulous scientist and his advice and mentoring, played an important role in my choice to pursue medical physics. Charles Hyde-Wright was one of the very first with which I discussed my idea of using impedance spectroscopy in radiation therapy. His natural curiosity and DaVincian thinking were both guides and tests of my work. In a great extent, my work involved biology and radiation biology. I was privileged to have in Frank Lattanzio from Eastern Virginia Medical School not only an expert that can talk a physicist's language but also, through his experience and suggestions, an active contributor to what our work became. My gratitude goes also to Linda Vahala for accepting to review my thesis and for her promptness. I would like to thank my advisor, Gary Copeland for his willingness to supervise a research somehow peculiar for a regular physics department. Not only did he take a chance that few others would have taken, but he was a constant and subtle presence that only an experienced professor can be. His expertise, sagacity and steady assistance made my work possible.

A good friend, a patient and cultivated interlocutor, Anca Dobrian from EVMS, not only made possible our experiments by making available the tissues we used, but brought new and interesting ideas from which I fully benefited.

I cannot thank enough the people from the company whose generosity made our access to the state of the art equipment, possible. The late engineer Peeter Kark, who first visited the lab and assessed our plans, followed by Brad Barchus and Nigel Evans, are just few of the people from Solartron, Inc., which helped us. Thank you. Also many thanks to Charles Sukenik and Leposava Vuskovic, who, on all occasions, helped us with equipment and good advice.

About four years ago, in an informal discussion with Jim Cox, the chair of our department, I expressed my desire to pursue medical physics research and he recommended that I contact Raymond Wu. The rest is history. I am very grateful, for Jim's continuous guidance and visionary advice.

Even though from far away, I received constant and knowledgeable support from Larisa Cheran (University of Toronto) and Vali Raicu (Kochi Medical School, Japan), to which I am thankful.

A very special thanks goes to our special friends, Walt and Vickie Hooks, who not only acted as our extended, American family, but as a ceaseless source of moral support and generosity. Living abroad, rising children and getting adjusted to another culture (not to mention the many small problems, from cars to taxes) was infinitely easier with your help.

I would also like to thank to Richard Wright for his assistance and good humor. Building parts for experiments, setting up the labs and fixing computers was almost a fun job having Dick always ready to help.

I am thankful to my fellow graduate students, in particular to Laura Marcucci, George Brooks, Trey Truman, Nicolas Tregoures and Rama Balasubramanian, with which I shared good moments, exams and homework, as well as frustrations and gray days.

A big *multumesc mult* (thank you very much) for everything you did, for being with me and for me whenever I needed it the most, goes to Luminita and my children Alina and Horia. Thank you for all the good days and successes we shared.

## TABLE OF CONTENTS

	Page
LIST OF TABLES .....	viii
LIST OF FIGURES.....	ix
 Chapter	
I. INTRODUCTION .....	1
II. IONIZING RADIATION .....	6
The interaction of radiation with matter .....	6
Biological effects of ionizing radiation .....	16
III. DIELECTRIC PROPERTIES OF MATTER. ....	27
Dielectric properties, a practical definition.....	27
The Debye dispersion .....	30
Cole-Cole dispersion.....	31
Non-Debye mechanisms .....	34
Interfacial polarization. The Maxwell-Wagner theory .....	37
Low frequency dispersion.....	50
Cells. An electrochemical perspective.....	54
IV. ELECTRICAL IMPEDANCE SPECTROSCOPY .....	58
Variables accessible by impedance measurements.....	59
The frequency response analysis .....	61
V. EXPERIMENTAL METHOD .....	66
Impedance spectroscopy equipment .....	68
Electrodes and specific problems .....	72
Sample irradiation.....	76



<b>VI. DATA ANALYSIS</b> .....	<b>80</b>
<b>Data validation and fitting</b> .....	<b>80</b>
<b>Data modeling</b> .....	<b>83</b>
<b>Blood</b> .....	<b>87</b>
<b>Kidney</b> .....	<b>103</b>
<b>Liver</b> .....	<b>114</b>
<b>Lung</b> .....	<b>124</b>
<b>Heart</b> .....	<b>136</b>
<b>VII. CONCLUSIONS</b> .....	<b>145</b>
<b>REFERENCES</b> .....	<b>157</b>
<b>APPENDICES</b>	
<b>A. Depth dose distributions for 6 MV photons</b> .....	<b>162</b>
<b>B. Parametric model and tables</b> .....	<b>167</b>
<b>C. Biologic variability study</b> .....	<b>173</b>
<b>VITA</b> .....	<b>178</b>

## LIST OF TABLES

Table	Page
I.     Timing of processes from energy deposition to biological effect.....	14
II.    Timing of processes from energy deposition to biological effect.....	56
III.   Krebbs-bicarbonate free buffer composition.....	67
IV.    Values of the parameters in equivalent circuits from Fig. 41 fitted to data shown in Fig. 43. The two values shown for each parameter correspond to the non-irradiated sample (first) and the irradiated one (second). In bold are the values which differ significantly during irradiation.....	98
V.     Cole model parameters for in vivo muscle tissue impedance measurements .....	137
VI.    The fractional exponents of the power laws describing the dielectric response of kidney tissue at high respectively low frequency. ....	153
VII.   The fractional exponents of the power laws describing the dielectric response of kidney tissue at high respectively low frequency. The fractional exponents of the power laws describing the dielectric response of irradiated kidney tissue at low frequency.....	153

## LIST OF FIGURES

Figure	Page
1. Mass attenuation coefficients for photons in water (from [8]).....	7
2. Energy transferred to the electron as a fraction of the photon scattering angle.....	9
3. Schematic representation of energy and stopping power dependence on the path in matter, for electrons. (adapted from [12]).....	11
4. Different types of energy localization in water as a function of primary electron energy..	13
5. The two pathways of cell death leading to necrosis. It is important to notice the differences in morphology, <i>e.g.</i> cell swelling with blebbing and increased plasma membrane permeability, in oncosis, vs. cell shrinking with budding in apoptosis (adapted from [14]) .....	20
6. Two frames from the 1955 time-lapse movie by Dr. Marcel Bessis; a) leukocyte (in vitro) at the beginning of apoptosis; b) 33 minute later. after budding, the cell virtually blows-up into a number of apoptotic bodies (from [14]) .....	22
7. Few checkpoints function in order to ensure that complete and correct genome is transmitted. The proliferation of most cells is regulated primarily in $G_1$ but some cell cycles are controlled in $G_2$ . In mammalian cells, arrest in $G_1$ is mediated by p53, which is rapidly induced in response to DNA damage. Mutations in p53 are very frequent in human cancers, thus contributing to genome instability and cancer development. ....	23
8. The frequency dependence of the complex permittivity $\epsilon = \epsilon' - i\epsilon''$ for a pure polar liquid... ..	29
9. Cole-Cole plot ( $\epsilon''$ vs. $\epsilon'$ ) of complex permittivity. ....	31
10. Variation of the dispersion and absorption plots for values of $\alpha \in [0, 1]$ . ....	32
11. The depressed semicircular behavior is characteristic for many biological materials. ....	32
12. Typical dielectric spectrum for tissues (adapted from [30]). ....	36

13.	A leaky condenser - the simplest model for interfacial polarization.....	38
14.	The exact $\epsilon^*$ is physically correct, while the approximation can only be used for $p < 0.2$ . In this example $\epsilon_1 = 78.5$ and $\epsilon_2 = 3.0$ .....	41
15.	Model for the ellipsoidal particles.....	42
16.	Model for the double layered particle .....	45
17.	Double layer structure at the electrode-electrolyte interface. ....	48
18.	Polarization by hopping activated surface conductivity (adapted from [32]). .....	49
19.	Variation of $\epsilon''$ with the frequency $\omega$ . Shown is the $\alpha$ dispersion and at very low frequencies the $\Omega$ dispersions. The effect of the static conductivity is shown in the interval 70-1400S/m .....	50
20.	Graphical representation of $\epsilon'$ and $\epsilon''$ dependence of frequency $\omega$ , in LFD regime .....	52
21.	Ionic conduction effect in blood samples at low frequency. Experimental points were collected only down to $f = 0.05$ Hz and then extended to $10^{-3}$ Hz by fitting with the model.....	53
22.	Lipid bilayer in a plasma membrane.....	55
23.	The membrane model. Proteins are incorporated in a semifluid liquid bilayer. The direction of the ionic pumps ( $\text{Na}^+$ , $\text{K}^+$ , and $\text{Ca}^{2+}$ ) is also shown (adapted from [43]). .....	55
24.	Ions concentration in and outside cell membrane .....	56
25.	Excitation of a linear system with a monochromatic signal $u(t)$ . $G(s)$ is the transfer function characterizing the system, $Y(s)=G(s)U(s)$ , with $s=i\omega$ the Laplace corresponding variable of $t$ . .....	62
26.	The steady-state response $y(t)$ , of a linear system to an input $u(t)$ . ....	62
27.	The response of a real system, either corrupted by noise or with distortions due to non-linearity .....	63
28.	A basic design of a correlation Frequency Response Analyzer (adapted from Solartron ref [44]).....	63

29.	Typical setting for bio-impedance measurements. A Frequency Response Analyzer (FRA) is connected to a Dielectric Interface, which uses a 4-electrode configuration to connect to the sample (adapted from Solartron documentation). .....	68
30.	Special feature of the Dielectric Interface 1294, which makes possible reliable 4-terminal measurements .....	69
31.	Electrolytical cell in the Dewar-like casing. Four of the sample holders (of different diameters) are also shown on top. ....	70
32.	Electrolytic cell for the determination of tissue impedance (adapted from [45]). .....	71
33.	Equivalent circuit for a conductive dielectric sample with electrode polarization.....	75
34.	The treatment head components of a linear accelerator for: A-photon beam and B-electron beam.(adapted from [50]) .....	76
35.	Schematic of major subsystems in Clinac 20 - Varian (from [51]) .....	78
36.	Three dimensional plot of a sample circuit's impedance response (the units for $Z' = \text{Re}(Z)$ and $Z'' = \text{Im}(Z)$ are ohms).....	81
37.	Data gathered from literature on whole human blood [58]. Shown on the vertical logarithmic axis are both $\epsilon_r$ (value) and $\sigma$ (S/m).....	88
38.	Equivalent circuit used in a first approximation. ....	92
39.	Impedance spectra on whole blood, before and during irradiation, in the frequency range (50 mHz-1 MHz). a) ( $Z, \theta$ ) impedance modulus-phase representation; b) ( $Y'', Y'$ ) admittance complex plot .....	93
40.	Simulation of frequency response for the circuit in Figure 38. a) $ Z $ and $\theta$ vs. frequency representation ( $Z =  Z e^{i\theta}$ ) ; b) Complex plane representation.....	94
41.	Improved equivalent circuit for whole blood data .....	94
42.	Impedance modulus and phase vs. frequency representation of the non-irradiated blood. The continuous line represents the fit with the model and the frequency domain was extended to check if the fitted response is physical meaningful (finite response at very high and very low frequencies). .....	95

43.	Comparison between data and fit of the equivalent circuits describing the data shown in FIG. 41.....	97
44.	Imaginary component of impedance, $Z''$ , measured at 1 Hz, as function of time for irradiated and non-irradiated blood. The photon beam is activated after 40 s. No changes occurred in the real component, $Z'$ .....	100
45.	Generic equivalent circuit used to model the dynamic instability .....	101
46.	Kidney data gathered from literature ([71]) .....	104
47.	Real (a) and imaginary (b) part of impedance for a kidney sample at different moments of time after excision. The samples were not irradiated.....	106
48.	Equivalent circuit for kidney samples.....	107
49.	Numerical simulations of the equivalent circuit used to fit the kidney data (extended frequency domain). The experimental data (open circles) are shown only on one fit. ....	108
50.	Impedance spectra of irradiated kidney tissue samples. ....	108
51.	$R_1$ time dependence for non-irradiated and irradiated kidney samples. ....	110
52.	$R_1$ time dependence for non-irradiated and irradiated kidney samples. ....	110
53.	$C_2$ time dependence for non-irradiated samples and irradiated kidney samples. ....	110
54.	$R_2$ time dependence for non-irradiated kidney samples and irradiated samples.....	111
55.	DE-R Time dependence for non-irradiated and irradiated kidney samples. ....	111
56.	DE-T time dependence for non-irradiated and irradiated kidney samples. ....	112
57.	Time dependence of the Phi parameter of the distributed element for non-irradiated kidney samples and irradiated samples.....	112
58.	Sample of liver tissue. Connective tissue and blood vessels are not	

shown. ....	114
59. Dielectric studies on liver tissue and fit [71]. The vertical logarithmic axis is common for $\epsilon_r$ (value) and $\sigma$ (S/m). ....	115
60. Impedance spectra for fresh, non-irradiated liver: a) $Z'(f)$ and $Z''(f)$ ; b) $Z'' = Z''(Z')$ . The time for the 5 measurements shown is: 0, 917, 1826, 12273, 13047 s. ....	116
61. Impedance spectra for irradiated liver samples. The last four are two sets of two measurements taken 18 h and respectively 23 h later. In b) a zoom of $Z' = Z'(f)$ is shown to point out the small immediate radiation induced changes in impedance. The time of the 12 measurements is: 0, 973, 1524, 2137, 3390, 3924, 4420, 5555, 57600, 58320, 82800 and 84180 s. ....	118
62. Magnitude variation of $Z' = \text{Re}(Z)$ during irradiation. The time of irradiation is shown with an arrow. The continuous curve shows the most probable variation of $Z'$ without irradiation. ....	119
63. Equivalent circuit for fitting the liver data. ....	120
64. Representation of the $C_1$ and $W_s\text{-R}$ parameters of the model. The index order is identical with that of the data presented in FIG. 61 and the data recorded immediately after irradiation is marked with an arrow. ....	121
65. Representation of the $W_s\text{-P}$ and $W_s\text{-T}$ parameters of the model. The index order is identical with that of the data presented in FIG. 61. ....	122
66. Representation of the $C_{\text{inf}}$ and $R_{\text{inf}}$ parameters of the model. The index order is identical with that of the data presented in Figure 61. ....	122
67. Dielectric data on lung tissue gathered from literature [71]. ....	126
68. Impedance measurements on lung tissue. All measurement are shown. ....	127
69. Impedance measurements on lung tissue. Data sets taken during the irradiation session are shown for comparison with the three later measurements. ....	128
70. Equivalent circuit used for fitting the lung data. ....	128
71. Data and fitted impedance spectrum for c1 data set. The	

	contribution of the two CPE elements (at low and high frequency) is shown separately.....	130
72.	. The evolution of the two dispersion peaks during the first 4 measurements .....	131
73.	Evolution of the two CPE dispersions after the irradiation. In a) are shown both $Z'$ and $Z''$ frequency dependence of the low frequency dispersion; b) similar plots for the high frequency dispersion .....	132
74.	Comparative evolutions of $R_o$ and $R_l$ of the equivalent circuit modeling the impedance response of lung tissue to radiation injury .....	133
75.	Comparative evolutions of CPE-Phi elements of the equivalent circuit modeling the impedance response of lung tissue to radiation injury .....	134
76.	Comparative evolutions of CPE-T elements of the equivalent circuit modeling the impedance response of lung tissue to radiation injury .....	134
77.	Dielectric data on heart muscle, gathered from literature. On the vertical axis are represented both $\epsilon_r$ (value) and $\sigma$ (S/m).....	137
78.	Impedance, $Z'$ and $Z''$ vs. frequency plots on irradiated heart tissue.....	138
79.	Elementary analysis of the non-irradiated heart tissue impedance response. The semicircle represents the response of a simple Cole element and the deviation at high frequencies is evident.....	140
80.	Equivalent circuit for heart tissue.....	140
81.	a) Separate response of the two Warburg circuits. b) Data and extended fit with the equivalent circuit.....	141
82.	Evolution of the $W_{s1-R}$ and $W_{s2-R}$ parameters for irradiated and non-irradiated samples .....	142
83.	Evolution of the $W_{s1-T}$ and $W_{s2-T}$ parameters for irradiated and non-irradiated samples .....	142
84.	Evolution of the $W_{s1-Phi}$ and $W_{s2-Phi}$ parameters for irradiated and non-irradiated samples.....	143
85.	A representation of different types of dielectric responses. The two	



- upper curves of each representation are the plots of the real and imaginary components of the susceptibility (in logarithmic scale). The lower curve is the complex plot of the same two quantities. In A is represented the Debye mechanism, the response (almost inexistent) of a collection of non-interacting dipoles. B, usually occurring in liquids, implies short, nearest-neighbor interactions, such the both  $\epsilon'$  and  $\epsilon''$  are proportional with  $\omega^{-n}$  ( $n < 0.3$ ); C represents also a response in a system with the same type of interactions as B, but characterizing the low frequency dispersion with  $n \sim 0.5$ ; in D a higher frequency response is shown, typically observed in polymers,  $n > 0.6$ ; in E, the mechanism of relaxation is due to hopping charges and the interactions are of the 'many-body' type. Characteristic to ionic conductors or high-density carrier systems,  $n < 0.3$  (adapted from [91]) ..... 147
86. Dielectric response of freshly excised kidney tissue. The power law frequency dependence of  $\epsilon'(\omega)$  and  $\epsilon''(\omega)$  (straight lines in log-log representation) are shown. The tissue was not irradiated. .... 152
87. Permittivity,  $\text{Re}(\epsilon)$  vs. frequency for liver and kidney tissue..... 154
88. Representation of  $\epsilon'=\text{Re}(\epsilon)$  and  $\epsilon''=\text{Im}(\epsilon)$  versus frequency, a 'universal' response of tissues..... 155

## CHAPTER I

### INTRODUCTION

Every year, about 1.25 million people in the United States are diagnosed with life-threatening forms of cancer<sup>§</sup>. About 60% of these patients are treated with radiation and half of them are considered curable because their tumors are localized and susceptible to radiation. Radiation therapy has been used to treat cancer for over 100 years. The most common type of radiation therapy uses photon beams with energy of 6-20 MeV. Electrons of similar energies are used for treating superficial tumors. While the photons and electrons are the mainstream particles used in radiation therapy, a number of other particles are used: protons, pions, neutrons, heavy ions, but their use is severely limited by both equipment availability and cost. The goal of radiation therapy is the killing (or inactivation) of cancer cells in tumors, while minimizing the effects on the normal tissue. In the last two decades, the development of the three-dimensional conformal radiotherapy, allowed precise delimitation of the targets (presumably the tumor) and the delivery of high radiation doses while sparing as much as possible the healthy tissue and avoiding normal tissue complications. More recently, the Intensity Modulated Radiation Therapy (IMRT) allowed the escalation of the prescribed doses close to 90 Gy with a 1% precision in the dose distribution.

However, despite the accuracy with which a radiation dose can be delimited to a given 'target' volume, there is a great uncertainty about the effectiveness of that dose. John Cameron, a well-known medical physicist, Emeritus Professor University of Wisconsin-Madison, states very clearly the current situation in radiation dosimetry: "*..it is likely that the present physical dosimetry (J/kg) is much more accurate than we need. The physics of dosimetry is in much better shape than (our knowledge of) the biological response of the cancer and of the normal tissues to the dose. That is the hard part and it is often ignored. Even a given type of cancer can vary greatly in its response and so can the response of the normal tissues of the patient.*" A very recent article [1] coming from one of the leaders in the field of radiotherapy research, stresses that "*The ability of IMRT*

---

<sup>§</sup> The journal model for this thesis is Physical Review E

*to paint (in 2D) or "sculpt" (in 3D) the dose, and produce exquisitely conformal dose distributions ..., begs the "64 million dollar question" as to HOW to paint or sculpt".*

The answer, or at least a good part of it, seems to be the newly proposed concept of "biological target volume". This would imply the use of biological images, which in contrast with the conventional radiological images will carry physiological and functional information about the tumors and surrounding normal tissue. There is now, the authors conclude, a tremendous need for new and if possible, non-invasive methods, yielding radiobiological information. NMR spectroscopy, using as imaging parameters the proton (or other nuclei) density and relaxation times and PET (positron emitted tomography) using FDG (fluorodeoxyglucose radiolabeled with  $^{18}\text{F}$ ) as tracer can provide metabolic and functional information. The vital processes at the cell level, as well as cooperative processes at the tissue level are, in their essence, electrochemical processes. The transport of electrons, protons and ions is of paramount importance for living matter. It is almost natural to think of the dielectric properties - conductivity and permittivity - as parameters that can be imaged with the hope of obtaining subtle, structural and functional information at cell and tissue level.

The measurements of electrical properties of biological materials held, historically, a pre-eminent position in biophysics and physiology. The study of dielectric properties of matter was pioneered by Debye [2], Van Vleck [3], Frohlich [4] et al. but soon turned out to be an important tool in the study of living matter, too. Initially, the physicist's territory, dielectric and electronic properties of biomolecules, cells and tissues is now used widely by biochemists, biologists, medical doctors, electrical engineers, etc. When dielectric properties are investigated, one can model the system in a multitude of ways: from a mixture of spheres in a conducting fluid, to a heterogeneous disordered media, or a fractal, a percolation system, or a colloidal suspension. Such a system can be described, under the right assumptions, as open or closed, linear or nonlinear, deterministic or chaotic, classic or quantum, etc.

Understanding radiation interaction with living matter and finding suitable models for radiation induced effects, implies not only the physics of the elementary energy deposition processes, but statistical and condensed matter, colloid physics, radiation chemistry and radiation biology as well. One of the difficulties of studying a biological

tissue is that the model has to be as simple as possible but at the same time still relevant for its microstructure and functionality. The radiation effects are relatively well described in simple systems, like semiconductors - mainly because of the needs of the space research - or in insulating, non-polar liquids. But where is the complexity threshold for modeling biological systems under the effect of ionizing radiation? Of course, from the biology standpoint, all the important phenomena are related to the cell - as fundamental organizational element - and its structure and dynamical behavior. A suitable mathematical model would be a system composed of many interacting cells, the interaction being mediated by contact (gap junctions) or diffusion or indirectly through the extracellular matrix. Organization of cells distributions and aggregation is known to strongly depend on the interaction parameters (with evidence that the cancer cells are less "gregarious" than the healthy ones). When considering dielectric properties as markers of the radiation induced effects, we have to take into account not only the structure of the tissue and cells but also their change in functionality and dynamics after the injury, along with known biochemical effects. These are, in broad terms the coordinates on which this work is placed.

We have investigated the dielectric properties of tissues (blood, lung, kidney, liver, heart) as a function of time, in response to irradiation, during the treatment and at early times after. Experiments were performed at Virginia Beach General Hospital (VBGH) on rat tissue samples freshly excised. The hope is that the dynamics of dielectric parameters can be used to assess the cell death progression and thus to provide feedback guiding the delivery (dose and timing) of the radiation treatment. The challenge is twofold: the experiments at these frequencies have to be carried out with numerous precautions; the second is the scarcity of models for low frequency dispersion in complex systems like tissues, as well as the lack of precedent as to how to relate radiation-induced effects to parameters accessible to dielectric measurements.

The technique can be developed as a non-invasive one because electrodes are applied on the skin, but other non-contact approaches are also at the horizon. In recent years, NMR was combined with current injection [5,6] and specific ways of processing the signal, to yield, with the high resolution characterizing NMR, dielectric parameters as new imaging parameters. Neoplastic (cancerous) tissue causes alterations in intracellular

and extracellular fluid compartments, cell membrane surface area, ionic permeability, and membrane associated water layers. Impedance tomography, the spatial resolved version of electrical impedance spectroscopy has already gained acceptance in the medical world by the recent authorization by FDA of an impedance-based device, T-Scan2000, for the detection of breast cancer tumors [7].

In Chapter II we review the main mechanisms of interaction of radiation with matter. The first part is devoted to brief descriptions of the photon interaction: the photoelectric effect, Compton scattering, pair production. We then continue with fundamentals of electron interaction processes. Given that the processes categorized as physical only account for the very early ( $10^{-18}$  to  $10^{-9}$  s) energy deposition events, we describe the timing and spatial extent of the whole process, continuing with elements of aqueous radiation chemistry and the specifics of radiation effects on cells. The last part of this chapter is an overview of the mechanisms of cell death and their relevance in the context of both radiation therapy and dielectric studies. The understanding of apoptosis, oncosis and necrosis is central to the rationale of using the dielectric properties of tissues as markers of the radiation induced injury and its progress.

A self-consistent description of dielectric properties of matter, with emphasis of cells and tissues, is the subject of Chapter III. After a practical definition of permittivity and conductivity, the Debye relaxation mechanism is introduced, together with several representations (*e.g.* Cole-Cole) plot. Under the general heading "non-Debye mechanisms" a number of dielectric relaxation features, especially important in heterogeneous and disordered systems, is discussed next. The classification of  $\alpha$ ,  $\beta$ ,  $\Omega$ ,  $\gamma$ , dispersions in tissues is explained with emphasis to the relaxation mechanisms contributing. Extremely important in inhomogeneous materials, the Maxwell-Wagner interfacial polarization, for spherical and ellipsoidal particles, as well as special cases of high concentration mixtures are presented in detail. For cellular systems, a correct understanding of their components, structure and function, is important for an efficient modeling as electrochemical systems. These, as well as other important issues, like surface conductivity, counterion polarization and low frequency dispersions (LFD) phenomena are the subject of the last part of this chapter.

Chapter IV is dedicated to the presentation of electrical impedance spectroscopy. The method, the experimentally accessible parameters and the technique used in our experiments - the frequency response analysis - are explained.

In Chapter V we describe the experimental method. The main issues are: the apparatus for impedance measurement, the cell measurement design and the irradiation environment. Also, important contributors to the success of the experimental measurement of impedance, like temperature control and electrode polarization, are discussed, and specific methods we choose to solve them, are given.

By far the largest, Chapter VI is devoted to the presentation and analysis of the experimental data. As a preamble to data analysis, we started by discussing methods used for validating the data. A critical view towards data modeling is also given at the beginning of the chapter. Each of the five tissue types (blood, kidney, liver, lung and heart) we studied is described in the following succession: we started with an overview of the tissue specific structure, function and dielectric properties. Whenever known, radiation effects and their possible relation to changes of dielectric properties, are discussed. After the presentation of the experimental results, we assemble the model used to interpret the data; when more than one model is discussed, we give the rationale for that and a comparison is being made. At the end, conclusions are drawn on whether the dielectric changes are consistent with the radiation-induced changes in the morphology and microstructure of the tissue.

Conclusions are the subject of Chapter VII. In spite of the differences between the tissues analyzed, a unitary explanation based on Jonscher's "universal dielectric relaxation" is attempted. General conclusions on the method's efficiency and possible future developments wrap up the presentation of the thesis.

## CHAPTER II

### IONIZING RADIATION

#### The interaction of radiation with matter

When radiation is delivered to an organism with the intent of inactivating (or killing) its cells, the physics of energy deposition is only the first stage. It has to be followed by the radiation chemistry and radiation biology. In this chapter, I will try to present the relevant processes, their description, magnitude and importance, with emphasis on charge carriers and radiation induced conductivity changes. We will first review the interaction of ionizing radiation with matter. Since water is the essential 'ingredient' in the life forms that are of interest for us (mammalian cells) the radiochemistry of water will be briefly described next.

At the very elementary level, we know what these mechanisms are and we can describe them fairly accurately. We will limit our discussion to photons, since it represents about 90% of the radiation therapy modality and it was the only type of radiation used in our experiment. For photons, the photoelectric effect, Compton scattering and pair production are the primary channels through which a beam of intensity  $I_0$  is attenuated after passing a slab of material of thickness  $x$ . The dependence of intensity  $I$  of  $x$  is known as the Lambert law:

$$I(x) = I_0 e^{-\mu x} \quad (1)$$

where  $\mu$  is the total linear absorption coefficient (expressed in  $\text{cm}^{-1}$ ). The law holds only for a monochromatic beam and as consequence the energy transferred to a medium has a much more complex form. The total absorption coefficient  $\mu$  is the sum of the 'partial' absorption coefficients, governing the three processes described. With the notation  $\sigma_c$  for Compton absorption,  $\tau$  for photoelectric absorption and  $\kappa$  for pair production, the linear coefficient of attenuation for photons in water (represented in Figure 1) will be:

$$\mu_a = \sigma_a + \tau + \kappa, \quad (2)$$

The attenuation produced by a certain thickness  $x$  of material depends either on the density of electrons with which the photons interact or the density of the atoms. The former is most important for biological tissue systems. A more fundamental quantity, the mass attenuation coefficient (units of  $\text{cm}^2/\text{g}$ ), can be obtained by dividing the above quantities by the density  $\rho$ . The dependence of the mass attenuation coefficient on energy is shown in Figure 1, below:

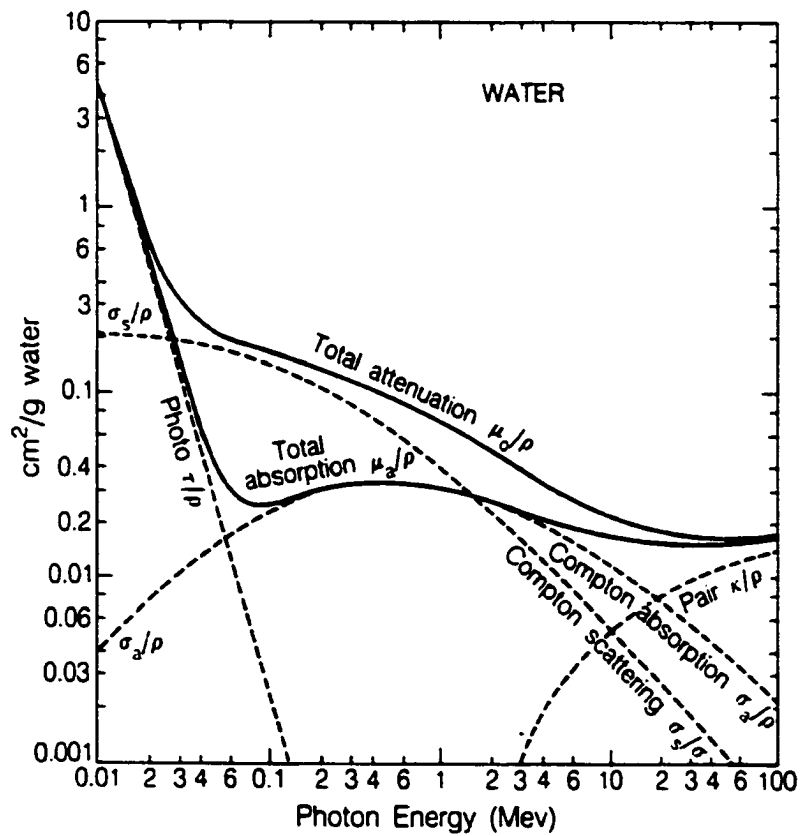


FIG. 1. Mass attenuation coefficients for photons in water (from [8])



### *Photoelectric effect*

In the photoelectric process, a photon is completely absorbed with the ejection of one electron, the kinetic energy of which is equal to the difference  $h\nu - I_B$  ( $\nu$  is the frequency of the incident photon and  $I_B$  is the binding energy of the electron in the atom) except for a negligible quantity which is the energy imparted to the remaining atom. The probability of interaction is maximum when the energy of the photon just exceeds  $I_B$ , the cross section exhibits sharp changes for the so-called orbital edges, K, L, etc. In tissues, the energy transferred to the atom by the photon is equal to the energy absorbed and both are nearly equal to  $h\nu$ .

Given that the tissue elements are low  $Z$  elements with very small binding energies (smaller than 500 eV), essentially all the photon incident energy is absorbed. The distribution of the photoelectron is forward for high photon energy and almost perpendicular with respect to the incident photon for low energies, a dipole pattern.

### *Compton Scattering*

The Compton interaction is an elastic collision between a photon and a loosely bound electron. We can actually distinguish a coherent scattering process (Rayleigh scattering) and an incoherent one. In the first kind there is in fact no transfer of energy from the incident photon to the medium; the only result is an increase in the angular dispersion of the photon beam. Given also the small cross section of the process for small  $Z$  materials, at energies greater than 100 keV, there is no interest with respect to chemical or biological events. The incoherent Compton scattering is one of the most important mechanisms of interaction of photon beams with tissue like materials.

After a simple derivation using classical mechanical arguments, one can write simple expressions for the scattered photon and (an unbound) electron:

$$E_e = h\nu \frac{\alpha(1 - \cos\theta)}{1 + \alpha(1 - \cos\theta)} \quad \text{and}$$

$$h\nu' = h\nu \frac{1}{1 + \alpha(1 - \cos\theta)}, \quad (3)$$

where  $\alpha = hv/m_0c^2$  and  $\theta$  is the photon scattering angle.

One can see (Figure 2), that the transfer of energy to the tissue becomes important only for  $\alpha = hv/m_0c^2 > 0.1$ , which translates into photon energies greater than 50 keV. To estimate the total energy transferred by Compton scattering, we have to take into account the differential cross section for the process, the well know Klein-Nishina formula:

$$\frac{d\sigma_t}{d\Omega} = \frac{e^4}{2m_0^2c^4} \left( \frac{1}{1+\alpha(1-\cos\theta)} \right)^2 \left( 1 + \cos^2\theta + \frac{\alpha^2(1-\cos\theta)^2}{1+\alpha(1-\cos\theta)} \right), \quad (4)$$

where  $e$  and  $m$  are the charge and mass of the electron,  $\theta$  is the photon scattering angle and  $\alpha$  was previously defined.

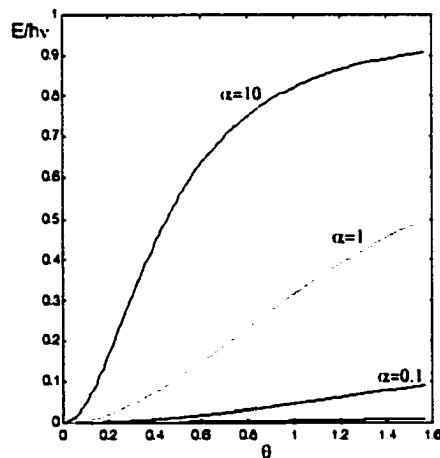


FIG. 2. Energy transferred to the electron as a fraction of the photon scattering angle.

From this, one can obtain the spectrum of Compton electrons. Qualitatively, the electron will have a maximum energy less than the energy of the incident photon, and the distribution goes through a minimum, so the probability is larger for small and high energy, rather than intermediate ones.

Adjustments can be made to consider the binding energy of the electrons, but since the only part in which there are significant differences in the KN coefficients is at low energies, it is insignificant at photon energies of interest for biological processes.

### *Pair Production*

While Compton scattering and the photoelectric effect involved photon interactions with an electron, the next significant channel for energy absorption - pair production - deals with photon interactions with nuclei. An energetic photon ( $E > 2 \cdot 0.511 \text{ MeV}$ ), interacting with a nucleus can decay into a positron-electron pair. The cross section for the process is proportional to  $Z^2$ , but a correction needs to be applied for large energies, due to the screening of the nuclear charge by the electrons. The atomic cross section for pair production is, in a first approximation,  $\kappa_a = \ln(h\nu)$  [9]. In water, pair production becomes significant for photon energies greater than 3 MeV. The kinetic energy of the produced pair is simply the energy balance between the energy of the incoming photon and the necessary energy to produce a pair of electrons:

$$E_{tr} = h\nu - 1.022 \text{ (MeV)}. \quad (5)$$

The real energy absorbed by the tissue is more difficult to find since the two electrons may lose energy by bremsstrahlung. When the positron loses energy, it might interact with a free electron to produce two annihilation photons. These will be further treated as scattered photons from Compton process.

After this brief review of the main mechanisms by which photons interact with matter, we can conclude that, regardless of the mechanism, the important phenomenon, leading to chemical changes, is the generation of secondary electrons. We will now discuss the interaction of charged particles - electrons - with matter. The best known macroscopically quantity related to the slowing down process is the stopping power<sup>1</sup> of the medium. The two important types of interaction between electrons and matter is bremsstrahlung, at high energies and Rutherford collisions at low energies. The stopping

power for electrons (in the range  $E < 100$  MeV), incident upon a material with atomic number  $Z$ , can be calculated using the expression given by Bethe and Ashkin [10]:

$$-\frac{dE}{dx} = \frac{2\pi N e^4 Z}{m_e v^2} \left[ \log \frac{m_e e^2 E}{2I^2(1-\beta^2)} - (2\sqrt{1-\beta^2} - 1 + \beta^2) \log 2 + 1 - \beta^2 + \frac{1}{8}(1 - \sqrt{1-\beta^2}) \right], \quad (6)$$

where:  $-dE/dx$  is the stopping power or the energy loss per unit path,  $N$  is the number of atoms per  $\text{cm}^3$ ,  $Z$  is the atomic number of the stopping material and  $I$  is the average excitation potential of the atom for the stopping material (66 eV for water),  $E$  the kinetic energy of the electron,  $v$  its velocity (in cm/s),  $\beta = v/c$ , and  $c$  is the speed of light. The energy loss for electrons with an initial energy of 10keV in water is 0.22 eV/Å but falls to 0.02eV/Å for  $E=400$ keV and remains practically constant as  $E$  continues to rise.

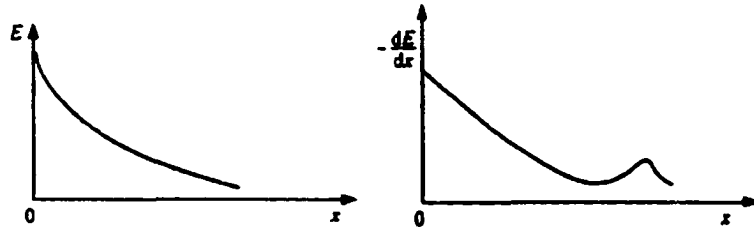


FIG. 3. Schematic representation of energy and stopping power dependence on the path in matter, for electrons. (adapted from [12])

An important correction has to be made for the passage of a charge particle through a dense medium. The polarization of the medium under the influence of the electric field of the passing particle will in fact weaken the influence of the atomic electrons and as a result the stopping power of the medium will be reduced. Formula (6) contains corrections due to relativistic, shell and the density effects discussed.

---

<sup>1</sup> Defined as the rate of energy loss per unit of path length.

For molecular media, Bragg put forward a simple rule: if a substance is represented by a chemical compound  $A_mB_n$ , composed of  $m$  atoms  $A$  and  $n$  atoms  $B$ , then the relation between its stopping power and that of its constituents is:

$$\left( -\frac{dE}{dx} \right)_{A_mB_n} = m \left( -\frac{dE}{dx} \right)_A + n \left( -\frac{dE}{dx} \right)_B. \quad (7)$$

The implicit assumption here is that the chemical bonds between atoms do not affect the interaction of the particle with the atomic electrons. Experiments have shown that, in general, the stopping power is slightly over-evaluated by the Bragg's composite law.

For electrons penetrating a medium, there are two mechanisms of stopping: ionization and radiative. The energy transferred by all processes and absorbed in the medium defines the dose  $D$ , formally, energy deposited per unit mass:

$$D = \frac{dE_{abs}}{dm}. \quad (8)$$

The unit for dose is Gray (1 Gray=1 Joule/1 kg) but older units (e.g. 1 rad =  $10^{-2}$  Gy) are still tolerated.

### *Spatial and time Dependence of Energy Deposition*

So far, we have discussed fundamental processes which have little do to with the effects at the cellular level. Remembering that the goal of the irradiation process is to create damage, let's turn to the typical track structures created by energy deposition and what is the timing of the processes initiated by the energy deposition.

Ionizing radiation imparts primary energy to matter in discrete packets ("energy deposits") conveniently categorized [11] according to the energy deposited, as spurs (~ 6 to 100 eV), blobs (~ 100 to 500 eV), and track segments (~ 500 to 5000 eV). As an example, a 1 MeV electron spends 65% of its energy to produce isolated spurs, 15% in blobs and 20% in short tracks, while a 10 MeV electron creates isolated spurs to the extent of 76% of its energy, 8% for blobs and 16% for short tracks. In aqueous media, the spurs and blobs created are associated with roughly spherical regions about 4 and 7 nm in

diameter, respectively. Short track segments in aqueous media impart their energy to spheroid shaped regions of matter with dimensions on the order of 25 to 75 nm. Right after the energy absorption, a number of "primary products" are created: electrons, ions, free radicals, excited states, etc.

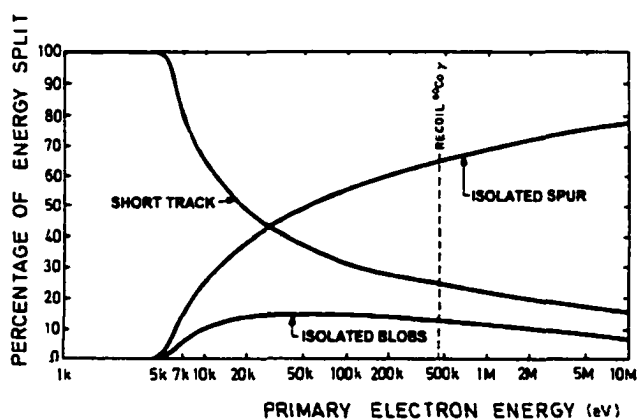


FIG. 4. Different types of energy localization in water as a function of primary electron energy [11].

The term primary can be better understood if we relate it to the time needed for radiation (electromagnetic or charged particle) to traverse a typical molecular distance of the order of few Å:  $10^{-18}$  -  $10^{-17}$  s. Following energy deposition the excited and charge species formed will undergo a series of deexcitation, thermalization, neutralization processes to form more stable radiolytical species. A sampling of the chronology of events, from the energy deposition, to the appearance of primary species and their diffusion, to the damage of the biological molecules and its repair, is presented in Table I.

At the beginning, the important processes leading to the formation of free-radical products are the following. First there is the ionization and excitation of water molecules:

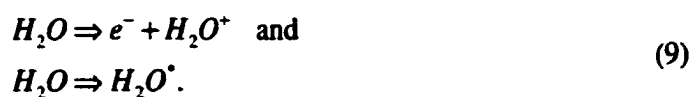


TABLE I. Timing of processes from energy deposition to biological effect

Event	Time (s)
Traversal of a molecular diameter by a high-energy electron	$10^{-18}$
Ionization and excitation	$10^{-17} - 10^{-16}$
Relaxation of excited states	$10^{-15} - 10^{-13}$
Dissociation of excited molecules	$10^{-14}$
Thermalization of secondary electrons in water	$10^{-13}$
Fluorescence	$10^{-9}$
Lifetime of the spur in liquid water	$10^{-7}$
Phosphorescence	$10^{-3}$
Damage to important biological molecules	$10^{-3}$
Enzymatic repair of molecular damage	minutes
Biological repopulation from survival cells	hours

The electrons ejected in the ionization process become thermalized and hydrated



An electron slowed down in a liquid of high  $\epsilon$  ( $\sim 80$  for water), will give rise to an orientation of the dipoles (water molecules) in its radial electric field. The electron is trapped almost as effective as if it were bound to a nucleus. A new entity is formed, the solvated electron ("hydrated" in the case of water). It is thought that the electron interacts strongly with a "solvation shell", the closest four to six water molecules, by short-range charge-dipole (permanent and induced) attraction. The  $H_2O^+$  ions then undergo a proton transfer reaction with neighboring water molecules:

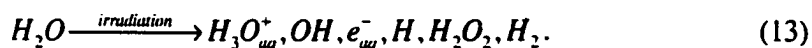


An excited water molecule dissociates into a hydrogen atom and a hydroxyl radical



In water, however, the contribution of excited molecules to the formation of free radicals is minor compared to that of ionization processes.

The state of the irradiated water after about  $10^{-9}$ s, when the reactions in the deposition structures are terminated can be described as:



An important quantity related to these primary species is the *yield*  $G$ , the number of free radicals (H, OH or e-) or molecules ( $H_2$  or  $H_2O_2$ ) created per absorbed 100 eV. Knowing  $G$ , one can find the rate of radical production which is the product of *dose rate* and  $G$ . Average values of yields for the free radicals or molecules mentioned are:

$$G_H + G_{e_{aq}^-} = 3.18 \quad G_{OH} = 2.72 \quad G_{H_3O^+} = 2.65 \quad G_{H_2} = 0.45 \quad G_{H_2O_2} = 0.68 \quad G_{-H_2O} = 4.09$$

The fate of the free radicals created in aqueous solutions depends on very many factors, among them being: pH, temperature, scavengers concentration, dose rate, etc. The radiochemistry of water and organic liquids are sub-fields of study by themselves. We will address the known reactions of free radicals with biopolymers, the most notable being DNA. About 20% of the OH radicals will react with the sugar links (deoxyribose) in the DNA chains, leading to strand breaks (breaks of the sugar-phosphate bonds). The yield of strand breaks in DNA is  $G = 0.2-0.8$  for ssb (single strand breaks) and  $G = 3-9 \cdot 10^{-2}$  for dbs (double strand breaks). For chromatin DNA the values are about 100 times smaller. The subject of DNA damage and its importance in the radiobiological process will be discussed in more detail in the next section.



## Biological effects of ionizing radiation

Radiation effects on individuals are a function of the radiation effects on the cells which make up various organs and systems of the body. All biological effects can be traced to damage on the level of individual cells, the specific effect being dependent on the type and extent of damage. The class of lesions that most closely correlates with cell death is the DNA double strand break but in recent years other targets have been recognized, including the cell membrane. Enzymatic pathways can quickly and effectively repair the majority of lesions. Misrepaired lesions, lead to mutations and clonogenic<sup>2</sup> cell death. Details about radiation induced cell death, central to our study, will be given in the following section on cell death.

There are two basic ways to characterize the influence of radiation on cells, direct effects and indirect effects. The *direct effect* can be defined as direct ionization of DNA or other structure by radiation. When passing particles, either primary radiation particles or secondary ones (i.e., the  $\delta$ -rays created by the passage of a single primary radiation particle) deposit energy to matter in a volume of interest (e.g., the cell nucleus), a radiation event occurs. These events, considering DNA as a primary target, are the single break strands (sbs) and double break strands (dbs).

*The indirect effect* consists of ionization of water molecules within the cell with the creation of very chemically active agents (free radicals) which in turn, can chemically attack other molecules in their immediate vicinity. If a DNA molecule is located in this area, alteration to the DNA molecule can occur. Since studies have shown that very few critical sites exist in the cell, indirect effects actually cause most of the damage. Free radicals are able to disperse throughout the cell and can react with materials of the cell over greater area than the original beam of radiation.

---

<sup>2</sup> Sometimes called *reproductive death*, refers to the failing ability of cell to reproduce, to act as a clone for a significant (more than 2, 3) line of offspring.

### *Production of free radicals from water*

The mechanism of indirect effects relies on the formation from water of highly energized molecules or atoms called free radicals. The most important free radicals<sup>3</sup> produced by water radiolysis are the OH<sup>·</sup>, or hydroxyl radical and the H<sup>·</sup> or atomic hydrogen radical. Free radicals are usually chemically highly reactive and thus seek to combine either with another free radical to form a stable molecule or with an ordinary molecule to form both a stable molecule and a less reactive free radical. Some free radicals will combine and form H<sub>2</sub>O<sub>2</sub> and HO<sub>2</sub>. These compounds, while not as reactive as the original free radicals, are thought to be primary agents of cellular damage, since they are able to disperse throughout the cell and are thus more likely to react with important biological molecules. Damage to cells can take on various forms. If the DNA is damaged, a loss of control in daughter cells may result, or the ability to duplicate may be lost. Non-specific cell damage can result in loss of important cellular functions, production of toxic waste products or cell death without further reproduction.

### *Cell Death*

We will now give an overview of the mechanisms of cell death and will discuss why and how these are important for radiotherapy. An understanding of the mechanism of cell death is central to identify how measuring macroscopic parameters like electric permittivity and conductivity can be related to changes<sup>4</sup> occurring in cells and tissue. Also, distinguishing between different death mechanisms triggered by radiation is vital for both the treatment itself and for its final outcome. A crucial question coming into play, on a quite controversial subject, will be: is it the DNA damage that is mainly responsible for cell death (or inactivation), or are there other mechanisms at the level of cell organelles or molecular complexes (cytoskeleton, mitochondria, ionic pumps, etc.) that also contribute?

Most of medicine is involved with cell death, either in preventing cell death and necrosis (*e.g.* transplants, stroke, trauma) or in causing or promoting cell death (*e.g.*

---

<sup>3</sup> A free radical is defined as *any* chemical structure that contains an unpaired electron.

cancer treatment). It is important to emphasize the otherwise implicit idea, that even though we will continuously refer to *cell* we expect that organized tissue systems respond as predicted by cellular studies. This is, in principle, true, but there are a number of local conditions able to modulate the response, some of which are not completely understood, including the supply of metabolic substrates (or removal of metabolic products), the effect of hormonal substances responsible for regulatory performance, and tissue physiological environment (*e.g.* state of oxygenation, free radical scavenger capacity), etc.

The concept of death evolved slowly to our current understanding, namely that programmed death (and we will define the term later) is an intrinsic part of the development of all invertebrate and vertebrate multicellular animals. It starts with the morphogenesis, the self organization processes that leads to formation and differentiation of tissues and organs- and continues with tissue homeostasis, regulation of cell numbers, elimination of damaged cells and defense against infections. Malfunction of this mechanism is an important component in the pathogenesis of several human diseases, including AIDS and cancer. The death mechanism is regulated by signals provided by other cells, either directly, cell-to-cell contacts, or indirectly, by soluble mediators or cell lineage information. It should be vigorously emphasized that multicellularity seems to be intimately linked to the evolution of the mechanism of programmed death. With the exception of germs, all other cells, in a multicellular organism, are 'condemned' to live together and to cooperate such that the whole system remains adapted to its environment. The mechanism of death can be seen, in this light, as a social form of regulation of cell survival, through a process of 'altruistic' suicide for the benefit of the organism as a whole. It is also worth mentioning that all cells from multicellular organisms or structures (*e.g.* tissue, organ) undergo programmed death<sup>5</sup>, *in vivo* and *in vitro*, despite the existence of adequate nutrients *if they are deprived of contact*. At the same time we have to remember that there are a number of quite different cell population kinetics, ranging from close, almost static populations (*e.g.* neurons in the central nervous system), to dividing,

---

<sup>4</sup> The generic term *changes* should in fact be read *radiation-induced changes*. It basically refers to changes in the cell population as well as changes in the tissue morphology.

<sup>5</sup> In a healthy human body, there are about 70 billion cells dying every day (from apoptosis), so the death of a cell is not something unusual [13].

transit populations (*e.g.* blood cell types) In culture, a cell population under a minimal density threshold (and in the absence of externally added survival factors) will undergo a rapid induction of programmed death. An interesting connection with the conduction in fractal systems and the percolation limit will be made in Chapter III. Also, the adhesion dependent cell-regulation through the interaction with the extracellular matrix (EM) will be discussed in the context of the radiation-induced denaturation of the EM.

The term *programmed death* is usually synonymous with apoptosis (for invertebrates, the term is cell deletion), and refers to the natural death associated with healthy tissues or organs. The other type, *the accidental death*, occurs as a result of a cell injury. In both cases, one can distinguish three phases of the cellular reaction: a prelethal phase (potentially reversible), the cell death and necrosis phase [13]. The term necrosis is sometimes used as cell death due to accident, injury or disease. We will differentiate here the prelethal phase from the death phase, thus using necrosis to name the changes in cells *after* death.

The two pathways to death and necrosis, oncosis and apoptosis (in more vivid terms these two can be called respectively cell death by murder and cell death by suicide) are very different in their structure, function and occurrence.. Even though fundamentally different, in real systems it is difficult to separate them. Often the two pathways occur in combination, oncosis at the center of a lesion, apoptosis at the periphery. There is no universal response even for a given type of injury or trigger. Instead, there are a large number of factors which play roles into the dominance or one or another of the cell responses (*e.g.* hypoxia<sup>6</sup> have been shown to increase apoptosis). After an injury like ionizing radiation, the cell type is, for example, a factor in the type of response (note that there are approximately 200 types of cells in an adult human being). A graphical description of the differences between oncosis<sup>7</sup> and apoptosis<sup>8</sup> is shown in Figure 5. .

---

<sup>6</sup> Defined as lack of oxygen in the tissue

<sup>7</sup> From the Greek *oncos* - swelling

<sup>8</sup> The Greek name comes from *apo*-meaning from, and *ptosis*-meaning a fall, and suggests leaves falling here and there under a tree

*Apoptosis vs. necrosis*

We will examine further the specifics of the two pathways to necrosis. The suicide mechanism for apoptosis is under genetic control.

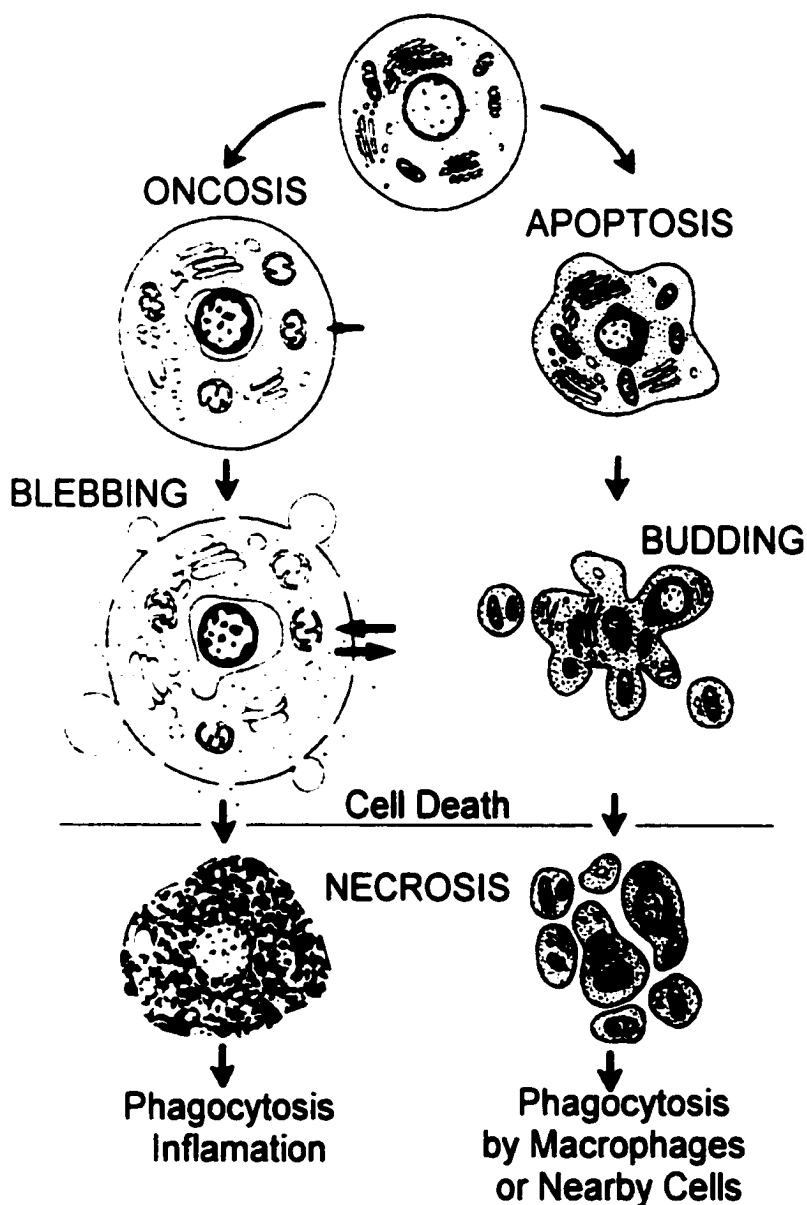


FIG. 5. The two pathways of cell death leading to necrosis. It is important to notice the differences in morphology, e.g. cell swelling with blebbing and increased plasma membrane permeability, in oncosis, vs. cell shrinking with budding in apoptosis (adapted from [14])

The trigger, though, can have an amazing variety: an internal clock, extracellular agents (hormones, cytokines, etc.) or a variety of physical (ionizing radiation, hyperthermia), chemical or viral agents. A central component of the death-signaling pathway in many cells, particularly in tumor cells exposed to chemo- or radiation therapy, is the anti-oncogenic gene p53. This transcription factor is an interesting example of bifunctional protein involved in both cell proliferation and cell death. In many cell systems a primary trigger for P53 synthesis is DNA damage such as that caused by accumulation of reactive oxygen species (free radicals) or by the direct action of radiation. The generation of P53<sup>9</sup> can be considered a necessary but not a sufficient condition for apoptosis. Many proteins are involved in apoptosis, the most significant one being Bcl-2. It has an antagonistic role to p53, blocking the physiological cell death in many mammalian cells, sometimes even after the action of toxic agents.

An important limitation to assess the apoptosis *in vivo* is the fact that it is a rapid mechanism that leaves only subtle traces. The timing of the apoptosis can be a fast one, (see Figure 6) running its course in minutes or tens of minutes after the onset, which is one of the reasons that it escaped undetected and unnoticed by pathologists for a long time<sup>10</sup>. Besides, it is not always synchronized in a cell population.

Morphologically, during apoptosis, the cell shrinks and loses normal contacts, and this constitutes one very important feature in the rationale for using Electrical Impedance Spectroscopy as a tool for assessing cells death in tissue. In fixed sequence, chromatin condensation, cellular budding and fragmentation and rapid phagocytosis by either neighboring cells or specialized phagocytes, are typical events that describe apoptosis. If as a results of a trigger (*e.g.* radiation) a significant number of cells undergo apoptosis in the same time frame, it is expected that that loss of contacts and the shrinking and fragmentation, will be translated into an decrease of conductivity at low frequency and a shift in the characteristic dispersion peak at intermediate frequencies.

---

<sup>9</sup> The gene is written in lower case (p53) and the corresponding protein in upper case (P53)

<sup>10</sup> Dr. Marcel Bessis did the first known cinematographic recording of apoptosis in 1955.

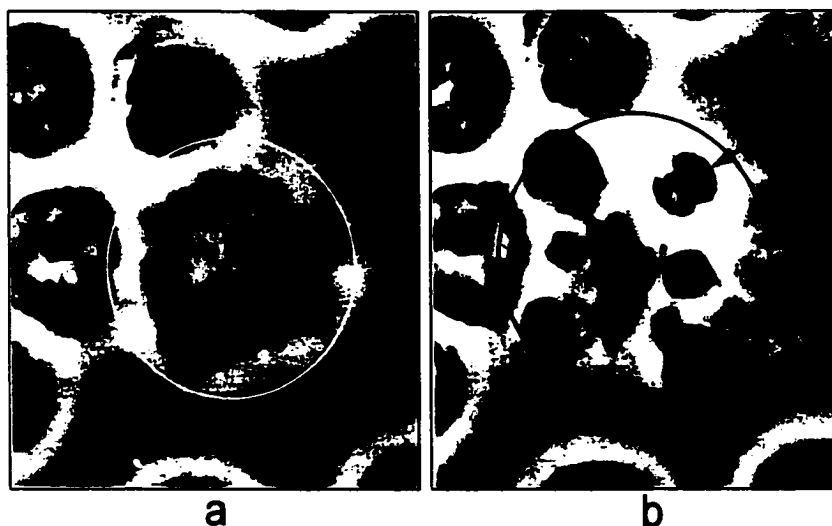


FIG. 6. Two frames from the 1955 time-lapse movie by Dr. Marcel Bessis; a) leukocyte (in vitro) at the beginning of apoptosis; b) 33 minute later, after budding, the cell virtually blows-up into a number of apoptotic bodies (from [14])

Changes in the parameters modeling the membrane response as well as variation of the extracellular space volume (an increase for apoptosis, decrease due to swelling, for oncosis) will also play a role into the dynamic of dielectric parameters.

The shrinking and condensation mechanism are largely unknown. A possible explanation for the increased density could be the accumulation of denaturated proteins, which in turn have been linked to the increase in the intracellular calcium. Recent research elucidated part of the mechanism by which cells activate enzymes called caspases carry out the 'dirty work' of cell suicide. Caspases chop apart the cellular proteins which maintain the structural and functional integrity of the cell and carry out key cellular tasks like DNA repair and cell adhesion. Until recently, malignancies were histologically graded using cell replication and cell differentiation as indicators. It is now clear that increased cell replication is not the only explanation for the loss of tissue homeostasis in cancer: an equally important role is the disturbance of the cell death mechanisms. In fact it is quite intriguing that evidence shows that the apoptotic mechanism may never be completely inactivated; instead its threshold for activation is set

higher, such that most oncological treatments capable of inducing apoptosis (*e.g.* chemo- and radiotherapy) become ineffective.

*For all these reasons, there is an increased interest in searching for a simple and effective method of specific identification and quantification of cell proliferation and deletion that can be used routinely in oncological patients.*

Recently, the capacity of malignant cells to escape the effects of chemotherapy, radiation (in this case, radiosensitivity) or other hormone treatment, has been related to their capacity of escaping apoptosis. As far as radiation is concerned, despite the large variations among malignancies, there is good evidence that there is a strong correlation between radio-curability and the *magnitude* of apoptotic response. Depending on the dose, radiation can induce apoptosis or oncosis. At small to moderate doses, apoptosis is induced in both normal tissue and malignant neoplasm. The way in which radiation triggers apoptosis is not completely understood, but it is believed to be related to the damage inflicted at the level of DNA.

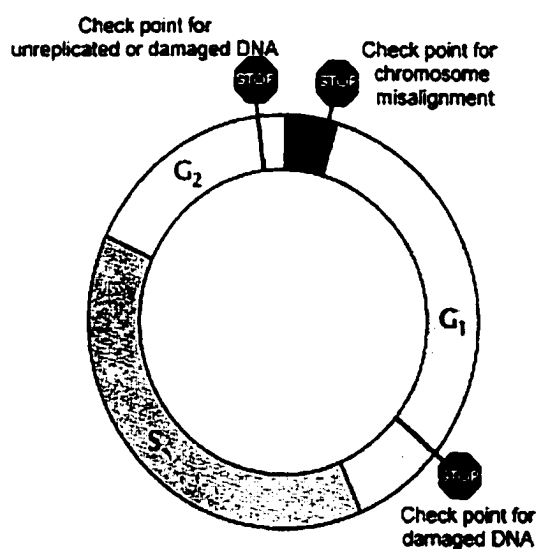


**FIG. 7.** Few checkpoints function in order to ensure that complete and correct genome is transmitted. The proliferation of most cells is regulated primarily in G<sub>1</sub> but some cell cycles are controlled in G<sub>2</sub>. In mammalian cells, arrest in G<sub>1</sub> is mediated by p53, which is rapidly induced in response to DNA damage. Mutations in p53 are very frequent in human cancers, thus contributing to genome instability and cancer development.



When DNA is damaged, the cell is arrested at G<sub>1</sub> phase to allow extra time for the repair of DNA (as seen in Figure 7).

Ischemic cell death - oncosis - is characterized by swelling (this explains how Von Recklinghausen coined the term oncosis about 100 years ago). This type of early response follows a variety of injuries (heat, toxins, ischemia, etc.) applied *in-vivo* or *in-vitro*. The main difference between oncosis and apoptosis seems to be whether or not the injury primarily (or secondarily) interferes with ATP synthesis and failure of the ionic pumps in the plasma membrane ( $[Na^+]$  regulation). The sequence of functional and biochemical changes take place quickly after injury (minutes). The oncotic death, defined functionally by the point of no return, occurs long before necrosis and *it is not detectable* histologically. In rat liver for example, it takes about 120-150 min to reach the point of no return; the swelling however takes place for 6 to 7 hours, and then it loses water (sign of massive membrane breakage) and shrinks. The cells die early in the swelling process. ATP is typically reduced, in some cases as ischemia of kidney *in vivo*, quickly becomes non measurable. A direct consequence is loss of control of ions and water regulation. The timing of this stage depends on the type of injury and whether the plasma membrane permeability is affected. Increased concentrations of  $Na^+$ ,  $Cl^-$  and  $H_2O$  in the cell are accompanied by decreased levels of  $K^+$ . In parallel,  $[Ca^{2+}]_i$  increases due to increase entry from the extracellular space; the increase can be from 100 nM in most cells to mM levels. There are also enzymes leaking<sup>11</sup> from the cell even in the case of relatively mild, reversible injury.

A number of studies [15, 16, 17, 18] have put in evidence a mechanism of radiation-induced damage at the level of the level of plasma membrane. The currently accepted explanation for radiation-induced membrane damage is lipid and protein peroxidation by highly reactive free radicals. This leads to increased cell membrane permeability, which results in metabolic exhaustion, an increased production of reactive oxygen intermediates and the onset of necrosis. It was also recently recognized that the

---

<sup>11</sup> These are the "liver enzymes", "cardiac enzymes", etc., that a lab measures to determine the presence and extent of injury in the clinical setting. Skeletal muscle enzymes rise after a workout, and liver enzymes after a beer party, but in neither case is there microscopic evidence of cell death.

cell membrane may be an important target for at least one pathway of radiation-induced apoptosis [19].

It is generally accepted that the type of prelethal phase (apoptosis or oncosis) following radiation injury has dose dependence, in that lipid peroxidation-mediated permeabilization of cell membranes is associated with intense ionizing irradiation. In [16], Canaday *et al.*, showed with irradiated postmitotic muscle cells that there is a lag time between irradiation and the onset of membrane permeability changes. The lag time is between 5-35 minutes, also with a dose dependency. The model they used considers radiation-induced poration followed by diffusional coalescence; a breakdown of membrane integrity occurs only when there are enough local pores, which coalesce into one of critical size. The process seems to depend both on dose and temperature. It is also interesting to notice that the existence of the lag time is a feature encountered also in the TRAP (total peroxy radical-trapping potential) assay [20]. Antioxidants prevent modification of low density lipoprotein (LDL) by free radicals. The TRAP assay is meant to quantify the capacity of human serum to resist attacks by free radicals, by measuring the length of time that a subject's serum is able to resist artificially induced peroxidation. In this case, the lag time is related to the concentration of antioxidants in the sample.

To review the important information in this chapter, we have to point out again that there are two pathways towards cellular death: apoptosis and oncosis. They are very much different in the sequence of changes occurring after irradiation. The nature and chronology of these changes are such that they evolve fast thus rendering histopathological investigations of little help. Giving the widespread use of the radiation treatment, *there is an increased interest in searching for a simple and effective method of specific identification and quantification of cell proliferation and deletion that can be used routinely in oncological patients.* In the experimental section we present evidence that Electrical Impedance Spectroscopy, has the potential of monitoring in real time, the subtle changes that can lead to the recognition of the two pathways to cellular death. The advantage can be an increased awareness of the response of the organism to radiation therapy before necrosis is installed and late changes become obvious; the feedback provided *during* the treatment can lead to the customization of the dose delivery, in terms of both magnitude and timing. Further *in vivo* studies are needed, to correlate the very

early changes we detected in the parameters modeling the dielectric response following irradiation, with evidence for apoptosis or necrosis and morphological changes.

## CHAPTER III

### DIELECTRIC PROPERTIES OF MATTER

The aim of this chapter is to present the main tools used in dielectric spectroscopy in order to assign dielectric dispersion to biological structures and to identify the processes taking place in these structures. Historically, Fricke [21] was the first one, in 1925, to show by impedance measurements that cells are surrounded by a thin, insulating membrane.

#### Dielectric properties, a practical definition

The electrical properties, conductivity  $\sigma$  and permittivity  $\epsilon$ , of a material, can be determined by placing the material between the plates of a capacitor and measuring its resistance  $R$  and capacitance  $C$ :

$$R = \frac{l}{\sigma A} \frac{d}{A}, \quad \text{and} \quad C = \frac{\epsilon_0 \epsilon A}{d}. \quad (14)$$

The conductivity  $\sigma(\omega) = \sigma_{DC} + \omega \epsilon_0 \epsilon''(\omega)$  (measured in  $\Omega^{-1}/m$  or  $S/m$  in SI) measures the easiness with which free charge carriers can move through the material under the influence of the external applied field, thus being the proportionality factor between the electric field and electric current. The permittivity  $\epsilon$  (measured in units of  $\epsilon_0$ ) is, following a similar reasoning, the proportionality factor between the electric field and localized charges, reflecting the extent at which the charge distributions can be distorted by polarization. For non-polar materials, the increase in the capacitance results from the polarization of the molecular structure, in the form of atomic and electronic polarization. In the case of the polar materials, the component molecules possess a permanent dipole moment, and their polarization response will have an orientational polarization component in addition to the polarizations already mentioned for non-polar materials.

If one now applies an electric field with increased frequency  $E = E_0 e^{i\omega x}$ , there will be a phase shift  $\delta$  between the applied field  $E$  and polarization. The dielectric displacement  $D$

can thus be written  $D = D_0 e^{i(\omega t - \delta)}$ . The experimentally accessible quantity is  $\epsilon$ , defined as the ratio  $D/E$ , which is therefore complex if the phase is non-zero. Anisotropic systems would normally require a tensor for  $\epsilon$ , but for biological materials, this can be safely considered a complex scalar  $\epsilon = |\epsilon| e^{-i\delta} = \epsilon' - i\epsilon''$ . Figure 8 illustrates a typical frequency dependence of the complex permittivity  $\epsilon = \epsilon' - i\epsilon''$  for a pure polar liquid. The frequency scale as well as the characteristic dispersion frequency is arbitrary. The consequent reduction of the permittivity and the increase in absorbed energy is referred to as *dispersion* (or dielectric relaxation). As we expect the 'slowest' one is the orientational or dipolar polarization. Depending whether the molecules are bulky macromolecules like DNA or smaller molecules, like the water molecule, the fall-off of the orientational polarization can occur in a frequency range from 0.01 Hz to  $10^{11}$  Hz. The atomic and electronic dispersions occur in IR (infrared, about  $10^{14}$  Hz) respectively visible, UV ( $>10^{15}$  Hz). For dielectric studies, the dipolar relaxation is interesting because information about the dipoles and their environment is contained in both the frequency and the shape of the dielectric dispersion.

Most molecules of biological interest possess an electric dipole, which in general gives rise to a high dielectric constant and a well-defined dispersion region [22]. The magnitude of the dipole moment  $\mu$  depends on the size of the molecule and on its distribution of charge. A convenient unit for  $\mu$  is the Debye (D), representing a SI value of  $3.33 \cdot 10^{-30}$  Cm; an electron  $e$  displaced for one Å ( $10^{-10}$  m) would have a dipole moment of 4.8 D. Thus, a water molecule has approximately 2D, hemoglobin (68000-molecular weight) several hundred D, and DNA (molecular weight  $2 \cdot 10^6$ ) roughly 105 D.

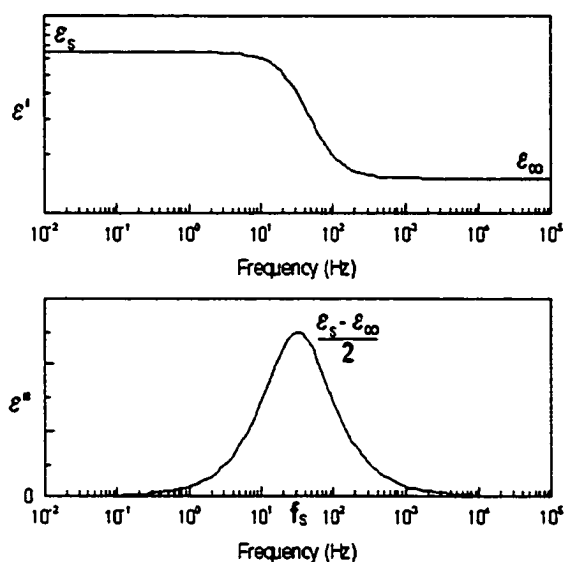


FIG. 8. The frequency dependence of the complex permittivity  $\epsilon = \epsilon' - i\epsilon''$  for a pure polar liquid

As shown, the dielectric constant  $\epsilon'$  falls from a high value  $\epsilon_s$  (the static dielectric constant) to  $\epsilon_\infty$  (the high frequency dielectric constant) as the frequency increases through the dispersion region. When dispersion occurs there is a phase lag between the motion of the dipoles and the applied field, with a consequent loss of energy. The lower curve shows the variation of the fractional *energy absorption per cycle*  $\epsilon''$ , the frequency corresponding to the maximum absorption being termed the *relaxation frequency*  $f_s$ . Corresponding to this parameter is a relaxation wavelength  $\lambda_s = c/nf_s$ , and a relaxation time  $\tau_s = 1/2\pi f_s$ .

These three quantities  $\epsilon_s$ ,  $\epsilon_\infty$  and  $\tau$  as well as the shape of the dispersion curve are related to various molecular parameters, so a study of the dielectric behavior of a substance can be used to provide information at the molecular level. In the context of the large  $\epsilon$  values, typically encountered in biological solutions or tissue structures characterizing the low frequency dispersion, we should note that these high values of the dielectric constant, do not come from the existence of permanent dipoles – there are other polarization mechanisms that can give rise to high dielectric constants but have nothing to do with dipole rotation (*e.g.* Maxwell-Wagner effect, discussed later).

### The Debye Dispersion

The simplest case is a single dispersion region, a relaxation process characterized by a single relaxation time associated with viscous damping of one species of polar molecules as they try to align with the applied field, which conforms to the Debye equations [23]:

$$\epsilon' = \epsilon_{\infty} + \frac{\epsilon_S - \epsilon_{\infty}}{1 + \left(\frac{\lambda_S}{\lambda}\right)^2} \quad \text{and} \quad \epsilon'' = \frac{\epsilon_S - \epsilon_{\infty}}{1 + \left(\frac{\lambda_S}{\lambda}\right)^2} \frac{\lambda_S}{\lambda}, \quad (15)$$

which are derived from :

$$\hat{\epsilon} = \epsilon' - i\epsilon'' = \epsilon_{\infty} + \frac{\epsilon_S - \epsilon_{\infty}}{1 + i\left(\frac{\lambda_S}{\lambda}\right)}. \quad (16)$$

Expressing  $\epsilon'$  and  $\epsilon''$  explicitly as functions of  $\omega$ :

$$\epsilon' = \epsilon_{\infty} + \frac{\epsilon_S - \epsilon_{\infty}}{1 + \omega^2 \tau^2}; \quad \epsilon'' = \frac{(\epsilon_S - \epsilon_{\infty}) \omega \tau}{1 + \omega^2 \tau^2}, \quad (17)$$

and eliminating  $\omega\tau$  between them, we obtain:

$$\left[ \epsilon' - \frac{(\epsilon_S - \epsilon_{\infty})}{2} \right]^2 + (\epsilon'')^2 = \left[ \frac{(\epsilon_S - \epsilon_{\infty})}{4} \right]^2, \quad (18)$$

which represents the basis for a widely used representation of the dielectric constants  $\epsilon'$  and  $\epsilon''$ , the so-called *Cole-Cole* plot, a semicircle with its center on the  $\epsilon'$  axis if the Debye equation are obeyed. When deviations from the pure Debye behavior were measured, the most straightforward way of tweaking the Debye function was to invoke a spread of the relaxation times.

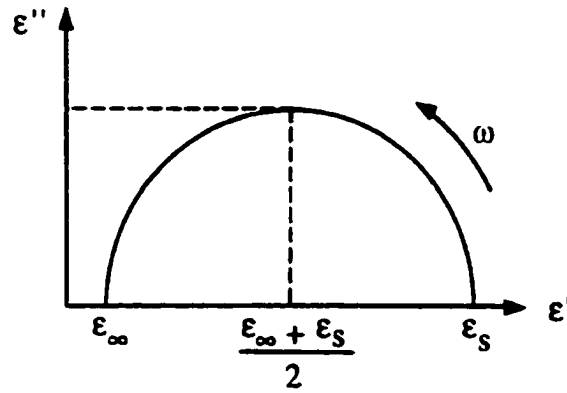


FIG. 9. Cole-Cole plot ( $\epsilon''$  vs.  $\epsilon'$ ) of complex permittivity.

### Cole-Cole dispersion

Several distribution functions are available. Cole and Cole [24, 25] have deduced the following phenomenological equation, introducing an empirical coefficient  $\alpha$  in Eq. (16):

$$\hat{\epsilon} = \epsilon' - i\epsilon'' = \epsilon_\infty + \frac{\epsilon_s - \epsilon_\infty}{1 + \left[ i \left( \frac{\lambda_s}{\lambda} \right) \right]^{1-\alpha}}, \quad (19)$$

where  $\alpha \in [0,1]$  and is a measure of the spread of the relaxation times.

Figure 10 shows the variation of the dispersion shape as a function of  $\alpha$ :



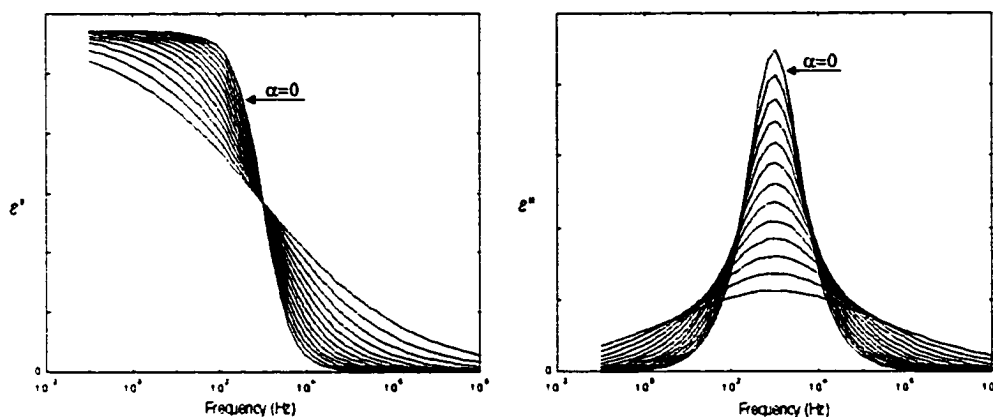


FIG. 10. Variation of the dispersion and absorption plots for values of  $\alpha \in [0,1]$ .

In the Cole-Cole plot shown in Fig. 11, the semicircle become depressed as  $\alpha$  increases:

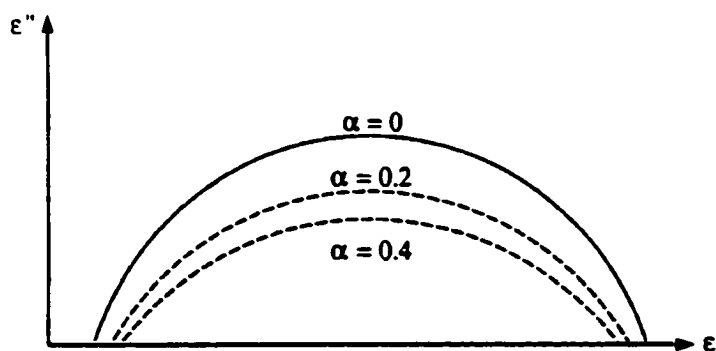


FIG. 11. The depressed semicircular behavior is characteristic for many biological materials.

Lets consider now the type of relation that one would expect between dielectric properties and molecular structure.

The static dielectric constant ( $\epsilon_s$ ) is dependent upon the molecular dipole moment ( $\mu$ ) and the type of short-range structure present. For an ideal system such as a polar gas

or a very dilute solution of polar molecules in a non-polar solvent, the polarization is given by the Debye equation [23]:

$$P = \frac{\epsilon_s - 1}{\epsilon_s + 2} \frac{M}{\rho} = \frac{4\pi}{3} N \left( \alpha + \frac{\mu^2}{3kT} \right), \quad (20)$$

with  $P$ -molar polarization,  $M$  the molecular weight in grams,  $\rho$  the density and  $\alpha$  the molecular polarizability or induced moment per molecule per unit field. It can be seen that the polarization can be split up into 2 parts corresponding to induced dipoles and permanent dipoles, the former being due to atomic and electronic displacement. Unfortunately, this equation is based on assumptions (concerning intermolecular forces) that do not hold in the case of biological liquids. When formulating his equation, Debye [26] accepted the Clausius–Mossotti expression for the electric field acting on a given molecule in a dielectric

$$E_i = \frac{\epsilon_s + 2}{3} E, \quad (21)$$

where  $E$  is the external field. Later Onsager [27] showed that the relation should be replaced by

$$E_i = \frac{3\epsilon_s}{2\epsilon_s + 1} E, \quad (22)$$

from which he deduced the following equation for the dipole moment in terms of  $\epsilon_s$ :

$$\mu^2 = \frac{9kT}{4\pi s} \frac{(\epsilon_s - n^2)(2\epsilon_s + n^2)}{\epsilon_s (n^2 + 2)^2} \quad (23)$$

with  $n$ - the refractive index in far infrared, and  $s$  the number of molecules per ml.

Onsager's theory [27] shows that the dominant term in the expression for dielectric constant should be the square of the dipole moment of the molecule in the gaseous state ( $\mu$ ). However, the equation breaks-down with hydroxylic liquids which precludes its use for biological molecules, where hydrogen bonds play such an important role. Various

attempts were made to modify Onsager's law, the most well known being due to Kirkwood [28]:

$$\frac{(\epsilon_s - 1)(2\epsilon_s + 1)}{9\epsilon_s} = \frac{4\pi s}{3} \left( \alpha + \frac{g\mu^2}{3kT} \right). \quad (24)$$

The factor  $g$  is called the correlation parameter and equals one for a molecule undergoing free rotation. The departure from unity is a measure of the degree of intermolecular attraction and its value must be deduced from a model for the liquid structure. For the associated liquids, for a given set of dielectric data it may be possible to envisage several alternative molecular models that fit the facts equally well.

### **Non-Debye mechanisms**

The above examples were restricted to small inorganic molecules but the same kind of ideas can be extended to molecules of biological interest. It should not be assumed, however, that a large  $\epsilon_s$  necessarily implies the existence of permanent dipoles; other mechanisms of polarization exist which give rise to high dielectric constants but which have nothing to do with dipole rotation. An example is the Maxwell-Wagner effect which will be discussed in more detail in the next section. In the cluster model of relaxation (for both bulk and barrier properties), the Maxwell-Wagner response represents a limiting case, only applicable when the series elements are perfect, non-dispersive capacitors and resistors.

A broad classification of dispersions can be made according to the dominant physical processes:

- Debye - the frequency dependence is due to the orientation processes of electric dipoles associated to molecules or other structures in external electric fields;
- Maxwell-Wagner - its frequency dependence is due to the heterogeneous structure and hierarchical organization of tissues.

Another appropriate classification would have been Debye and non-Debye relaxation processes. The reason is that there is a wealth of phenomena in the physics of condensed

matter dealing with a 'universal' non-Debye relaxation, basically a non-exponential decay of the depolarization current (for dielectrics) following the removal of the polarizing field. While in the Debye mechanism, the time domain response function is of the type  $\Psi(t) \propto e^{-t/\tau}$ , the typical non-Debye relaxation is characterized [29] by the response function  $\Psi(t) \propto t^{-n}$ , leading to a susceptibility  $\chi'(\omega) \propto \chi''(\omega) \propto \omega^{-n+1}$ . In general, the causes for the a non-Debye behavior can be considered due to:

1. An inhomogeneous mechanism: the distribution of relaxation times, probably the oldest and most phenomenological explanation. The individual dipoles relax exponential (Debye) but the relaxation time is different from dipole to dipole due to spatial inhomogeneities. Thus the result of the non-Debye behavior is to be attributed to superposition.
2. A homogeneous mechanism based on defect-diffusion controlled relaxation. The elementary dipole, re-orienting under the usual Debye-like rotational diffusion, relaxes completely after an encounter with a defect. In its essence a diffusive-reactive process, it is also highly dimensionality dependent.

Another possible classification, particular helpful for our applications, uses as criteria the frequency at which these dispersions occur. Schwan has shown [30] that most biological materials exhibit 3 dispersion regions ( $\alpha$ ,  $\beta$  and  $\gamma$ , seen in Figure 12), which occurs at Hz, kHz-MHz and GHz frequencies, respectively. A fourth one,  $\delta$ , occurring between the  $\beta$  and  $\gamma$  regions is acknowledged for a number of systems (*e.g.* protein solutions) and some authors discuss about sub-ranges of  $\beta$ :  $\beta_1$ ,  $\beta_2$ . Even though the original idea was to assign these ranges to certain polarization mechanisms, due to a number of factors (*e.g.* distribution of molecule or cell sizes) there are no clearly defined boundaries.

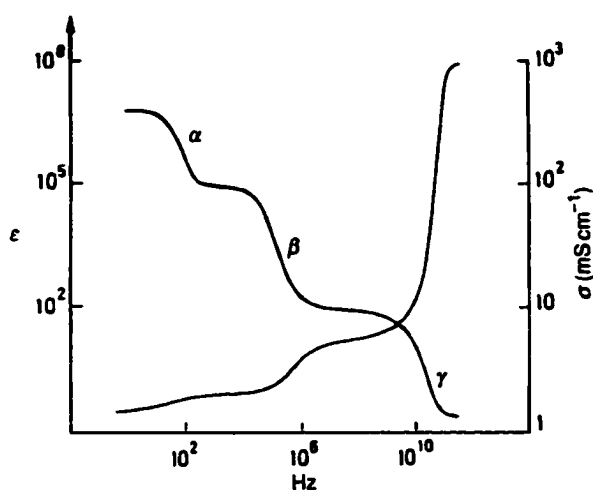


FIG. 12. Typical dielectric spectrum for tissues (adapted from [30]).

The  $\alpha$  dispersion is believed to occur from mHz to kHz frequencies. Despite of the apparent accessibility, it is very difficult to model this region because of the many different processes playing a role: electrode polarization, particle electrophoresis, electrolytic processes, hydrodynamic relaxations of the field induced convections, and the impossibility of isolate the different contributions. Schwan initially suggested [31] the responsible with the  $\alpha$  dispersion is the polarization of counterions near the cells surface (see reference to the counterion polarization). In muscle cells, where the low frequency dispersion is especially strong and orientational dependent, another source could be the polarization of the sarcotubular<sup>12</sup> system. The  $\alpha$  dispersion is a very striking feature in the permittivity data (for tissues  $\epsilon_r$  can reach  $10^6$ - $10^7$ ). Due to the strong ionic conductivity of the tissue electrolyte, the  $\alpha$  dispersion is not present in the conductivity, the results being that tissue conductivity at these frequencies exhibits an almost entirely resistive behavior with very small contributions from displacement currents.

<sup>12</sup> A complex system of membranes, vesicles and tubules that permeates the cytoplasm of a muscle cell (sarcoplasm) and connects to the exterior of the cell

In the frequency range corresponding to the  $\beta$  dispersion, the relaxation is essentially due to the capacitive charging of cell membranes, its origin lying in the structure of the cell in which an interface - the plasma membrane - separates two conducting media. When the frequency increases, the capacitive reactance decreases, which in turn determine an increase current in the intracellular space. The increase in conductivity is also accompanied by a decrease of the permittivity, since at high frequency the cell walls don't have the time to fully charge during a cycle. The cell aggregate composing the tissue is clearly an heterogeneous medium in which the relaxation is based on Maxwell-Wagner interfacial polarization. Towards higher frequencies, also contributing is the dipolar reorientation of the proteins and cell organelles. There is a strong overall dependence of the  $\beta$  dispersion to the physical integrity of the membranes.

The high frequency dispersion (UHF and microwave) is due to the dielectric relaxation of water. Pure water relaxes at about 20 GHz at 25 °C and has an (almost) pure Debye behavior. For tissue with high water content, at these frequencies, the conductivity is due to both dipolar loss and to ionic conduction.

### **Interfacial Polarization. The Maxwell-Wagner Theory**

The permanent electric dipole moment (when it exists) of a number of biological polymers cannot explain the high polarization of these molecules, especially at low frequencies. A theory which is based on the concept of interfacial polarization of inhomogeneous materials has been developed in order to explain the unusual dielectric properties of these substances.

In this section we will discuss the classical Maxwell-Wagner polarization mechanism. Later, it will be shown that from the more general standpoint of transport across fractal interfaces (percolation, cluster, etc.). Maxwell-Wagner theory represents in fact a limiting case, only applicable when the series elements are perfect, non-dispersive capacitors and resistors.

Many biological materials do not have a permanent electric dipole moment, yet when dissolved or suspended in aqueous media, they exhibit a dielectric constant which

is far larger than that of the solvent. This strange behavior seems not to be only related to biological systems, but also to simpler systems (*e.g.* suspension of latex or polystyrene particles) which do not have a permanent dipole moment but exhibit an exceedingly large dielectric constant and an anomalous dispersion. These observations cannot be explained by the theory of polar molecules, the so-called Debye behavior. The dielectric analysis of colloids and suspensions in the frequency range corresponding to the Maxwell-Wagner polarization [32] can bring information about the size and shape of the particles, the colloid-solvent interface and the ions distribution around the particle surface.

How can we describe an inhomogeneous dielectric material? First of all, these systems must have discrete domains (barriers, layers), separating regions with different dielectric constants and/or conductivities. In the case of the suspension of particles, for example, there is a sharp boundary at their surface. The solvent phase can be considered a dielectric continuum.

A simple barrier model (for wavelengths much larger than the size of the dimensions of the capacitor) is a system with two slabs having different dielectric properties in contact with each other, as shown in Figure 13.

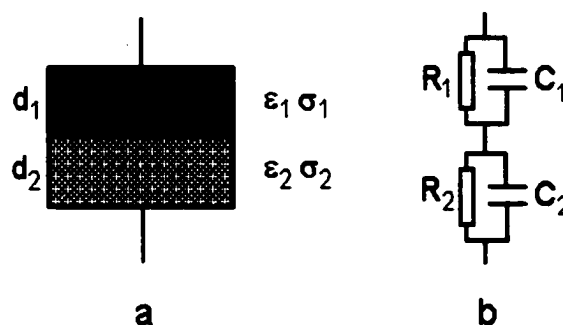


FIG. 13. A leaky condenser - the simplest model for interfacial polarization.

In this figure,  $\epsilon_1$ ,  $\sigma_1$ ,  $\epsilon_2$ ,  $\sigma_2$  are the dielectric constants and conductivities of these slabs respectively. The equivalent circuit of this system is shown in Fig. 13. Each slab is represented by a leaky condenser (a capacitor and resistor are connected in parallel). The

measured impedance of such a system at a given frequency is resolved into equivalent parallel capacitance  $C_p$  and resistance  $R_p$  to evaluate the dielectric constant from the following equations:

$$\varepsilon' = \frac{C_p}{C_0}; \quad \varepsilon'' = \frac{1}{\omega C_0 R_p}, \quad (25)$$

where  $C_0$  is the geometrical capacitance of the sample.

Assuming no true charges on the interface and an isotropic dielectric, the continuity of  $\mathbf{D}$  requires:

$$\varepsilon_1 E_1 = \varepsilon_2 E_2. \quad (26)$$

Thus, the current densities at the interface are:

$$\frac{j_1}{j_2} = \frac{\sigma_1 E_1}{\sigma_2 E_2} = \frac{\sigma_1 \varepsilon_2}{\sigma_2 \varepsilon_1}, \quad (27)$$

so, whenever  $\sigma_1 \varepsilon_2 \neq \sigma_2 \varepsilon_1$  the interface will be charged at a rate proportional with  $j_1 - j_2$ . If the unlikely condition  $\sigma_1 \varepsilon_2 = \sigma_2 \varepsilon_1$  is satisfied, no Maxwell-Wagner effect is observed. The equivalent permittivity  $\varepsilon$  and conductivity  $\sigma$  of the system can be found by regarding the two capacitors in series:

$$\frac{d_1 + d_2}{\varepsilon + \frac{\sigma}{i\omega}} = \frac{d_1}{\varepsilon_1 + \frac{\sigma_1}{i\omega}} + \frac{d_2}{\varepsilon_2 + \frac{\sigma_2}{i\omega}}. \quad (28)$$

To further simplify the formulae, we will consider  $d_1 = d_2 = d$  and will seek the complex permittivity of the Debye form:

$$\varepsilon = \varepsilon_\infty + \frac{\varepsilon_s - \varepsilon_\infty}{1 + i\omega\tau}. \quad (29)$$

By identification, the following formulae are obtained:



$$\varepsilon_{\infty} = \frac{\varepsilon_1 \cdot \varepsilon_2}{\varepsilon_1 + \varepsilon_2}; \quad \varepsilon_s = \frac{(\varepsilon_2 \sigma_1 - \varepsilon_1 \sigma_2)^2}{(\sigma_1 + \sigma_2)^2 (\varepsilon_1 + \varepsilon_2)}; \quad \tau = \frac{\varepsilon_1 + \varepsilon_2}{4\pi(\sigma_1 + \sigma_2)}. \quad (30)$$

Considering  $\varepsilon_1 \cong 3$ ,  $\varepsilon_2 \cong 95$ ,  $\sigma_1 \cong 10^{-7}$  S/m and  $\sigma_2 \cong 0.1 \cdot 10^{-9}$  S/m, one can obtain a maximum loss factor  $\varepsilon_m = 1/2(\varepsilon_1 - \varepsilon_{\infty})$  rising from  $10^{-5}$  at a frequency  $f_m = 1/2\pi\tau$  of 6 Hz to almost 400 at  $10^{-2}$  Hz. Even though we can imitate the Debye expression, it's obvious that the meaning of the parameters involved has nothing to do with the dipolar moment and that the apparent dielectric relaxation obtained is an interface phenomena.

The two slab model can seldom be of use in modeling real systems, so our next step will be to find the dielectric properties of a dilute mixture of non-interacting spherical particles. The well-known mixture equation was derived by Maxwell (1892):

$$\frac{\varepsilon_1^* - \varepsilon^*}{2\varepsilon_1^* + \varepsilon^*} = p \frac{\varepsilon_1^* - \varepsilon_2^*}{2\varepsilon_1^* + \varepsilon_2^*}, \quad (31)$$

where  $\varepsilon^*$  is the complex permittivity of the mixture, the indices 1 and 2 are used for solvent and suspended particles respectively, and  $p$  is the volume fraction of the particles. Maxwell originally derived the equation above for real dielectric constants of the two media. Solving for  $\varepsilon^*$ , we obtain:

$$\varepsilon^* = \varepsilon_1^* \frac{(2\varepsilon_1^* + \varepsilon_2^*) - 2p(\varepsilon_1^* - \varepsilon_2^*)}{(2\varepsilon_1^* + \varepsilon_2^*) + p(\varepsilon_1^* - \varepsilon_2^*)}. \quad (32)$$

For small  $p$  the previous relation reduces to:

$$\varepsilon^* = \varepsilon_1^* \left( 1 + 3p \frac{(\varepsilon_2^* - \varepsilon_1^*)}{(2\varepsilon_1^* + \varepsilon_2^*)} \right). \quad (33)$$

The difference between the exact formula and the approximation used for small  $p$  can be seen in the Figure 14.

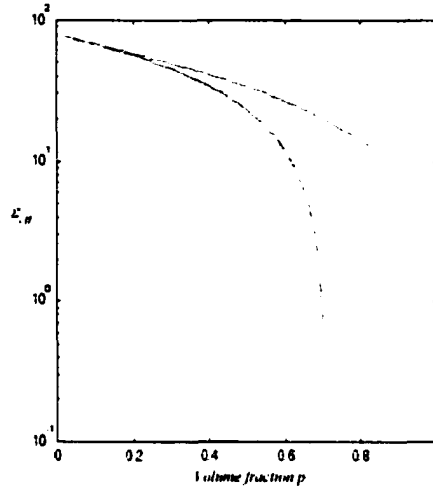


FIG. 14. The exact  $\epsilon^*$  is physically correct, while the approximation can only be used for  $p < 0.2$ . In this example  $\epsilon_1 = 78.5$  and  $\epsilon_2 = 3.0$

The generalization of Maxwell's theory, written for real dielectric constants, is due to Wagner [33], who essentially replaced  $\epsilon^*$  with  $\epsilon + 4\pi \frac{\sigma}{i\omega}$  and obtained a Debye-like expression:

$$\epsilon = \epsilon_{\infty} + \frac{\epsilon_s - \epsilon_{\infty}}{1 + i\omega\tau}, \quad (34)$$

in which

$$\begin{aligned} \epsilon_{\infty} &= \epsilon_1 \left( 1 + 3p \frac{\epsilon_2 - \epsilon_1}{2\epsilon_1 + \epsilon_2} \right), \\ \Delta\epsilon = \epsilon_s - \epsilon_{\infty} &= 9p \frac{(\epsilon_1\sigma_2 - \epsilon_2\sigma_1)^2}{(2\sigma_1 + \sigma_2)^2 (2\epsilon_1 + \epsilon_2)}, \\ \tau &= \frac{2\epsilon_1 + \epsilon_2}{4\pi(2\sigma_1 + \sigma_2)}, \end{aligned} \quad (35)$$

are in fact approximations of the exact formulae for small  $p$ .

At this point it is interesting to notice that the frequency of the maximum dielectric loss  $f_m = 1/2\pi\tau$  is independent (in the small  $p$  approximation, but it doesn't vary significantly in the exact formulation) of the concentration of the dispersed components, which represents an important feature of the interfacial polarisation in heterogeneous systems.

### *The Maxwell-Wagner theory for suspensions of ellipsoidal particles*

Even though a dilute suspension of spherical particles seems more suitable to model real systems, biological cells as well as the polyions have complex geometries that cannot be approximate by spheres. Since many structures are elongated or disc-shaped, the next best choice seems to be an ellipsoid (Figure 15). The following ellipsoidal model can be used:

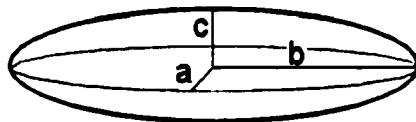


FIG. 15. Model for the ellipsoidal particles

and the field is considered to be applied along the x axis. The idea of the calculus is the same as for the sphere: one estimates the potential of one large ellipsoid with an (effective) dielectric constant  $\epsilon^*$  in a point P at a distance  $r$  from the center. On the other hand, in the same point, the potential due to  $N$  small particles is evaluated by superposition. The two potentials, even though calculated by different methods, have to be the same, and this is the relation leading to  $\epsilon^*$ . With the notation:  $p = Nv/V$  ( $v$ -volume of particle,  $N$ -no. of particles and  $V$ -volume of the large ellipsoid),  $n = 4\pi/l_a$  and

$$L_a = \int_0^{\infty} \frac{d\xi}{(a^2 + \xi)\beta(\xi)} \quad \text{where} \quad \beta(\xi) = \frac{\sqrt{(a^2 + \xi)(b^2 + \xi)(c^2 + \xi)}}{abc/2}. \quad (36)$$

For simplicity, medium 1 will be considered a pure insulator  $\varepsilon_1^* = \varepsilon_1$  and medium 2 with non-zero conductivity  $\varepsilon_2^* = \varepsilon_2 + \frac{4\pi\sigma_2}{i\omega}$ . The following components of  $\varepsilon$  are obtained:

$$\varepsilon' = \varepsilon_{\infty} + \varepsilon_1 \frac{\Delta\varepsilon}{1 + (\omega\tau)^2} \quad \text{and} \quad \varepsilon'' = \frac{\varepsilon_1 \Delta\varepsilon \cdot \omega\tau}{1 + (\omega\tau)^2}. \quad (37)$$

where

$$\varepsilon_{\infty} = \varepsilon_1 \left( 1 + p \frac{n(\varepsilon_2 - \varepsilon_1)}{(n-1)\varepsilon_1 + \varepsilon_2} \right), \quad (38)$$

$$\Delta\varepsilon = \varepsilon_2 - \varepsilon_{\infty} = p \frac{n^2 \varepsilon_1}{(n-1)\varepsilon_1 + \varepsilon_2}, \quad (39)$$

and

$$\tau = \frac{(n-1)\varepsilon_1 + \varepsilon_2}{4\pi\sigma_2}. \quad (40)$$

### *Concentrated suspensions*

The Maxwell-Wagner theory was developed with the assumption of small concentration of suspending particles in solution (which in turn implies non-interacting particles). It was found later that it can be applied for high concentration, even though rigorously, it is true only for small volume fractions  $p$ . Hanai [34] extended Maxwell's theory for high volume fractions. The relation between  $\varepsilon^*$ -the dispersion of the suspension, and  $\varepsilon_1^*, \varepsilon_2^*$ -the dispersion of the solvent respectively the suspended particle is:

$$\frac{\varepsilon_1^* - \varepsilon_2^*}{\varepsilon_1^* - \varepsilon_2^*} \left( \frac{\varepsilon_1^*}{\varepsilon_2^*} \right)^{\frac{1}{3}} = 1 - p, \quad (41)$$

which leads to solving a third degree equation in  $\varepsilon^*$ :

$$\varepsilon^{*3} - 3\varepsilon_2^* \varepsilon^{*2} + \left( 3\varepsilon_2^{*2} + \frac{[(p-1)(\varepsilon_1^* - \varepsilon_2^*)]^3}{\varepsilon_1^*} \right) \varepsilon^* - \varepsilon_2^{*3} = 0. \quad (42)$$

The frequency dependency is implicit, given that all the complex permittivities depend on  $\omega$ :

$$\varepsilon^* = \varepsilon + \frac{4\pi\sigma}{i\omega}. \quad (43)$$

### *Particles with surface conductivity*

Until now we discussed about mixtures (in fact colloids or suspensions) in which the suspended particles were characterized by only one set of dielectric parameters: the electric permittivity  $\varepsilon$  and conductivity  $\sigma$ . An important assumption was that the particles are not in contact with each other and are not forming clusters leading to conductive pathways between electrodes. A phenomenon which was not taken into consideration and which is of great importance in real cases (biological macromolecules or cells) is surface conductivity. Most of these systems are electrically charged (as a result of ionized surface chemical groups or adsorbed ions). The surface charges will attract counter-ions, forming an electrical double layer. Surrounding the particle with its double layer is the bulk volume of the electrolytic solution. The model is a particle with a thin conductive layer, shown in Figure 16.

The Laplace equation  $\nabla^2\Psi = 0$  has to be solved for each domain (1,2 and 3) along with the boundary conditions at  $r=R_1$  and  $r=R$ . The exact solution is difficult to obtain and unsuitable for practical applications. With few simplifying assumptions:

$$R_1 \gg d \text{ and } R \cong R_1 \cong R_2,$$

the effective values for the conductivity and permittivity of the particle are:

$$\sigma \equiv \sigma_3 + 2d\sigma_2/R \quad \text{and} \quad \epsilon \equiv \epsilon_3 + 2d\epsilon_2/R.$$

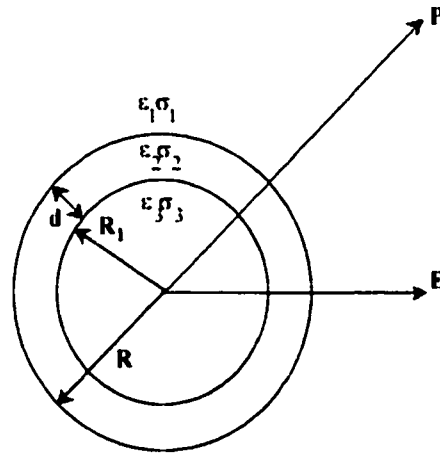


FIG. 16. Model for the double layered particle

Using the Maxwell-Wagner equations for mixtures of spherical particles, one obtains:

$$\epsilon_{\infty} = \epsilon_3 \left( 1 + 3p \frac{2d\epsilon_2/R}{3\epsilon_3 + 2d\epsilon_2/R} \right), \quad (44)$$

$$\Delta\epsilon = 9p \frac{(\epsilon_3(\sigma_3 + 2d\sigma_2/R) - (\epsilon_3 + 2d\epsilon_2/R)\sigma_3)^2}{(3\sigma_3 + 2d\sigma_2/R)^2 (3\epsilon_3 + 2d\epsilon_2/R)}, \quad (45)$$

$$\tau = \frac{2\epsilon_3 + \epsilon_1 + 2d\epsilon_2/R}{4\pi(2\sigma_3 + \sigma_1 + 2d\sigma_2/R)}. \quad (46)$$

In the mixture theory for the shell model, this should lead to two dispersion regions, but because of the large interval between them (the second is to be found at very high frequencies), it is very difficult to put both of them in evidence.

### *Counterion polarization*

As we already discussed, the real particles, immersed in electrolyte, are surrounded by a cloud of counterions. The distribution of these charges is in general such that it reaches a maximum at the Debye length ( $\lambda_D$ ) and then decreases with distance. The surface charge arise basically from the different affinities for electrons of the phases in contact, but a number of other mechanisms can play a role. For biological particles, the surface charge is determined mainly by the adsorption of ionizable chemicals. As a result, the electrostatic potential created by the surface charges will attract ions of opposite charge (counter-ions) and repel like ions (co-ions). When an external field is applied, the counterion cloud is distorted, the center of positive and negative charges gets shifted and causes an apparent (or induced) dipole moment, much larger than the intrinsic one. Within the double layer, two motions are possible: one radial the other tangential.

Assuming that  $n_o$  represents the equilibrium volume density of ions in the electrolyte and  $z$  the valence of the counterion, the volume density at some distance  $x$ , normal to the surface, will be:

$$n^+ = n_o \exp(-z^+ eV(x)/kT), \quad (47)$$

and similarly for the counterions

$$n^- = n_o \exp(-z^- eV(x)/kT), \quad (48)$$

we can see immediately that at any  $x$ ,  $n^+ n^- = n_o^2$

Considering  $z^+ = z^- = z$  the charge density  $\rho(x)$  becomes:

$$\rho(x) = e(z^+ n^+ - z^- n^-) = zen_o (\exp(-zeV(x)/kT) - \exp(zeV(x)/kT)), \quad (49)$$

and the Poisson equation

$$\frac{\nabla^2 V}{dx^2} = -\frac{\rho(x)}{\epsilon_0 \epsilon}, \quad (50)$$

with the boundary conditions

$$\begin{aligned} V(x \rightarrow 0) &= V_o, \\ V(x \rightarrow \infty) &= 0, \\ \left. \frac{\partial V}{\partial x} \right|_{x \rightarrow \infty} &= 0, \end{aligned} \quad (51)$$

will give

$$V(x) = \frac{2kT}{ze} \ln \left( \frac{1 + \gamma \exp(-x/\lambda_D)}{1 - \gamma \exp(-x/\lambda_D)} \right), \quad (52)$$

with

$$\gamma = \frac{\exp(zeV_o/2kT) - 1}{\exp(zeV_o/2kT) + 1}, \quad (53)$$

and

$$\lambda_D = \sqrt{\frac{\epsilon_0 \epsilon kT}{2z^2 e^2 n_0}}, \text{ being the Debye (screening) length.}$$

There are in fact a number of theories taking into account, with different degrees of complexity, the structure of the double layer and the motion of ions in its proximity. The double layer invoked here is involved in surface phenomena related to charged cells in an electrolyte. Equally important, surface phenomena occur at the interfaces between electrodes (normally a metal) used to impose an external field on a sample, and the electrolyte in which that sample is usually immersed. Reciprocally, many of the theories aim to explain the "electrode effects" can be as well used to explain phenomena in membrane and glycocalyx<sup>13</sup>.

---

<sup>13</sup> Glycocalyx - carbohydrate layer, covering the extracellular portion of the plasma membrane. Serves for both protection and as collection of markers for a variety of cell-cell interactions.



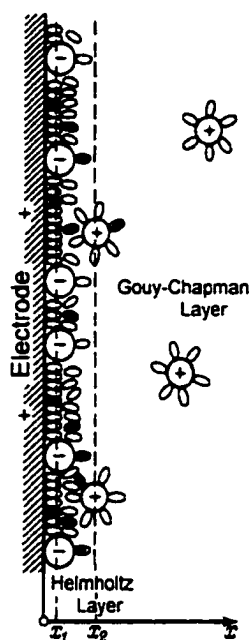


FIG. 17. Double layer structure at the electrode-electrolyte interface.

The Stern layer, shown in the Figure 17 as the one adjacent to the electrode, is a monolayer formed by the counter-ions adjacent to the charged surface. In the diffuse GC layer, the ions are still mobile and can participate to the thermal motion. These structures are modeled using ladder networks of capacitors, resistors and Constant Phase Angle (CPA) elements.

But how is, in fact, the surface conductivity and the counterion polarization modifying the dielectric response of the system? Two notable theories were developed, by O'Konski [35] and Schwartz [36]. The ideas of a hopping mechanism of conduction of the counterions along the particle surface and the reestablishment of the original surface charge distribution under the influence of diffusion, lead Schwartz to a diffusion limited relaxation time  $\tau$ :

$$\tau = \frac{r^2}{2D} = \frac{er^2}{2\mu_{ef}kT}, \quad (54)$$

where  $r$  is the particle radius,  $\mu_{eff} = \mu_0 e^{-E/kT}$ , the effective ionic mobility, and  $E$  is the potential energy barrier created by the overlapping of the coulomb wells of the surface charges. A pictorial is shown in the Figure 18, below: the formation of potential wells (a), the external field activated hopping motion of the counter-ions along the charged surface (b) and the polarization resulted from the net displacement of the counter-ions (c).

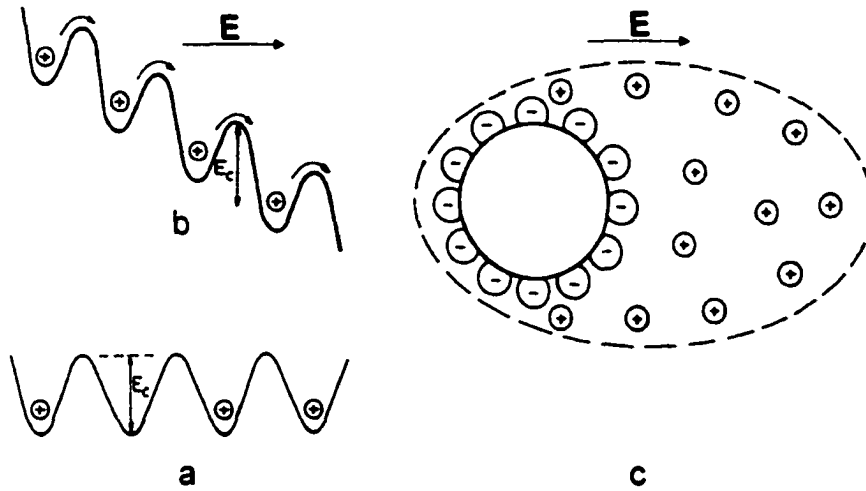


FIG. 18. Polarization by hopping activated surface conductivity (adapted from [32]). a) counterions in potential wells on the surface of a particle; b) when a field is imposed, the counterions can be activated and a tangential hopping motion can lead to surface conductivity; c) shows the polarization of the counterions determined by their net displacement under the effect of the externally applied field.

The polarizable counterion layer also adds a frequency dependent dielectric increment  $\Delta\epsilon$ , given by:

$$\Delta\epsilon = \frac{4\pi}{1+i\omega\tau} \frac{e^2 r \sigma_0}{kT}, \quad (55)$$

with  $\sigma_0$  the surface charge density in the absence of the electric field. For an arbitrary volume fraction  $p$ ,  $\Delta\epsilon$  becomes:

$$\Delta\epsilon = \frac{9}{4} \frac{4\pi p}{(1+p/2)^2} \frac{\sigma_0 e^2 r}{kT}, \quad (56)$$

We can see that the dielectric increment is proportional with  $r$ , while the relaxation time is proportional with  $r^2$ .

### Low Frequency Dispersion

For conducting samples, and biological materials in aqueous electrolytes fall into this category, low frequency dielectric dispersions are considered arising from ionic conduction effects. A numerical simulation of such effect is shown in Figure 19. The real part of  $\epsilon$  is not influenced by an increase of conductivity. The parameters chosen for simulation are:  $1-\alpha = 0.962$ ,  $f = 10^{-2}$ - $10^8$  Hz,  $f_c = 1$ kHz,  $\epsilon_\infty = 4$ ,  $\Delta\epsilon = 5.7 \cdot 10^4$  and the conductivity  $\sigma$  was varied from 10 to 200  $\text{Sm}^{-1}$  in 20 steps.

$$\epsilon(\omega) = \epsilon_\infty + \frac{\Delta\epsilon}{1 + i(\omega/\omega_c)^{1-\alpha}} + \frac{\sigma}{i\omega\epsilon_0}. \quad (57)$$

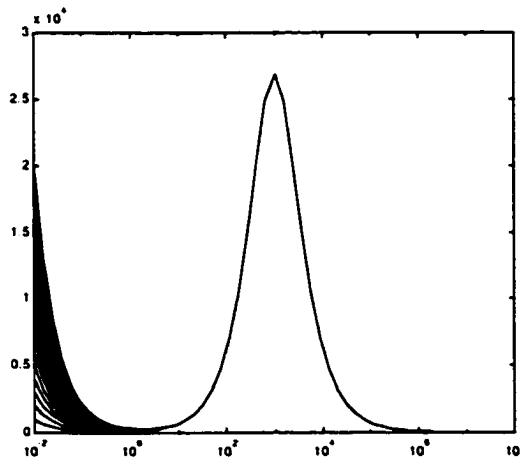


FIG. 19. Variation of  $\epsilon''$  with the frequency  $\omega$ . Shown is the  $\alpha$  dispersion and at very low frequencies the  $\Omega$  dispersions. The effect of the static conductivity is shown in the interval 70-1400S/m

Pethig [32] and earlier Onsager, in his Nobel prize lecture [37] pointed out that the  $\Omega$  dispersion is due to proton conduction processes. It was known that  $\Omega$  is associated with the generation and accumulation of ions at the sample-electrodes interface.

The low frequency dispersion (LFD) domain in general is still under debate, but a majority of researchers believe that  $\alpha$  has an underlying mechanism fundamentally different from  $\beta$ , and it is associated with the charge hopping between localized sites or clusters, rather than orientational relaxation of some permanent dipoles or more simply, the interfacial Maxwell-Wagner effect. More than that, the  $\alpha$  dispersion, which depends on the static conductivity, might also be protonic in nature.

In the study of conduction in disordered systems and LFD in general, one of the very useful models is the so-called percolation model. In a percolation model, the conductivity arises from long-range percolation of the charges along pathways (which are at the protein surface level and involve the displacement of protons between ionizable sidegroups of the protein) that connect the localized clusters.

The fractal interpretation of the dielectric response, especially for tissues, initially pioneered by Hill [38] and Dissado [39] is now more and more gaining terrain. The principal idea brought into play by the fractal system proponents is that organization of the tissues is far from Schwan's mixture model - a suspension of spherical cells in an aqueous solution. In the real tissue, the cells are interconnected and connected to the extracellular matrix in an intricate network. The cells are not spherical and usually their shape fluctuates slowly. In this context, and emphasizing that is the structural organization of the cells within a tissue that makes possible the biological function at that level, one can imagine that a stochastic fractal structure can be a more realistic model. This structure is expected to be evidenced especially in the  $\alpha$  dispersion, where the current travels outside of the cells, 'exploring' the network of interconnections.

It was identified [39, 40] that for these systems, both  $\epsilon'$  and  $\epsilon''$  vary with a fractional power of the frequency (see Figure 20):  $\epsilon'(\omega) \propto \epsilon''(\omega) \propto \omega^{n-1}$ , and consequently, the impedance depends as  $Z(\omega) \propto (i\omega)^{-n}$ .

In an equivalent circuit, that will involve using a CPE (constant phase angle element), with the exponent  $n$  containing all the information about the structure. This type of response can be mistaken with the onset of the d.c. conduction ( $\omega \rightarrow 0$ ) for which  $\epsilon'(\omega) \propto \text{constant}$  and  $\epsilon'' \propto \sigma/\omega$ . With a similar low frequency behavior, the Maxwell-Wagner interfacial polarization can be distinguished by the dependency of  $\tan \delta$  of  $\omega$  or in terms of permittivity,  $\epsilon' \propto \omega^{-2}$  and  $\epsilon'' \propto \omega^{-1}$ .

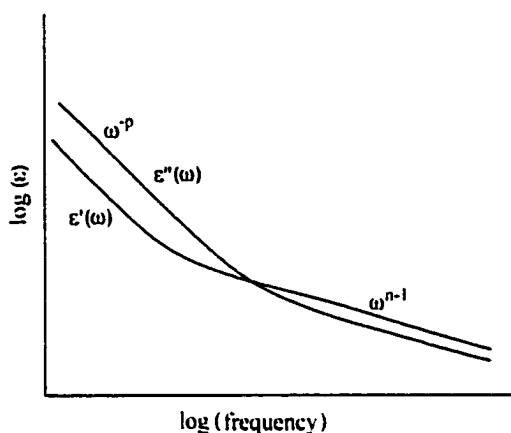


FIG. 20. Graphical representation of  $\epsilon'$  and  $\epsilon''$  dependence of frequency  $\omega$ , in LFD regime, based on power law behavior expected in fractal structures.

A large number of systems are known to exhibit this frequency dependence, among them being wetted proteins, hemoglobin, humid sand, porous ceramics and polymers.

Anyway, examining from this perspective our blood samples (see Fig. 21), it is quite clear that what we have observed in the low frequency end of the spectrum are ionic conductivity effects. Returning to fractal systems lets see what are their important features and how we can use them to better model the dielectric properties at low frequencies. Fractal geometry, in very broad terms, is a generalization of the Euclidian geometry, which adds the concept of non-integral dimension. Complexity and scaling are intimately related, so in an intuitive manner, the fractal dimension  $d$  is a quantifier of

complexity measuring the rate of addition of structural detail when the magnification is increased.

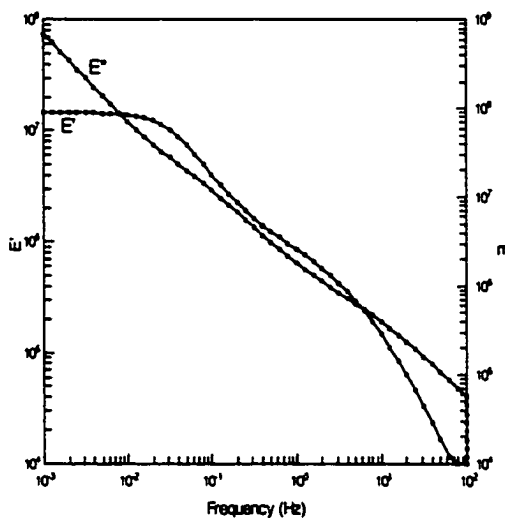


FIG. 21. Ionic conduction effect in blood samples at low frequency. Experimental points were collected only down to  $f = 0.05$  Hz and then extended to  $10^{-3}$  Hz by fitting with the model.

The idea of using fractals in these studies is twofold. On one hand, it refers to the electrode-electrolyte interface (the transport across such an interface and its frequency response) and on the other hand it refers to the material under investigation: the biological tissue. One of the well known methods of reducing the polarization at low frequencies is to use to so-called black platinum electrodes, which because of their porous structure of the superficial layer (deposited by electrolysis) have an increased effective area, a consequently reduced current density and polarization. During this study we used Pt, black Pt and some electrodes made of carbon (conductive) aerogel, material that offers a tremendous effective area per unit of mass. Whether designed as fractal or not, it is believed that electrodes in general can be treated as such (see the Constant Phase

Angle Conjecture). A unitary view of a fractal interpretation of our results is given in the last chapter.

### **Cells. An electrochemical prospective**

Biological tissues, with the fields of  $10^6$ - $10^7$  V/m across cell membranes, networked through gap and tight junctions and connected to the extracellular matrix, are probably obvious examples of complex and active systems in which linearity represents only an approximation. A very interesting approach to linearity at macroscopic scale vs. non-linearity and asymmetry at the level of microscopic constituents in biological tissue, is presented in [41]. The idea is that the effect of the local non-linearity is 'smeared-out' by the randomness of the interconnections of the constituents in the network, making possible the characterization of the macroscopic system by means of an effective conductivity and permittivity. In the next few paragraphs we will try to describe the system that we worked with, emphasizing the aspects which are most relevant to the dielectric measurements.

From an electrochemical point of view, biological systems are highly branched circuits consisting of ionic conductors, aqueous electrolyte solutions and selective membranes. Aqueous electrolyte solutions are of exceptional importance to the biological and physiological processes in living matter, because they form the intra- and extracellular fluids. There is experimental evidence [32, 42] that electronic conduction is also present in these systems, from electrons being transported over macroscopic distances due to peculiar relay-type mechanisms.

The conductivity of water (in theory  $\sigma = 3.8 \cdot 10^{-6}$  S/m at  $T = 20^\circ\text{C}$ ) depends on its degree of purification. The water molecule has 2 OH bonds at about  $105^\circ$ , has an approximate radius of 0.14 nm and it is dipolar, with a dipole moment of 1.87 D. The relative permittivity at  $25^\circ\text{C}$  and low frequencies is 78.5. Its structure is not completely known, one of the most common theories being the "flickering clusters", a continuous rearrangement and decay of a loosely packed lattice.

Essential process in tissues -metabolism and synthesis, reproduction of genetic material, etc. - occur at the level of basic structures or units: the cells. In their vital

functions, the cells are in continuous interaction among themselves and with the extracellular space, their membranes (both plasma and intracellular ones) being essentially the regulators of these interactions. The membrane consists of two layers (a bilayer) of oriented lipid molecules, with the hydrophilic heads outside and the hydrocarbon tails toward each other, as seen in Figure 22, with a mean distance between lipids of about 5 nm and a total thickness of 8-15 nm.

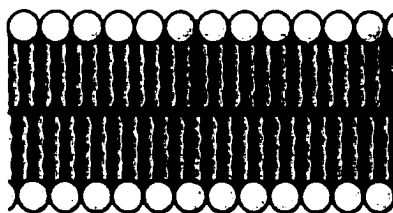


FIG. 22. Lipid bilayer in a plasma membrane.

In fact the membrane is a very important and complex organelle. Embedded in the lipid bilayer are (not shown) cholesterol and lipid components, membrane and transmembrane proteins with specialized functions (*e.g.* ion channels, ion pumps). A more realistic picture of the membrane, in the so-called fluid membrane model is shown in Fig. 23:

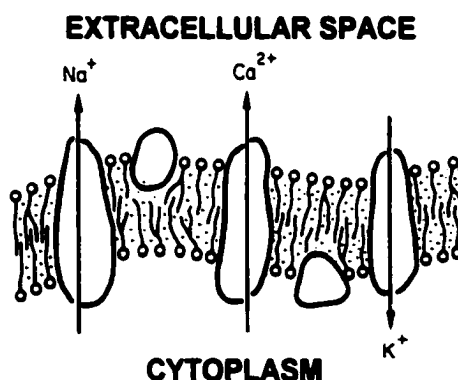


FIG. 23. The membrane model. Proteins are incorporated in a semifluid liquid bilayer. The direction of the ionic pumps ( $\text{Na}^+$ ,  $\text{K}^+$ , and  $\text{Ca}^{2+}$ ) is also shown (adapted from [43]).



The plasma membrane separates the cytoplasm from the extracellular solution. The concentration of the important ions is synthesized in Table II and in a graphical form in Fig. 24:

TABLE II. Example of ions concentration (in mM) in frog muscle.

	Na <sup>+</sup>	K <sup>+</sup>	Cl <sup>-</sup>	Others
Outside the cell	120	2.5	120	K <sup>+</sup> , Ca <sup>2+</sup> , Mg <sup>2+</sup>
Inside the cell	9.2	140	3.5	Organic anions

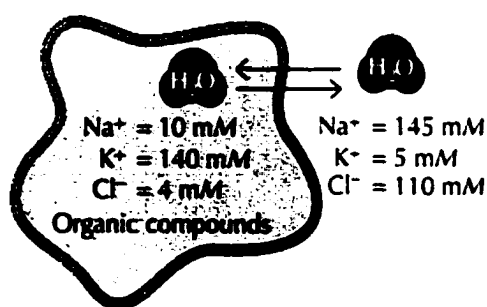


FIG. 24. Ions concentration in and outside cell membrane

All biological systems contain aqueous electrolyte solutions, which consist of either strong or weak electrolytes (organic substances with acidic or basic functional groups exhibiting low dissociation rates). Their pH ranges from 6.7 to 7.6 and their appearance is often gel-like. In spite of their different permeabilities - the permeability of the membrane for Na<sup>+</sup> is about 75 times lower than for the K<sup>+</sup> ions - the total flux, in opposite directions, of the two species is approximately the same. Actually, the permeability is potential dependent and this represents the basis for the membrane excitation.

Across the membrane a potential difference  $\phi_m$  is established, always negative, since the cytoplasm is negatively charged relative to the extracellular solution and by convention  $\phi_m = \phi^{\text{int}} - \phi^{\text{ext}}$ . Typical values are between -50 mV and -100 mV, which for an approximate membrane thickness of 15 nm, means an electric field across the membrane of the order of  $10^6$ - $10^7$  V/m. This potential gradient is meant to compensate the concentration gradient and thus preserve the ion concentrations. The specific electrical resistivity of the membrane is very high ( $\sim 10^6 \Omega\text{m}$ ) compared with that of the extracellular fluid ( $\sim 1 \Omega\text{m}$ ). Its specific capacitance is  $\sim 10^{-2} \text{ F/m}^2$ .

We reviewed in this chapter the main polarization mechanisms with emphasis to extensions of the Debye and interfacial polarization, which can constitute more or less ideal models for the biological tissue. Emphasis on the mechanisms contributing to the  $\alpha$  and low  $\beta$  dispersions, especially counterion and interfacial polarization, will be placed in the analysis chapter.

## CHAPTER IV

### ELECTRICAL IMPEDANCE SPECTROSCOPY

This chapter will be devoted to a description of the principles of electrical impedance spectroscopy and of specific variables accessed by the impedance experiment.

Spectroscopic techniques can be very broadly (and likely not accurately) divided into those which examine the molecular structure (*e.g.* FT-IR, NMR) and those which examine the physical arrangements and behavior of molecules *within structures*. Dielectric spectroscopy<sup>14</sup> tends towards the latter category, although information on molecular structure can be gained. At low frequencies, the applied field will result in changes of the mean position of the dipoles as the direction of the field changes, although these dipoles will still be oscillating around that mean. At high frequencies, the changes in field direction are so rapid that the dipoles are unable to reorient because of their inertia and viscous damping, so the total polarization of the system falls. However, at a characteristic frequency,  $\omega_p$ , the efficiency of the reorientation process is at a maximum, as the rate of change of the field matches the relaxation time of the dipoles.

EIS involves the study of the response of a system to an applied electric field. The dispersion is the frequency dependence of the polarisation response. As the frequency of the field changes, different mechanisms of polarization will predominate. Two processes are associated with frequency dependence: resonance and relaxation processes. The regular oscillations (*e.g.* vibrations of intramolecular bonds) absorb energy over a narrow range of applied frequencies, but these frequencies tend to be higher than those of interest for EIS. The relaxation processes, on another hand, are essentially cooperative phenomena, involving the damping of the response of dipoles to an electric field, this damping being due to the inertia of the dipoles and the structure of the surrounding environment. Hence, dielectric studies may yield information concerning both the nature of the relaxing species and the structure surrounding that dipole. Dielectric phenomena

---

<sup>14</sup> Dielectric analysis can use either temperature  $T$  or frequency of the applied field  $\nu$ , as parameters. With this in mind, the rigorously correct name for the type of analysis we used, is impedance spectroscopy.

may be studied over a frequency range of  $10^{-5}$  Hz to  $10^{12}$  Hz, a much wider spectral window than most other spectroscopic techniques.

In general, the type of information that we are seeking is:

- Electrical properties of materials (systems) and their interfaces with electronically conducting electrodes.
- The dynamics of bound or mobile charges in the bulk or interfacial regions of any kind of material: ionic, semiconducting, mixed electronic-ionic or dielectric<sup>15</sup>. For the study of the biologically relevant materials, the aqueous electrolytes and polyelectrolytes are the basic models.

Most of the time, the impedance investigation of a system implies the existence of electrodes at the boundary of the system. The electrodes are used for applying an electric field and for measuring the potential and current generated as response to a certain excitation. Complex phenomena occur at the interface between electrode and system, depending strongly on their state and phase. For sustaining a steady current, one needs a steady sink for the arriving particles and a steady source for those departing. The most common electric charge carriers are the electrons and ions, the reactions taking place at the electrode acting as both source and sink for the corresponding particle.

### **Variables Accessible by Impedance Measurements**

The electric response,  $i(t)$ , of a system (electrodes & material), is expected to be linear if the magnitude of the applied voltage  $|v(t)|$  is smaller than the thermal voltage:  $V_T = kT/e \approx 25mV$ .

The most common approach is the excitation of the system directly in the frequency domain. A monochromatic electric field of frequency  $\omega$  is applied on the interface and the resulting steady state current is measured:

---

<sup>15</sup> A dielectric may be defined as a material that contains dipoles, either permanent or induced. Polarization arises from a finite displacement of charges in an electric field and is distinct from conduction which arises from a finite average velocity of charges in an electric field.

$$\begin{aligned}v(t) &= V_o \sin(\omega t), \\i(t) &= I_o \sin(\omega t + \phi).\end{aligned}\tag{58}$$

The impedance  $Z(\omega)$  is defined as the ratio of the measured  $v$  and  $i$ :

$$Z(\omega) \equiv v(t)/i(t),\tag{59}$$

with the modulus

$$|Z(\omega)| = V_o(\omega)/I_o(\omega).\tag{60}$$

The impedance can be expressed in the complex plane as:

$$Z = Z' + i \cdot Z'' ; \quad (i = \sqrt{-1}).\tag{61}$$

The complex plane  $ZZ''$  is usually called the Argand diagram. The frequency dependence of the real and imaginary part of the impedance,  $Z' = f(\omega)$  and  $Z'' = f(\omega)$  is represented in the so-called Bode diagrams. A number of other parameters are routinely employed in the representation and analysis of impedance data and these are:

- Admittance  $Y$ , the inverse of impedance  $Z$ :

$$Y(\omega) \equiv Z^{-1}(\omega) = Y' + i \cdot Y''\tag{62}$$

- Modulus function  $M$ :

$$M(\omega) = i\omega C_o Z(\omega)\tag{63}$$

in which  $C_o$  represents the capacitance of the empty electrolytic cell, usually considered a parallel plane capacitor,  $C_o = \epsilon_o A/d$ .

- Dielectric permittivity  $\epsilon$ :

$$\epsilon = M^{-1}(\omega) = Y/i\omega C_o = \epsilon' - i\epsilon''\tag{64}$$

These relations also show the actual process for obtaining  $\epsilon$  from impedance, the primary results of a measurement. Permittivity  $\epsilon(\omega)$  is preferred to  $Z$ , as output parameter of the measurement and analysis, in particular for dielectric materials with very low conductivities. This is not the case for biological samples and liquid electrolytes, where all dissociated charges are mobile, with mobilities that can differ considerably.

In the absence of an exact physicochemical model, the collected data are analyzed by a lumped circuit of the measured impedance  $Z$ . Unfortunately, the models are not proven to be unique, so other constraints have to be used. In general the disadvantages of impedance spectroscopy are related to the ambiguities in finding and interpreting a model for a given physical system. The objective is to find a reasonable equivalent circuit whose impedance matches the measured impedance over the observed frequency interval. Elements of the equivalent circuits are usually resistors, capacitors and various distributed elements. The term distribution can either be used in the sense of a finite space extent of the system itself or in the sense of a distribution of the associated microscopic properties (conductivity, space charge polarization, etc.). The CPE (Constant Phase angle Elements), often used with great success in fitting the experimental data, can arise, for example, from processes associated with either the bulk or the interface (*e.g.* a time constant describing such a process can in fact be a distribution of such time constants, each characterized by a certain activation energy). In such a case, the RC time constant of a series of parallel circuit is replaced by a more complicated frequency response of a distributed impedance element.

### **The Frequency Response Analysis**

The Frequency Response Analysis is based on the assumption that the system under investigation is linear. Few systems are, in reality, linear. We have described, in Chapter III, the particularities of the biological systems, electrolytes, cells and tissue and we emphasized that fact that for such complex and dynamic systems linearity is just an approximation.

The simplest way to think about the frequency response of a linear system is depicted in Fig. 25:

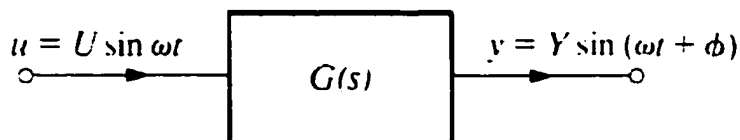


FIG. 25. Excitation of a linear system with a monochromatic signal  $u(t)$ .  $G(s)$  is the transfer function characterizing the system,  $Y(s)=G(s)U(s)$ , with  $s=i\omega$  the Laplace corresponding variable of  $t$ .

In a steady-state regime, the response of the system is  $y(t)$  having the same frequency as the excitation, but different amplitude and phase. In an ideal setting, for a linear system without noise, the relative phase and magnitude of the response would be directly measurable with an oscilloscope, as shown in Fig. 26:

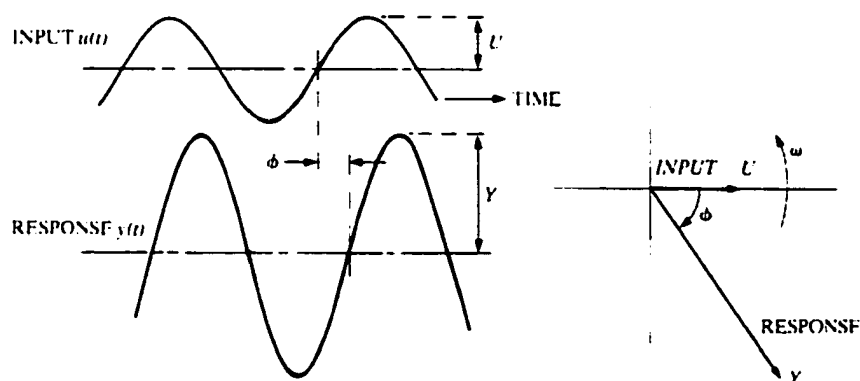


FIG. 26. The steady-state response  $y(t)$ , of a linear system to an input  $u(t)$ .

Making such measurements for a whole range of frequencies, one should be able to numerically determine the impedance function. The advantage of such measurement resides in the frequency selective nature of the analysis, achieved by extracting from the system's response one component, that of the excitation. Real systems, as already

mentioned, are noisy and distorted (as seen in Fig. 27), and that makes impractical an accurate measurement of the gain and phase.

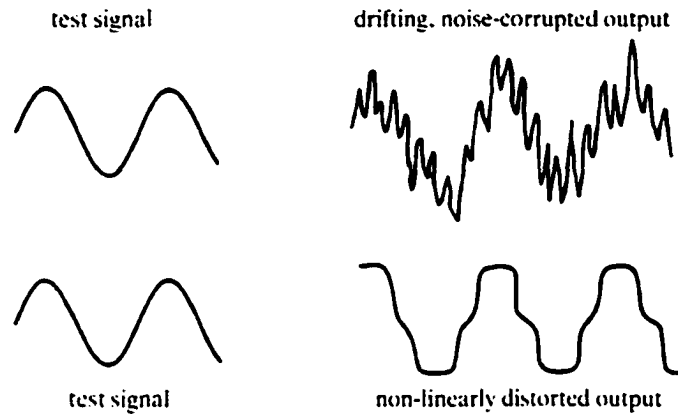


FIG. 27. The response of a real system, either corrupted by noise or with distortions due to non-linearity

In such cases, the solution is the correlation frequency analysis. The output  $y(t)$  is multiplied with  $\sin \omega t$  and  $\cos \omega t$  and then integrated. A schematic of this method is shown in Fig. 28:

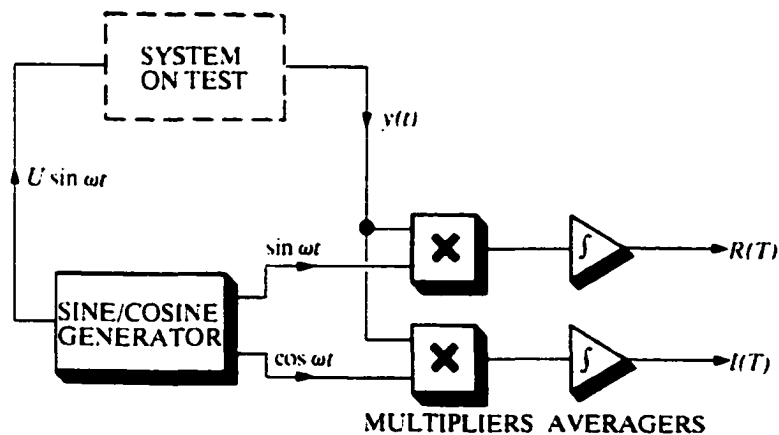


FIG. 28. A basic design of a correlation Frequency Response Analyzer (adapted from Solartron ref [44])



Why this system is more powerful in terms of dealing with noise and distortions, should become transparent from the following:

Let

$$\begin{aligned} u(t) &= U \sin \omega t, \\ y(t) &= Y \sin(\omega t + \phi), \\ \text{with} \\ Y &= U |G(i\omega)| \quad \text{and} \quad \phi = \angle G(i\omega). \end{aligned} \tag{65}$$

The output of the sine channel will be given by:

$$\begin{aligned} R(T) &= U |G(i\omega)| \frac{1}{T} \int_0^T \sin \omega t \cdot \sin(\omega t + \phi) dt = \\ &= \frac{U}{T} |G(i\omega)| \left[ \cos \phi \left( \frac{T}{2} - \frac{\sin(2\omega t)}{4\omega} \right) - \sin \phi \left( \frac{\cos(2\omega t)}{4\omega} - \frac{1}{4\omega} \right) \right] \end{aligned} \tag{66}$$

If the integration time  $T$  is chosen to be an integer number of half periods of the harmonic investigated:

$$T = \frac{N\pi}{\omega}, \quad \text{with } N \in \mathbb{Z} \tag{67}$$

then the output  $R(T)$  will be:

$$R\left(\frac{N\pi}{\omega}\right) = \frac{U}{2} |G(i\omega)| \cos \phi \tag{68}$$

In a similar manner, it can be shown that the other output will be:

$$I\left(\frac{N\pi}{\omega}\right) = \frac{U}{2} |G(i\omega)| \sin \phi \tag{69}$$

From (68) and (69) one can find both the magnitude and phase of the response function. In practice, the integration is performed over a period of time equal with an integer number of periods of the sinewave, in order to avoid non-linear harmonic distortions. By increasing  $T$ , one can reduce the noise influence in the measurement process to very low levels. This is one of the reasons for which most impedance spectra presented in this

work are very smooth and virtually noiseless. The software for acquisition allows the user to either set  $N$ -the number of complete cycles used for averaging (see eq. (67)) or to preset a target value for the standard deviation such that the signal is integrated until the SD reaches that level.

## CHAPTER V

### EXPERIMENTAL METHODS

In this chapter we will describe the equipment and the method used for the detection of impedance changes in irradiated tissues. These changes were correlated and modeled with alterations in the electrical conduction and polarization and these, in turn, used as criteria for distinguishing between oncotic and apoptotic death, and for assessment of membrane and cell volume, radiation induced modifications.

The biological samples used throughout the experiments were human blood and rat kidney, lung, liver and heart tissue. In addition to the biological tissue, experiments were performed on irradiated discrete RC components, electrolytes and sand. The results on the non-biological systems were not of interest by themselves. They used for either calibration of the impedance analyzer, detection of possible radiation effects on the connecting probes, or the existence and determination of electrode polarization. Sand of various grain sizes and humidity was investigated to gain prior knowledge on Maxwell-Wagner interfacial polarization on a disordered system often modeled as a stochastic fractal.

The tissue types were chosen for a number of reasons. Our initial research focused on blood, in our opinion, a system that can be more easily modeled and understood. The preliminary measurements on blood were part of a NIH proposal in 1998. The reviewers, passed along with the enthusiasm for a method that showed the potential of becoming a new way of monitoring radiation effects, their criticism towards a number of issues. One of them was the relevance of results obtained in blood versus tissues, thus suggesting a more earlier transition to biological tissue than we would have otherwise considered. Others issues discussed become, in the second phase of our research, the rationale for a redesign of the measurement cell, a more careful consideration of the temperature effects, the exclusive use of the four-electrode method and the search for new electrode materials.

The tissues we used were provided by Dr. Anca Dobrian from Eastern Virginia Medical School (EVMS) and were excised from healthy mice and rat animals, which were sacrificed for purposes related to concurrent experiments running at EVMS. After

sacrifice, the tissues (integral organs) were stored in Krebbs buffer, whose composition is given in Table III, at 4-5 °C (on dry ice). Studies of the impedance changes occurring after excision were done for each of the tissues, in order to have a baseline for the measurements during and after irradiation, and the results are reported for each tissue in the Data Analysis Chapter.

TABLE III. Krebbs-bicarbonate free buffer composition.

Substance	Concentration	
NaCl	0.1M	5.8 g/l
KCl	4.69 mM	0.35 g/l
CaCl <sub>2</sub>	1.87 mM	0.27 g/l
MgSO <sub>4</sub>	1.20 mM	0.29 g/l
KH <sub>2</sub> PO <sub>4</sub>	1.03 mM	0.14 g/l
HEPES	20mM	4.76 g/l
Glucose	11.1 mM	1.99 g/l
	pH = 7.4	

The irradiation of the excised tissue was carried out at Virginia Beach General Hospital (VBGH) under the direction of Dr. Raymond Wu, using a linear accelerator Clinac 1800, in a clinical setting. The precise timing of the irradiation with reference to the excision time was recorded for each sample. The specific dose received for each sample is discussed in the Data Analysis Chapter. We would like to emphasize though, that at this stage of the exploratory research, we were not particularly interested in dose or energy dependence of impedance changes. Sometimes two or three fractions were delivered during an irradiation session, but again we were only interested in the dynamic of the impedance parameters during the whole session. Long term monitoring of the tissues was not possible due to the lack of perfusion, but we do hope that, fortunately, with adequate funding, we will be able to carry out *in vivo* experiments, in which we will establish and validate the relation between the impedance changes, the type and extent of the cell death in the tissue and changes in morphology.

### Impedance Spectroscopy Equipment

The equipment used for the measurement of dielectric properties in tissue was a Frequency Response Analyzer (FRA), Solartron 1260 and a Dielectric Interface, Solartron 1294, provided with generosity by Solartron, Inc. Some preliminary experiments on blood also used the Dielectric Interface 1296. Here follows a brief description of the main features of each of these components of the measurement system.

The 1260 Impedance/Gain-phase Analyzer is probably the most powerful, accurate and flexible frequency response analyzer available today. It can measure impedances up to 100 M $\Omega$ , in two-, three- and four-terminal measurement configurations. The frequency ranges from 10  $\mu$ Hz to 32 MHz with a resolution of 1 in 65 million (0.015 ppm). The modulus and phase of impedance can be measured with an accuracy of 0.1% and respectively 0.1 $^\circ$  and a resolution of 0.001 dB, 0.01 $^\circ$ . It can use polarization voltage up to  $\pm$ 40.95 V and automatically sweeps frequency, amplitude or bias. Even though it can operate in a stand-alone mode, in our studies it was computer-controlled through a GPIB interface (IEEE 488).

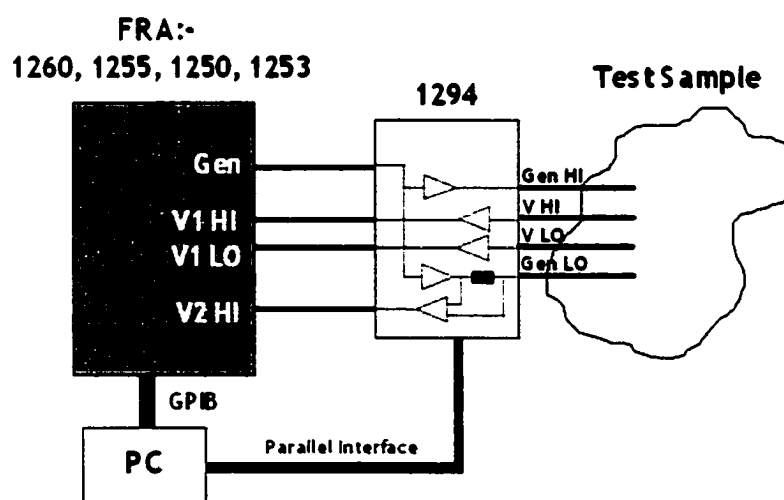


FIG. 29. Typical setting for bio-impedance measurements. A Frequency Response Analyzer (FRA) is connected to a Dielectric Interface, which uses a 4-electrode configuration to connect to the sample (adapted from Solartron documentation).

The Dielectric Interface Solartron 1294 is a highly accurate and sensitive impedance interface which is designed to operate together with an FRA for 2- or 4- terminal impedance analysis. The 1294 also complies with safety specifications for the connection of electrical equipment to live subjects (*e.g.* IEC601), thus making it suitable for bio-impedance measurements. A schematic of the interconnection of the two devices is shown in Fig. 29:

Four terminal analysis allows the separation of the current stimulus Gen HI, LOW and voltage sense electrodes (V HI and V LOW) which is important in applications where the impedance of the connection cables and electrodes is significant compared to the impedance of the sample itself (which is the case for conductive - either ionic, electronic or mixed - systems). High accuracy 4-terminal measurements are very difficult to achieve in practice. The effects of unequal electrode impedances (often seen in bioimpedance measurements for example), and instrumentation effects to do with input and cable capacitance have, until now, limited the performance of 4-terminal impedance measurement equipment.

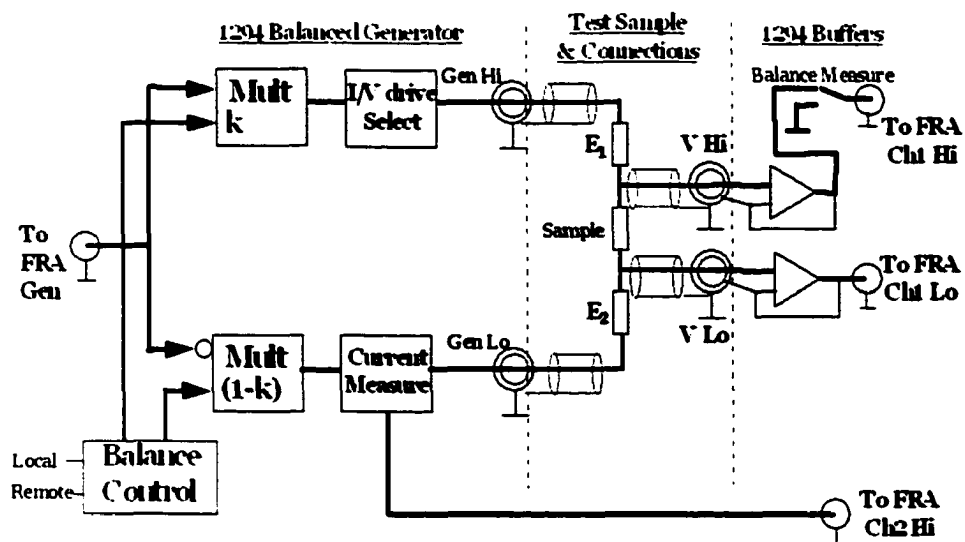
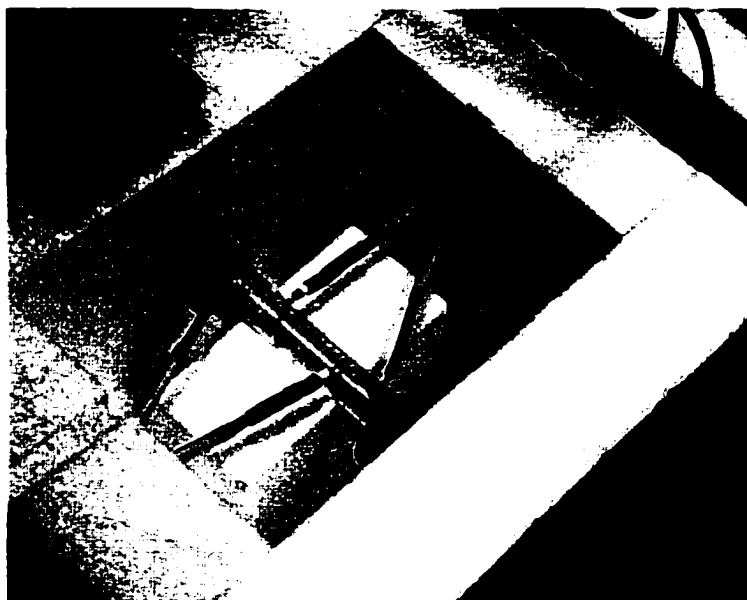


FIG. 30. Special feature of the Dielectric Interface 1294, which makes possible reliable 4-terminal measurements

The Solartron 1294 makes use of various measurement techniques including balanced generator, high impedance voltage sense inputs and driven shield cables, in order to achieve maximum accuracy 4-terminal measurements. The balanced generator can also cope with extremely difficult measurement situations where for instance the electrode impedances are not equal, a typical situation for bio-impedance measurements where it is difficult to obtain reproducible electrode contacts onto sample. At high frequency, a specific problem is due to errors introduced by input and cable capacitance. The driven shield technique replicates the signal waveform (which appears on the inner cable), onto the cable shield in order to minimize leakage current flow between the cable inner and the shield. Since no current flows between the cable inner and shield, the impedance appears to be very large and therefore the effects of the cable and input capacitance are minimized. A schematic representation of some of these elements is shown in Fig. 30.



**FIG. 31. Electrolytical cell in the Dewar-like casing. Four of the sample holders (of different diameters) are also shown on top.**

The 1296 Dielectric Interface is similar in function with 1294 but distinguishes itself by an exceptionally accurate current to voltage converter (1 fA resolution), which enables the measurement of the ultra-low capacitance and current levels, commonly experienced in material/dielectric analysis. An important concern in the design of the experiments was the temperature effect. The temperature coefficient of the conductivity of most biological materials is  $\approx 2\%$  per  $^{\circ}\text{C}$  at low frequencies. To make sure that the measured changes in impedance are only irradiation induced, we built a Dewar-like case, shown in Fig. 31, surrounding the measurement cell. The design of the cell itself was inspired from a previous design proposed of Schwan [45], pictured in Fig. 32.

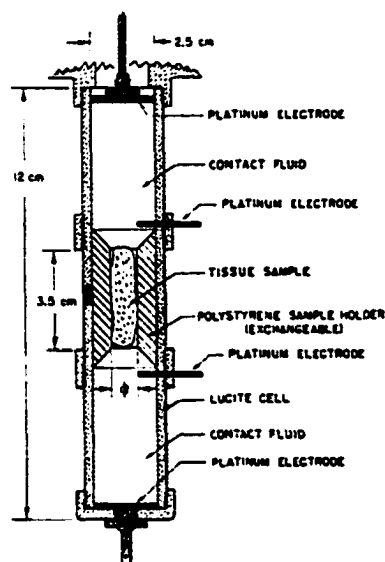


FIG. 32. Electrolytic cell for the determination of tissue impedance (adapted from [45]).

The temperature was actively controlled with a pearl thermistor placed on the electrolytic cell. An error signal provided by an electronic temperature regulator drove a thermoelectric element (1.5 x 1.5 cm) situated under the cell. The 3 cm walls and the large heat capacity obtained by filling the vessel with water filled polyethylene sachets, allowed us to control the temperature to better than  $0.02\text{ }^{\circ}\text{C}$  per 30 min, the approximate duration of the measurements (controls and irradiation) per sample. Also, to limit the



temperature rise of the sample due to ohmic effects, a maximum current of 100  $\mu\text{A}$  was chose. The applied potential, when the potentiostatic mode was used, was limited to 50 mV, because of the non-linearity of membrane impedance. To stabilize the temperature more easily, on one hand, and to slow down the denaturation processes on the other hand, all measurements on tissues were performed at temperatures close to the room temperature, in the range 23-25° C.

The dielectric changes reported here were measured in freshly excised tissue that was far from a physiologically normal state. An obvious question arises: are these properties likely to be representative for tissue *in situ*? Of course, following this line, one can ask if these *in situ* properties, reflect, or can be directly related to physiological measurements *in vivo*. One of the reasons for choosing kidney tissue for observing radiation induced changes in impedance, was the fact that without elaborate preservation techniques, the kidney can be conserved up to 24 h with little or no deterioration. In general, our measurements were done on tissue freshly excised, and/or kept at 4 °C in a refrigerator for 2-10 h.

### **Electrodes and Specific problems**

The electrical impedance measurements on biological materials pose a number of difficulties. Electrodes are used to inject current and acquire the induced potential across the sample or parts of it. Complex electrochemical reactions occur at the electrode-electrolyte interface and create polarization phenomena. In certain conditions, this can create important errors in measurement. We will discuss some particularities, problems and solutions for the contact electrodes used in the frequency range (mHz-MHz) of our measurements.

The usual choice for an electrode is a metal, but can be in principle any conducting material which will work being immersed in an electrolyte. The problematic phenomenon to deal with is electrode polarization. Due to the free energy differences between electrode and solution, at the interface, two current mechanisms will occur: a Faradaic current resulting from charge transfer across the interface (neutralization of electrons leaving the electrode with the positive charge molecules in the bulk solution)

and a non-Faradaic (or capacitive) one. The conduction through the electrolyte can be, for a large frequency range, considered purely resistive. As we already discussed, there are a number of models for the double layer formed at the interface electrode-electrolyte. The closest, the so-called Helmholtz layer, consists of aligned ions and water dipoles that balance out the charges on the aqueous surface of the electrode. The next one, the Gouy-Chapman diffuse layer, is formed by ions in solutions, in thermal motion, that compensate the electrode charge. For the usual buffers (physiological serum, Ringer solution, Krebs buffer, etc.) the ionic strength is large enough so that the diffuse layer can be considered negligible in comparison with the Helmholtz layer. The currents across the double layer are displacement currents and do not require electron transfer. The capacitive mechanism can be therefore modeled as a capacitor  $C_p$ .

Returning our attention to the Faradaic current, we have to stress the idea that electron transfer between electrode and solution means a chemical reaction (reduction or oxidation). Thus the Faradaic process can be modeled in an equivalent circuit by a resistor, whose magnitude is proportional with the activation energy of the reaction occurring at the electrode. For a heterogeneous electrolyte the potential of the electrode will determine which of the ionic species will undergo a Faradaic process. Sometime in series with the usual Faradaic resistor there is another impedance caused by a concentration gradient starting at the electrode and extending into the bulk - the Warburg Diffusion impedance. Warburg initially postulated that the resistance and capacitance of an electrode-electrolyte interface varies proportional with  $\omega^{-1/2}$ . Later, Fricke showed in a more elaborate model, that the polarization resistance  $R_p$  varies as  $\omega^{-1+m}$  and  $C_p$  as  $\omega^{-m}$  with  $m \in [0.1, ..0.7]$ . According to Jossinet and McAdams [46] an even better way of modeling is by using a CPA (Constant Phase Angle) element of impedance  $Z = A(i\omega)^{-\beta}$ . In the linear model approximation (small signal  $k_b T \ll \hbar \omega$ ) the values of  $C_p$  and  $R_p$  are independent of the current density, but in general this is not true. Simpson *et al.* [47] determined experimentally for Pt electrodes, the non-linearity limit to  $\sim 1 \text{ mA/cm}^2$  at 10 Hz and  $10 \text{ mA/cm}^2$  at 1 kHz. In our experiment, the excitation signals were much smaller than the non-linear regime, being of the order  $10\text{-}100 \text{ }\mu\text{A/cm}^2$ .

With respect to charge transfer there are reversible (or non-polarizable) and irreversible (polarizable) electrodes. In the first case, the electrode is at equilibrium with the ions in solution (*e.g.* Ag/AgCl). The polarizable electrode (*e.g.* the Pt electrode) is irreversible because there are no ions in solution in equilibrium with the electrode. Large activation energy leads to a large value for  $R_p$ , but increasing the surface area of the electrode can decrease it.

In the course of our experiments, we have tried a new material for electrodes - *carbon aerogel* - characterized by a very large effective area due to its porosity. Even though we obtained a very low current density and consequently a low polarization resistance there were some other phenomena for which reason we didn't continue using it. Shifts in pH near the electrode, were reported in literature [48] for the carbon electrodes. Adsorption, the binding of an ion from the bulk of the electrolyte to the electrode was increased as results of the unusually large active area. The Ag/AgCl electrodes, the most commonly used reversible electrodes (in EEG, EKG, etc.) cannot be used in buffers since the silver ions are toxic. The Platinum electrodes, especially when treated (electrolytically coated) with black platinum in order to reduce the polarization impedance, are the electrodes of choice and this is what we used in our experiments.

One of the methods for reducing (theoretically at least) the polarization of electrodes is the use of the four-terminal method<sup>16</sup>. The excitation current is applied using 2 electrodes and the potential measured across the sample, is measured with another pair. For a frequency sweep, the current have to be kept constant. The idea is simple, no current flowing between the 2 voltage electrodes, no electrode polarization.

When the polarization cannot be eliminated through experimental means, one should proceed to correct the data for polarization of the electrodes. That means modeling the equivalent circuit such that it will include equivalent elements describing the interface phenomena (double layer formation, diffusion, fractal structure of the electrode, etc.) This is especially a requirement for conductive liquids where the surface ionization and ion exchange processes in the double layer depend critically of the chemical nature of the investigated sample as well as the chemical and physical nature of the electrodes.

---

<sup>16</sup> For two-electrode measurements the electrode separation is another method, together with high-surface electrodes and low current density.

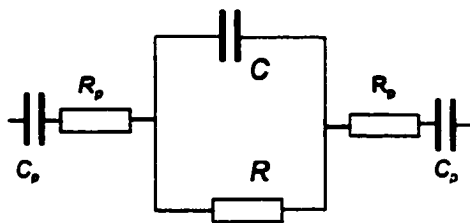


FIG. 33. Equivalent circuit for a conductive dielectric sample with electrode polarization

An interesting correction is described by Raicu [49] under the assumption that the system, sample and electrodes interfaces can be modeled as simple series and parallel RC circuits, as shown in Figure 33. The total impedance of such a system is given by:

$$Z(\omega) = R_p + \frac{R_s}{1 + (\omega R_s C_s)^2} - i \left[ \frac{1}{\omega C_p} - \frac{\omega R_s^2 C_s}{1 + (\omega R_s C_s)^2} \right] \quad (70)$$

Considering, as previously explained, the elements describing the polarization as proportional with powers of  $\omega$ :

$$\begin{aligned} R_p &= a\omega^{-m} \\ C_p &= b\omega^{-n} \end{aligned} \quad (71)$$

with  $a, b, m, n \in \mathbb{R}^+$ . Taking derivatives of  $Re(Z)$  and  $Im(Z)$  with respect to  $\omega$  and under the low frequency approximation ( $\omega \rightarrow 0$ ) we obtain:

$$\begin{aligned} \frac{d}{d\omega} Re[Z(\omega)] &= -a m \omega^{-1-m} \\ \frac{d}{d\omega} Im[Z(\omega)] &= \frac{2-n}{b} \omega^{n-3} \end{aligned} \quad (72)$$

By plotting these expressions in the logarithmic scale, we can determine the constants and then subtract the electrode contribution (point by point) from the general response

$Z(\omega)$ . However, given the power of the software that we've used, that allows us to fit simultaneously the  $\text{Re}(Z)$  and  $\text{Im}(Z)$  with the response of the equivalent circuit from Figure 33, the correction procedure can be done implicit, in the modeling of the equivalent circuit.

### Sample irradiation

The irradiation of tissue samples was carried out at Virginia Beach General Hospital (VBGH), in the Radiotherapy Department. The radiation generator was a Varian Clinac 20 Radiotherapy Linear Accelerator in a typical treatment facility. The electrolytic cell was placed on the treatment couch and all irradiations were carried out at 100 cm SSD (Source to Surface Distance). A schematic of the treatment head, for photon (A) and electron (B) beam is presented in Figure 34.

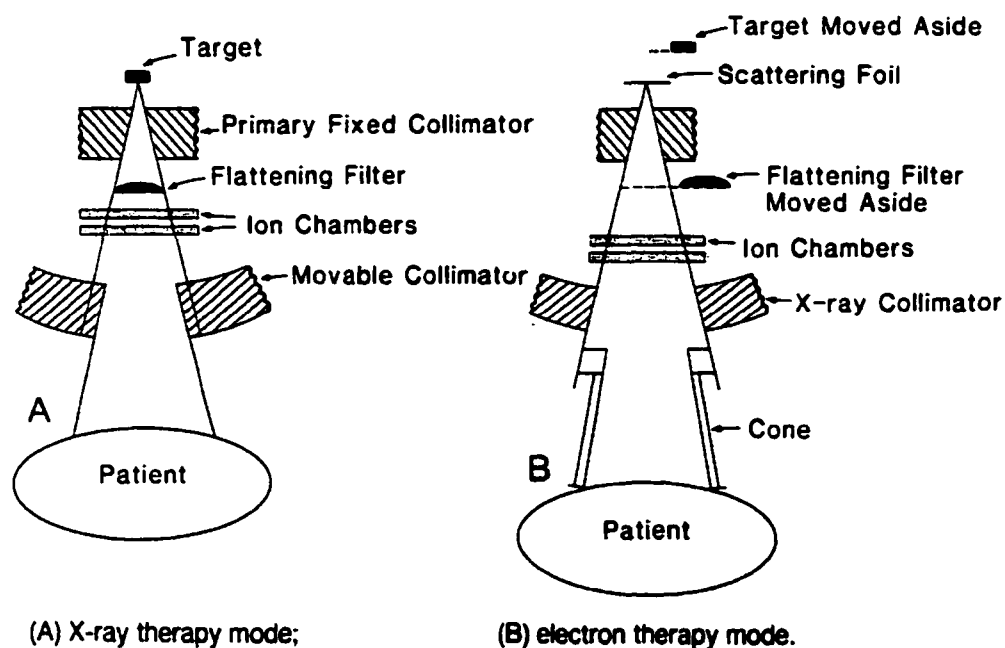


FIG. 34. The treatment head components of a linear accelerator for: A-photon beam and B-electron beam.(adapted from [50])

In brief, the linear accelerator accelerates electrons using a traveling or a stationary microwave field at approximately 3 GHz. The Clinac 1800 from Varian uses a stationary wave structure, with the microwave power coupled into the structure via side coupling cavities (rather than the aperture of the beam). The electron beam emerging from the accelerator structure is a pencil beam approximately 3 mm in diameter. The electron beam is bent at 270° by a precision beam transport system (achromatic electromagnet, focusing coils, etc.) The photon beam is the result of electrons striking a target of high Z material (tungsten) and producing bremsstrahlung radiation. The target is cooled with water and is thick enough to absorb most of the incident electrons. The efficiency of the X-ray production is proportional to Z the atomic number of the target and the tube voltage in volts.

In the electron beam mode, instead of striking a target, the electrons strike a scattering foil (a thin metallic foil, usually made of lead or aluminum). The purpose is to create uniform electron fluence across the treatment field, since at high energies the x-ray intensity is peaked in the forward direction. A small fraction of the electrons are converted into bremsstrahlung, thus 'contaminating' the electron beam. While the photon beam is collimated by a set of jaws (see FIG. 34) for the electrons these jaws are kept wide open and the collimation is realized with a set of attachable cones, extended down to the skin surface to avoid the wide scattering of electrons from the collimator surfaces and air.

A more detailed schematic of the main components of this particular type of Linac is shown in Figure 35. The linear accelerator generates electron and photon beams with energy ranging from 6 to 20 MeV. The central axis intensity at 10 cm depth for a (10 x 10) cm<sup>2</sup> field and a TSD (Target to Surface Distance) of 100 cm is  $77 \pm 2$  % of the intensity at maximum buildup. The depth of maximum buildup is  $3.0 \pm 0.2$  cm for the (10 x 10) cm<sup>2</sup> field. The dose rate at maximum buildup for the nominal (10 x 10) cm<sup>2</sup> field is variable in five steps from 100 to 500 rads/min at 100 cm TSD. By adjusting the movable collimator (see Figure 1A) the field size can be continuously varied from (0 x 0) (completely closed) to (35 x 35) cm<sup>2</sup>. The energy of the electron beam at isocenter<sup>17</sup> can

---

<sup>17</sup> The isocenter is the point of intersection of the collimator axis with the axis of rotation of the gantry.

be varied discretely from 6 to 20 MeV in 5 nominal steps (6, 9, 12, 16 and 20). The field size can be varied from (4 x 4) to (25 x 25).

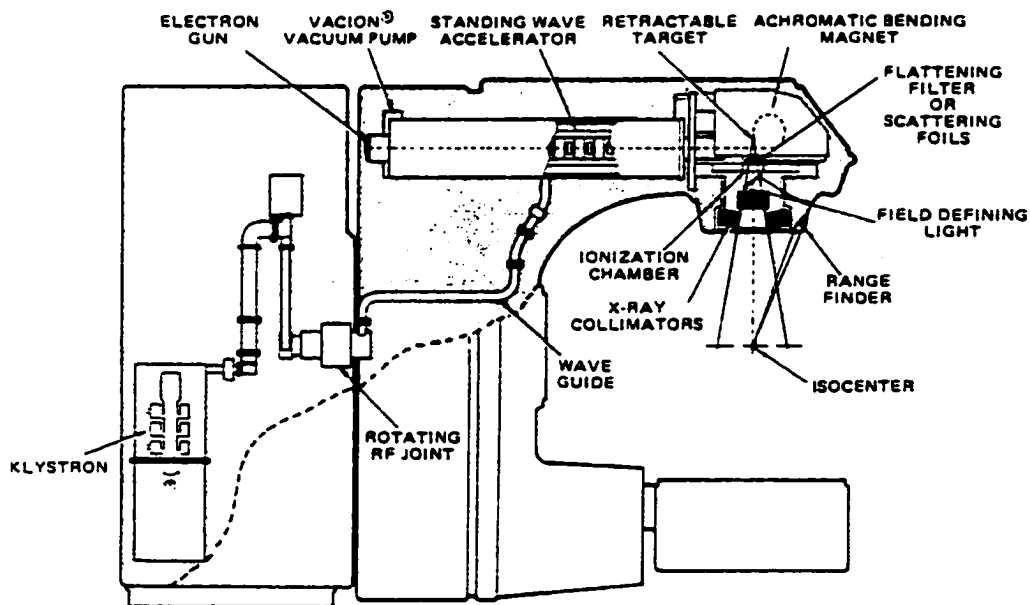


FIG. 35 Schematic of major subsystems in Clinac 20 - Varian (from [51])

The field size and its position on the treatment couch can be visualized by a light field congruent with the radiation field. The light source projects a light beam as if emitted from the X-ray focal spot.

Before irradiation of the tissue sample, the isodose<sup>18</sup> distributions were measured for the energy used, using an automated dose plotter. This is essentially a water phantom (a Plexiglas cube of about 1m<sup>3</sup>) with a small ionization chamber that can be moved along 3 independent axes under computer control, during irradiation, 'scanning' the absorbed dose profile. A number of such profiles are shown in the Figures 1-3 in the Appendix A.

<sup>18</sup> Volumetric and planar distributions of the absorbed dose, represented by planes or curves passing through points of equal dose. The depth dose is usually normalized at the point of maximum dose on the central axis and drawn at equal increments of percent depth dose.

Also in Appendix A, shown in Figure 4 is an artist's view of a modern Clinac. The next figure (Fig. 5) in the Appendix A, represents the real accelerator used in our experiments at VBGH, under the direction of Dr. Raymond Wu.



## **CHAPTER VI**

### **DATA ANALYSIS**

This chapter is devoted to data analysis. We will start by a description of the methods used to validate and fit the data acquired in the impedance measurement. The analysis of each of the tissue specimens will then proceed, with different sections for blood, kidney, liver, lung and heart. Because of the particularities of each of the systems investigated, we will have a brief description of the specific structure and function of the tissue discussed, followed by a presentation of known dielectric data gathered from literature. Whenever prior knowledge on the irradiation effects on the tissue under discussion exists in the radiobiological literature, we will refer to it. Since the tissue used was excised, we will present data about the time evolution of the impedance for non-irradiated samples. The most relevant results of our impedance measurements will be presented and a model for analysis will be proposed. At times, we will present successive iterations leading to a final electrochemical model, and the time evolution of the model parameters is presented with and without irradiation. The most difficult part of the analysis will follow, discussing how the analysis of the model and the time evolution of its parameters, shortly after the sample irradiation, can be interpreted. Conclusions will be drawn in the sense of discriminating between oncosis and apoptosis cellular death following irradiation.

#### **Data validation and fitting**

One of the first methods of spotting anomalies in data, strongly recommended by Macdonald [52], is plotting the data in three dimensions, for all 4 functions  $Z$ ,  $M$ ,  $Y$  and  $\epsilon$ , and choosing the one which resolves best the experimental data over the entire frequency range analyzed. This visualization technique is valuable because for a given parameter, one can see all projections at once and outliers, which are sometimes difficult to see in one representation, are more easily spotted. In the same way in which the beauty of a mathematical representation is an indication of correctness, the smoothness of the frequency data, the lack of abrupt changes, are an indication of good quality impedance

data. An example of a 3D plot for a simple series combination of RC parallel circuits is shown in Figure 36.

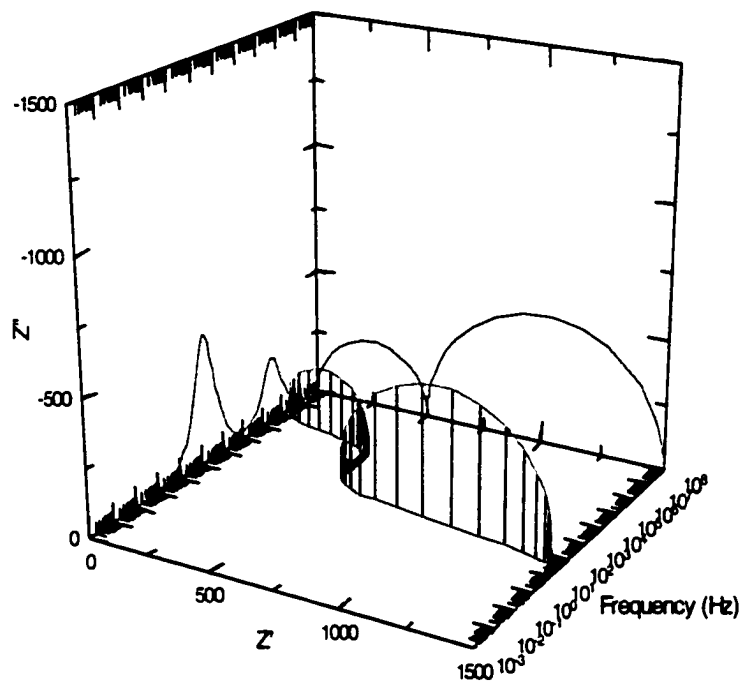


Figure 36. Three dimensional plot of a sample circuit's impedance response (the units for  $Z' = \text{Re}(Z)$  and  $Z'' = \text{Im}(Z)$  are ohms).

We have used this primary visual test throughout our experiments.

A number of conditions have to be satisfied in order to analyze "good" impedances. It is usually easy to recognize features of impedance spectra that can be assigned to certain processes or structural elements. Sometimes though, impedance spectroscopy (IS) is applied to systems that have not been measured before, leading to Bode plots difficult to analyze in relationship to existing data. In such cases, there is a general mathematical procedure, introduced by Kramers [53] and Kronig [54] that can test whether the acquired impedance data is physically correct. Assuming that general

criteria like linearity, causality, stability and finiteness are satisfied, the *Kramers-Kronig relations* enable one to calculate the real component of the impedance  $Z' = \text{Re}(Z)$  from the imaginary part  $Z'' = \text{Im}(Z)$  and vice versa:

$$Z'(\omega) - Z'(\infty) = \left(\frac{2}{\pi}\right) \int_0^{\infty} \frac{xZ''(x) - \omega Z''(\omega)}{x^2 - \omega^2} dx \quad (73)$$

or if the zero-frequency asymptote of the real part is known, the following equation is used:

$$Z'(\omega) - Z'(0) = \frac{2\omega}{\pi} \int_0^{\infty} \left[ \left(\frac{\omega}{x}\right) Z''(x) - Z''(\omega) \right] \frac{1}{x^2 - \omega^2} dx \quad (74)$$

The imaginary part can be obtained from the real part, using:

$$Z''(\omega) = -\frac{2\omega}{\pi} \int_0^{\infty} \frac{Z'(x) - Z'(\omega)}{x^2 - \omega^2} dx \quad (75)$$

The phase angle can be computed from the magnitude of the impedance,  $|Z|$ :

$$\varphi(\omega) = \frac{2\omega}{\pi} \int_0^{\infty} \frac{\log|Z(x)|}{x^2 - \omega^2} dx \quad (76)$$

and the polarization resistance can be extracted from the imaginary component  $Z''$ :

$$R_p = Z'(\infty) - Z'(0) = \frac{2}{\pi} \int_0^{\infty} \frac{Z''(x)}{x} dx \quad (77)$$

The main difficulty in implementing these relations is the fact that the integration have to be carried out from  $0$  to  $\infty$ , while the data is collected only for a finite interval. A number of methods are known, among them, polynomial fitting and then analytical integration or the use of the so-called Voigt model (a series of parallel RC circuits) in which since each

RC circuit is transformable, the whole circuit will also be transformable (and the integration is thus replaced with an equivalent circuit fit).

A short comment on the requirement that the impedance be stationary is worthwhile: most of the biological systems do not satisfy this requirement, simply because a living system is a dynamical system. Because of this, the impedance might change during the actual measurement. Our measurement on irradiated blood, before and during the irradiation, was meant to put in evidence precisely the variation of the impedance in time, for a fixed frequency. One important drawback is that since we observed interesting features at low frequency, the measurement can take a long time. For consistency, we replaced this condition with fixed initial conditions; when during a frequency sweep there were reasons to suspect a non-stationary behavior, we repeated the measurement, preserving the direction and timing of the sweep (*e.g.* from high to low frequency, the same number of points per decade).

### **Data modeling**

Before discussing the Complex Nonlinear Least Squares (CNLS) fitting procedure, which is at the heart of the model parameter identification, we will discuss the choice of the model. This is one of the most difficult steps of applying Impedance Spectroscopy! The criteria for a certain model can be prior knowledge on certain physicochemical processes or on the structure of the investigated system. A formal or mathematical model can be used as well, but interpreting the model will be in this case more difficult. The way we have proceeded, the first step was an elementary analysis: for non-overlapping semicircular arcs in the impedance plane one can directly estimate the associated RC values and the value of the peak of the arc  $\omega_m = (RC)^{-1}$ . The procedure gives good estimates for initial values, which taking into account the inherent instability of a nonlinear fit is a considerable advantage. Further contributions from circuit elements that are described by closed-form equations can be identified (*e.g.* CPE, discussed in the next section).

A supplementary difficulty can come from the mismatch between a more elaborate model and an incomplete impedance spectrum. In the case of a system, for

example, the complete impedance spectrum can consist, in the complex plane, of two semicircles, but experimentally only one can be identified (the other may be in a frequency range inaccessible because of experimental difficulties). A criticism of equivalent model fitting is the fact that in complex models a large numbers of free variables are present, and sufficient experimental data have to be provided, to be able to characterize all parameters. It was our practice, through this work, to always use the minimum number of circuit elements that fitted the experimental data. When the initial proposed equivalent circuit was fitted with the data, we identify the contribution of each process, and when the data did not support it, or the contribution was not significant, we simplified the circuit. In some cases, the contribution of different processes is shown and discussed explicit.

It should also be pointed out that there is *no uniqueness theorem* guaranteeing that a good choice for a model or equivalent circuit is unique. Several different equivalent circuits, though indistinguishable in their impedance response can be used to model the same experimental data, especially if there are errors in the data.

Since one of the most common features of the complex impedance plots of impedance data on biological tissues is the Cole representation of "depressed arcs", we are discussing the modeling and interpretation of this one in more detail. The empirical representation is:

$$Z = R_{\infty} + (R_0 - R_{\infty}) / \left[ 1 + (i\omega/\omega_0)^{\alpha} \right], \quad (78)$$

often substituted, in order to represent the high-frequency behavior, by the "Constant Phase Element" CPE, of impedance:

$$Z_{CPE} = K (i\omega)^{-\alpha}. \quad (79)$$

Basically, we have three choices when modeling with the Cole equations: to represent the data empirically, attribute physical significance to the parameters in Eq. (78) or derive an equivalent circuit and attribute physical significance to the circuit components. Many authors relate the parameter  $\alpha$  to a "distribution of relaxation times". In fact, this being an

empirical model, the possibility of such distribution doesn't necessarily mean that a particular distribution has physical existence. Jonscher [55] in his series of articles on the "universal" dielectric response, also vigorously criticized the interpretation of  $\alpha$  as characterizing a distribution. The equivalent circuits (also used by us) are thought to reflect relationships between various underlying physical processes. A problem is their uniqueness (or better say, the lack of) and the fact that a particular choice depends very much of the researcher's physical intuition. Using a large number of parameters, an excellent fit can be obtained, even if the equivalent circuit employed has little relevance for the system under investigation. Another problem related to the choice of model and the composing elements is the mathematical expression used to describe them. The CPE element for example is described generically by the Eq. (79) but there is little physical significance that can be attributed to the constant  $K$ . The expression we used to describe the constant phase element is:

$$Z_{CPE} = R(i\omega T)^{-\alpha}, \quad (80)$$

where  $R$  has units of  $\Omega$  and  $T = 1/\omega_0$  can be considered an "average time constant". An "effective capacitance" of the system can sometimes be also derived,  $C_{EFF} = R^\alpha T$ , but since it is the particular value of capacitance at  $\omega = 1$ , it doesn't mean much. The most consistent interpretation of such elements is that they are distributed in space. Biological tissues especially constitute systems in which interfaces and distribution of the microscopic properties thought the sample are very important, so the need, in fitting the data, of CPE elements simply signals such behavior. Given the complexity of the physicochemical processes, it is often our only choice to describe them by using continuum models expressed by equivalent circuits.

Once we develop a model, the fitting procedure have to be used in order to extract the parameters of the model and their uncertainties. The CNLS program used in this work was developed by Macdonald [56] and distributed as public domain software by Solartron. Inc. The program can fit real, imaginary or complex (simultaneous real and imaginary components) impedance data. The program minimizes the sum of squares:

$$S = \sum_1^N \left\{ w_i \left[ Z'_{i,\text{exp}} - Z'_{i,\text{calc}} \right]^2 + w_i \left[ Z''_{i,\text{exp}} - Z''_{i,\text{calc}} \right]^2 \right\} \quad (81)$$

with  $Z'_i$  and  $Z''_i$ , the impedance components for  $\omega$ . Most often, a Marquard-Levenberg algorithm is used for the minimization of (81) but other solutions are used to ensure that the minimum found is indeed an absolute minimum in the parameter space.

An important problem, not always well-defined, is the choice of statistical weighting in CNLS. Because impedance is measured over a large frequency domain and may vary by orders of magnitude, if a unitary weighting is used ( $w_i = 1$ ) only the largest impedances will contribute to the sum  $S$ . In theory, one should just repeat the experiment 10 times (or a large enough number) and determine the  $w_i$  from the standard deviations. Such a procedure though, is very difficult to apply when measuring biological material, and impossible under the measurement & irradiation technique used for our work. An alternative, the proportional weighting, is to take the  $w_i$  coefficients inversely proportional to the measured (or calculated) impedances:  $w_i = 1/Z_{i(\text{calc or exp})}^2$ . Such weighting implies that the real and imaginary part of the impedance are determined with independent precisions, which is not always the case. A more common approach to weighting is the use of the modulus, such that the statistical weights become  $w_i = 1/(Z'^2 + Z''^2)$ . As result of the model-fitting process, we obtained both  $\chi^2$  and the weighted sum of the squares, as indicators for the goodness of the fit, as well as the model parameters and their errors. The main criteria of accepting the fit with a certain model, was the ability of the model to describe both low and high frequency data, while remaining physical meaningful. The indicators for the goodness of the fit were used mainly in the batch fitting (when a large number of impedance spectra were fitted with one model), to ensure that their value was consistent throughout the whole batch.

In the next section, we will begin analyzing the impedance data obtained on different tissues. The specific microstructure, as well as arguments for the model choice and its parameters are given for each tissue type.

## Blood

Blood is a fluid tissue, which constitutes about 7% of the body weight (for an average human adult about five liters in volume). The whole blood of normal human subjects consists of a concentrated suspension of red blood cells (approximately 40-45% in volume, with white blood cells and platelets contributing less than 1%) in plasma. Plasma contains about 7g/dl proteins (albumin, globulins and fibrinogen), nutrients (minerals, vitamins, glucose), complex macromolecules carrying blood lipids, hormone growth factors, vasoactive peptides, etc. Fluid representing a protein-poor filtrate of the plasma diffuses through the walls of fine blood vessels and enters the perivascular tissue carrying nutrients, hormones and other regulatory compounds.

Freshly drawn blood is a red fluid of relative density 1.052-1.064. On standing, it rapidly coagulates into a jelly like mass due to extensive red blood cells aggregation. The prerequisite for this phenomenon is the presence of certain macromolecules in the suspending medium, such as fibrinogen and some globulins fractions, which normally occur in the plasma blood. The so-called rouleaux ('piles of coins') formation, known from the mid 18<sup>th</sup> century, was recently investigated by using impedance spectroscopy with the aim of elucidating its growth mechanisms. However, if clotting is prevented (by adding anticoagulants) the blood cells settle, leaving the plasma supernatant. The physiologic pH of the blood is 7.4; it is a highly buffered fluid.

An obvious question that can arise is: why should we study radiation-induced effects in blood? Well, there are few answers to that. First, because it is an easily obtainable<sup>19</sup> and readily available system. Secondly, but not less important, is that it fits the description of the so-called "mixture model", a suspension of cells in an electrolyte, employed by Schwan, [30, 31] and other pioneers of the field, in explaining the Maxwell-Wagner theory of interfacial polarization. When irradiation comes into play, microcirculation and tumor - as well as healthy tissue - blood flow are important factors in the oxygen and nutrient supply of tumors.

---

<sup>19</sup> *Obtainable* only refers to Dr. Wu's efforts, for which I'm one more time thankful.



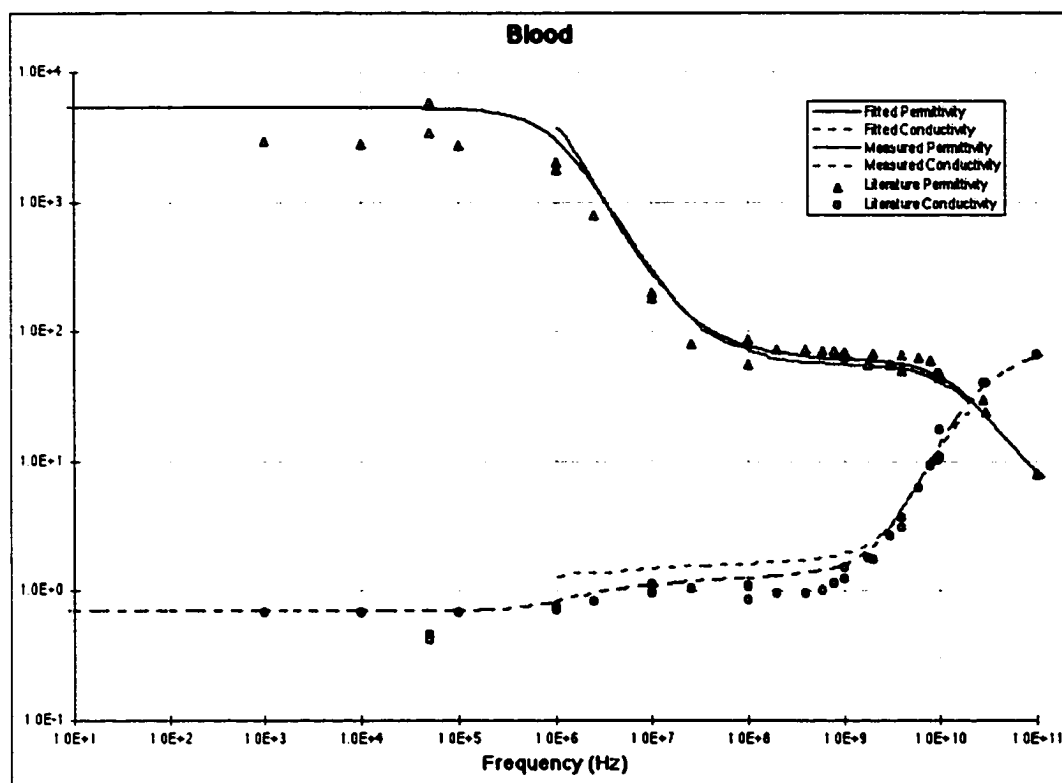


FIG. 37. Data gathered from literature on whole human blood [58]. Shown on the vertical logarithmic axis are both  $\epsilon_r$  (value) and  $\sigma$  (S/m).

From the dielectric point of view, blood is more conductive than other tissues ( $\sigma \cong 0.6$  S/m), and its relative permittivity,  $\epsilon_r$  around 2000, is a function of the hematocrit<sup>20</sup>. For this reason, when tissues with a heterogeneous structure and strong vascularization are investigated at low frequencies, the current path is likely to be, through blood to a large extent [57].

To give the reader an overall image about the known dielectric properties of blood we are presenting, in Figure 37 and Table I of Appendix B, information gathered from literature by Gabriel [58] and Andreuccetti [59]. Fig. 37 reflects the data gathered in different studies on whole human blood. A parametric model, (who's fit is also shown on the graph) was created by Gabriel *et al.* [58] in which the permittivity is considered to be the sum of up to six Debye or Cole-Cole terms:

$$\varepsilon(\omega) = \varepsilon(\infty) + \sum_n \frac{\Delta\varepsilon_n}{1 + (i\omega\tau_n)^{(1-\alpha_n)}} + \frac{\sigma_{ionic}}{i\omega\varepsilon_0} \quad (82)$$

Based on this model, Andreuccetti *et al.* developed a computer code [59] which calculates electric permittivity and conductivity for a specific tissue, for specific conditions (frequency range). The results of this calculation for whole blood, as a function of frequency, are shown in Table I of Appendix B. In Fig. 37, one should remark that there are no experimental points at frequencies less than 1kHz, pointing out that many experimenters avoid the low frequency domain.

### *Radiation induced changes in blood*

Red blood cells (erythrocytes), because of their numerous advantages - availability, characteristic size and metabolism, easy isolation of the cell membrane - are well-studied systems in radiobiology. A number of radiation induced effects are reported: an early structural membrane modification after irradiation [60], damage of the ionic pumps ( $\text{Na}^+$ ,  $\text{K}^+$ ) [61], swelling, changes of the membrane permeability [62] probably due to peroxidation of lipids and decrease in the antioxidant enzymatic activity. When irradiation occurs *in-vivo* an additional effect may be due to radiation damage on the endothelium in the microvessels, which could lead to an increase in the vascular permeability. An increased excretion of  $\text{Cl}^-$  on the first day after irradiation is known in literature under the name of polyuria. In the high dose region from 14 Gy up to 20 Gy, the increased supply capacity of blood in tissues suggests radiation-enhanced vascularization (probably the cause of edema, one of the very few visible radiation effects). One of the most radiation sensitive cells is the small lymphocyte. Small lymphocytes disappear from blood after very small radiation doses, and it is believed that they suffer inter-mitotic death. Most sensitive cells die a mitotic death after irradiation; most cells which never divide (among them the lymphocyte) usually require very large doses to kill them [63].

---

<sup>21</sup> The ratio of the volume of the packed red cells to the volume of the whole blood

In body fluids, under irradiation, a number of possible mechanisms of action causing changes in concentration of substances in body fluids in general, can be imagined:

- Release from a tissue or uptake by a tissue.
- Temporary damage to the cell membrane leading to increased level of serum enzymes due to leakage from cells.
- Abnormal cellular metabolism and subsequent release of metabolites into the blood.
- Destruction of cells (ex. Loss of nucleic acid metabolites from lymphoid tissue into the blood and urine; increase in the blood iron).

The change in the total blood volume results primarily from changes in the number of red cells, and secondarily from those in the plasma volume. Changes in electrolyte metabolism have been reported in patients during radiation therapy [64] but, most likely, these reflect the underlying malignant disease processes rather than the influence of radiation. Irradiation causes changes in blood level and urinary excretion of many compounds of low molecular weight. An increase in the blood glucose, perhaps related to changes in glycogen metabolism, is frequently observed during the first hours after irradiation. Serum enzymes have their origin in various organs of the body from which they are released into the serum. Changes after irradiation may represent release of enzymes from radiosensitive tissues or may be due to changes in synthesis. Conductivity, viscosity and surface tension of the blood are also reported in the literature to show significant alteration during the first hours after exposure [65].

#### *Frequency response of blood during irradiation*

While blood constitutes a thoroughly studied system from the electrochemical point of view and its dielectric properties are well known, no dielectric measurements have been performed on irradiated blood, to our knowledge. We designed our first experiments, with the idea of measuring dielectric changes of the system *during* the irradiation process. At that time, the idea that we followed, briefly sketched, was the following: body fluids, blood especially, should be a very important component of the free-radical mediated processes of radiation damage. The serum ability to resist attacks by free radicals is

measured by the total peroxy radical-trapping potential (in plain words, the length of time that a subject's serum is able to resist artificially induced peroxidation). At first, the antioxidants in the sample will be consumed by the free-radicals induced by radiation and no extra charge carriers will be available. After a lag phase, the free-radical dynamic will simply be governed, in a steady-state regime, by the generation-recombination rates. Of course, this is a simplistic view of an otherwise extremely complex picture: the free-radicals are created both in the intracellular and extracellular space so they are prone to damage both organelles and DNA as well as the plasma membrane and the surface receptors embedded in it. Some of the damage will be enzymatically repaired, some not. An arbitrary number of charged species will be created, with arbitrary mobilities and bulk concentrations. Reaction-adsorption (with different conditions for each of the mobile species) will take place both at the electrodes and membrane interfaces. It is likely that, due to the fluctuation in the number of charge carriers and their diffusion, the electric double layer (Gouy-Chapman) will be distorted and that will be observable in the capacity associated with it and the resistance associated with the charge transfer.

The frequency domain in which we pursued our investigation, covered both  $\alpha$  and low  $\beta$  dispersions, as well as what is sometimes referred to as the  $\Omega$  dispersion [40, 66]. The later, which is a more extended interpretation of the low frequency response (down to frequencies of  $10^{-4}$  Hz) seems to be due to the electrochemical (in our case, also radiation induced) generation of ions at the electrode surface, ionic conduction, trapping and relaxation of charge among traps, while the regular  $\alpha$  dispersions would be due to charge hopping in the bulk sample. The usual thinking is that at low frequency, the measurement of dielectric processes of the bulk sample is affected (or corrupted) by the electrode polarization. Our strategy was to model and use the information about the processes taking place in the proximity of the electrode, along with that about the bulk sample. A biological sample under irradiation with high-energy photons is an extremely complex system that can be studied at numerous levels. Having in mind that the role of radiation is to kill the cell, we will examine the relevant processes that can provide information, which can be connected to the death of the cell. In this context, it should be mentioned that the irradiation of blood for transfusion is a current procedure in hospitals.

The raw data collected on samples before and during irradiation is presented in Fig. 39. The measurements used a two electrodes configuration. A parallelepipedic glass cell of (12 x 12 x 2) cm was filled with about 200 ml heparinized whole blood from a perfusion bag. The Pt band electrodes (2.0 x 0.4) cm were placed at the periphery of the cell, such that they were outside of the (10 x 10) cm irradiation field. The blood was stirred before and between the measurements but not during the measurement. The temperature was checked during the measurement session and founded 21.3 °C; the typical measurement time was 320 s. The measurements on blood were carried out *during* the irradiation. This was consistent with the idea we followed at that time, that a change in the steady state concentration of charge carriers, reflected in the conductivity, must be in same relation with the lifetimes of free radicals and implicitly with the serum ability to annihilate them.

The first iteration in modeling this system response is based on the observation that there are two visible dispersions: one at high frequencies, probably a low  $\beta$  that can be assigned to the bulk suspension of cells in plasma, and another one, related to the electrode interface. While the one at high frequency is represented in the complex plane by the semicircle that we normally expect from RC-like dispersions, the low frequency one is 'sunk', its center is below the real axis, suggesting the use of a distributed element.

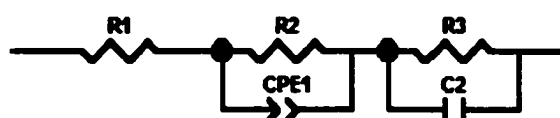


FIG. 38. Equivalent circuit used in a first approximation.

The result of fitting the experimental data with this model is shown in Figure 40. The high frequency dispersion is well fitted, but not the low frequency one.

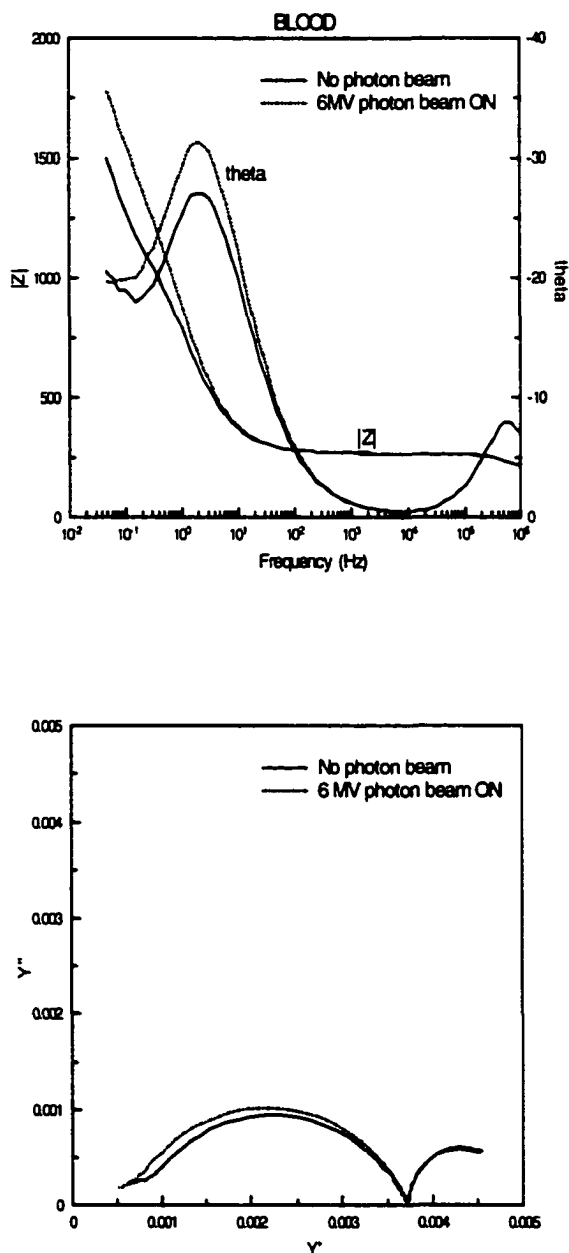


FIG. 39. Impedance spectra on whole blood, before and during irradiation, in the frequency range (50 mHz-1 MHz). a)  $(Z, \theta)$  impedance modulus-phase representation; b)  $(Y'', Y')$  admittance<sup>21</sup> complex plot

<sup>21</sup> Admittance  $Y$  is the inverse of the impedance  $Z$ :  $Y = Z^{-1}$

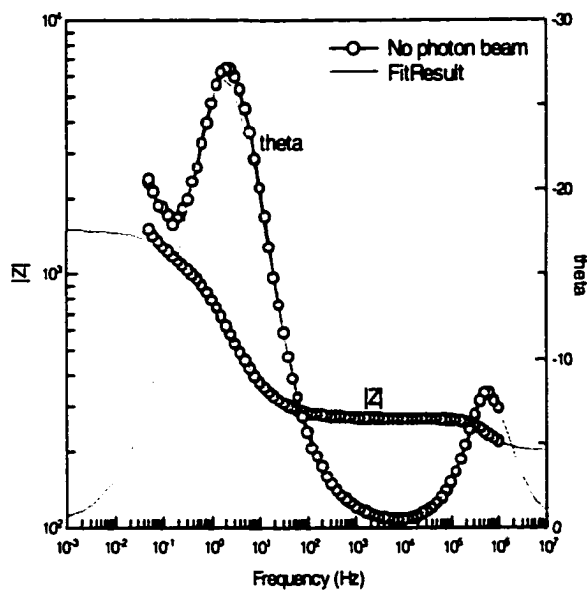


FIG. 40. Simulation of frequency response for the circuit in Figure 38. a)  $|Z|$  and  $\theta$  vs. frequency representation ( $Z=|Z|e^{i\theta}$ ); b) Complex plane representation.

The numerical values of the model are:  $R_1 = 202.4 \Omega$  represents the resistance of the electrolyte (plasma blood); the high frequency dispersion, very likely a membrane response, represented by  $R_3C_2$  ( $61.94 \Omega$  and  $5.101 \text{ nF}$ ) has a relaxation time of  $\tau \cong 32 \mu\text{s}$ , corresponding to a frequency of about  $503.7 \text{ kHz}$ . The CPE element has a capacity of  $381.77 \mu\text{F}$  and an exponent  $\alpha$  of  $0.67$ . The resistance  $R_2$  is a charge transfer resistance (explained later in the chapter) of  $1237 \Omega$ .

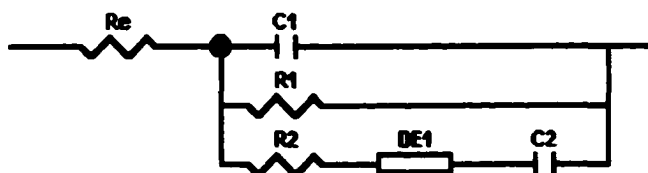


FIG. 41. Improved equivalent circuit for whole blood data

The next step in improving the response of the equivalent circuit is to add a distributed element DE, as shown in Fig. 41. The result of the fit with the improved model is shown in Figure 42:

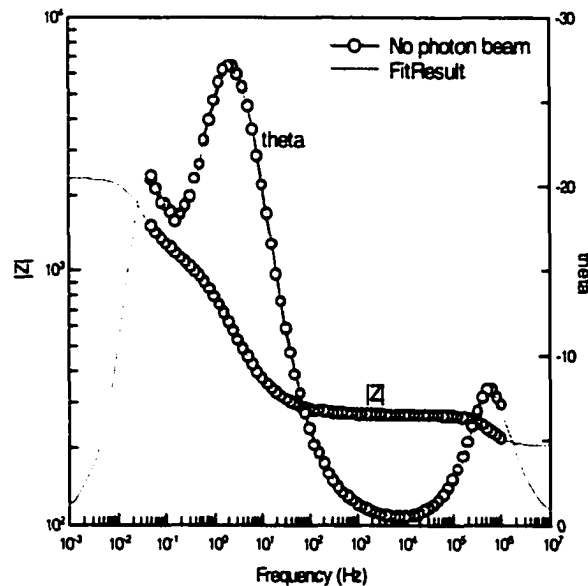


FIG. 42. Impedance modulus and phase vs. frequency representation of the non-irradiated blood. The continuous line represents the fit with the model and the frequency domain was extended to check if the fitted response is physical meaningful (finite response at very high and very low frequencies).

This circuit was suggested by the processes known to take place at the cell membrane interface as well as the interface electrode-electrolyte and which are observable in the frequency domain investigated. Under the effect of a continuous delivery of ionizing radiation the chemical composition of the extracellular medium is definitely affected. As a result, it is expected that the redistribution of minority ion concentration ( $\text{Na}^+$ ,  $\text{K}^+$ ,  $\text{Ca}^{2+}$  and  $\text{Mg}^{2+}$ ) will significantly change the cell's ionic boundary, with possible (electro)biochemical consequences. It is the change in the potential of the interfacial layer (membrane-extracellular fluid) and the relaxation time dependence of specific



interactions involving membranes sites that can greatly affect cell development and function. A charged species can be imagined interacting with a membrane surface site through changes in the hydration layer, displacement or spatial distribution changes. Since the concentration of water dipoles in tissue electrolytes is much larger than of any other ions, the first layer (Stern) of membrane bounded water dipoles will not suffer changes due to the modification of the ionic atmosphere. The Gouy-Chapman layer will be influenced by the adsorption of hydrated ions.  $R_2$  and  $C_2$  from the equivalent circuit describe (or represent) the adsorption (binding) kinetics and surface concentration.  $C_1$  represents the observable dielectric and electrostatic response, caused mostly by the lipid bilayer structure.  $R_1C_1$  are represented by the peak appearing at about 503 kHz. The distributed element DE has a more blurred physical interpretation. In general the distributed elements are very important in understanding, fitting and interpreting the impedance spectra. The word *distribution* can be used in two different ways. One is associated with nonlocal processes (*e.g.* diffusion) which can occur irrespective of the homogeneity of the sample or its physical properties (*e.g.* charge mobility). The other interpretation, by contrast, is based on the fact that sometimes the microscopic properties are themselves distributed. For example, [67] when a time constant associated with either a bulk or interface process exhibits a temperature dependence and is thermally activated with a distribution of energies, a series or parallel RC circuit is no longer appropriate and a CPE element is used instead. In our choice for the *type* of the distributed element, we would be tempted first to choose a Warburg impedance (semi-infinite diffusion, typical for cell-fluid interface). Such an element has an impedance of the form:

$$Z_w = \sigma\omega^{-1/2} - i\sigma\omega^{-1/2}, \quad (83)$$

where  $\sigma$  is given by:

$$\sigma = \frac{RT}{n^2 F^2 c \sqrt{2D}}. \quad (84)$$

When this impedance is plotted in the complex plane, is represented by a semicircle connected to a straight line at 45° from the real axis. What we obtained was not a 45°

angle, and an attempt to fit the data with an equivalent circuit (not shown) containing a Warburg element failed. Therefore we used a more general type of distributed element, which in limiting cases can become a diffusion impedance. Its generic form is

$$Z(\omega) \propto A(i\omega)^{-\alpha}, \quad (85)$$

where the coefficient  $\alpha$  is a measure of how wide the distribution of relaxation times is.

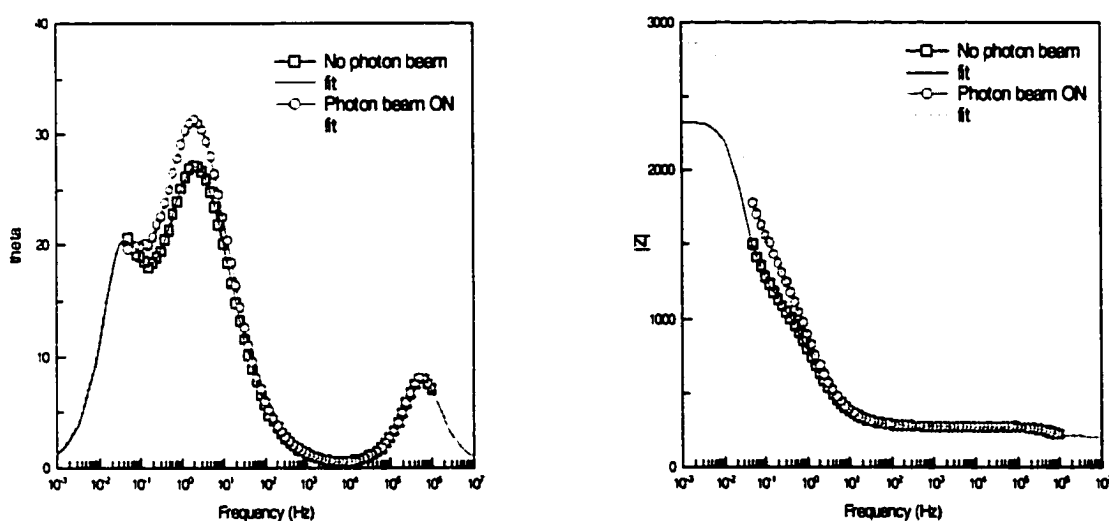


FIG. 43. Comparison between data and fit of the equivalent circuits describing the data shown in FIG. 41.

$\chi^2$  and respectively the sum of squares, for the fit of experimental values with the model are  $(2.944 \cdot 10^{-6}, 4.063 \cdot 10^{-4} \Omega^2)$  for the non-irradiated sample and  $(6.334 \cdot 10^{-6}, 8.741 \cdot 10^{-4} \Omega^2)$  for the irradiated sample. The numerical values of the parameters used in the equivalent circuits for whole blood and irradiated whole blood are shown in Table IV.

TABLE IV. Values of the parameters in equivalent circuits from Fig. 41 fitted to data shown in Fig. 43. The two values shown for each parameter correspond to the non-irradiated sample (first) and the irradiated one (second). In bold are the values which differ significantly during irradiation.

$Re (\Omega)$	$Re(\text{Error})$
203.4	0.2909
203.1	0.5841
$C1(\text{F})$	$C1(\text{Error})$
4.77E-09	4.85E-11
4.80E-09	9.63E-11
$R1(\Omega)$	$R1(\text{Error})$
<b>2136</b>	10.81
<b>2680</b>	31.94
$R2 (\Omega)$	$R2(\text{Error})$
67.35	0.3017
66.36	0.5988
$DE1-R (\Omega)$	$DE1-R(\text{Error})$
<b>1723</b>	5.045
<b>2318</b>	14.89
$DE1-T$	$DE1-T(\text{Error})$
0.000234	8.60E-07
0.000232	1.57E-06
$DE1-P$	$DE1-P(\text{Error})$
<b>0.7137</b>	0.0007
<b>0.7242</b>	0.0013
$C2 (\text{F})$	$C2(\text{Error})$
<b>0.001764</b>	1.77E-05
<b>0.001405</b>	3.99E-05

### *Time dependence response*

The second type of experiment we did on blood was the time domain measurement, presented in Fig. 44. The signal acquisition was initiated and after a time interval of 40 s the photon beam was activated. The photon beam energy was 6 MV with a size of (10 x 10) cm field and it delivered a dose of 10 Gy. Two Pt band (2 x 0.4) cm electrodes, at 12 cm distance, positioned outside the irradiation field, were used for measurements.

The idea was to check whether differences in the measured impedance can be seen immediately after the photon beam is activated, and which of the two components  $Z'$  or  $Z''$  are more sensitive to these changes. The impedance measurement was carried out at constant frequency of 1 Hz with a constant current excitation of  $i = 50 \mu\text{A}$ . It is clear that in this electrode configuration (only for the blood samples) interfacial phenomena played a significant role, along with the bulk of the sample. We believe that 2 different effects are present in these measurements: interfacial reaction, seen at short times and mass transport processes, at longer times. As often the case in the *ac* measurements, a steady state obtained in the frequency domain, might correspond to a transient state in the time domain. As shown in Fig. 44, the beam was switched on after 40 s, at which time a change in the traces representing  $Z''$  become evident. The resistive part of the impedance,  $Z'$  doesn't show any changes when the beam is switched on. The time variation of  $Z''$  without the photon beam on is believed to be a dynamic response of the interfacial electrode-electrolyte double layer to the low frequency applied. The dynamic behavior observed in the time domain measurements can be explained qualitatively by the interplay of electrode kinetics, transport processes occurring in the electrolyte and control device (potentiostat or galvanostat).

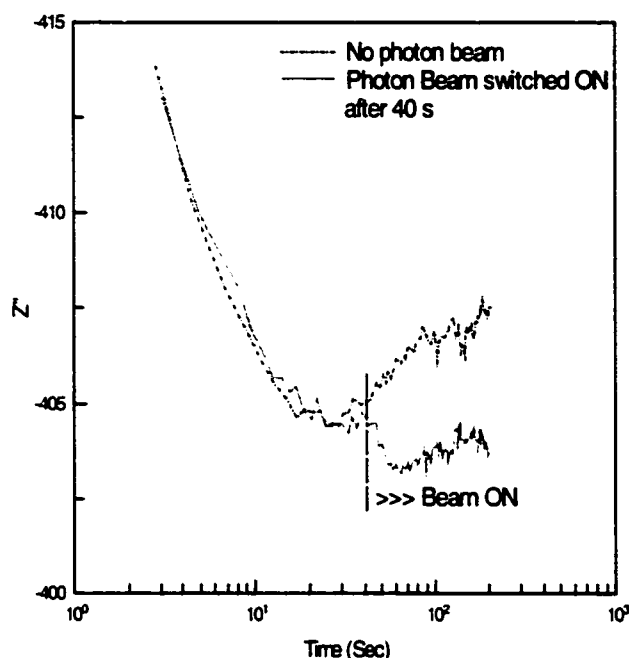


FIG. 44. Imaginary component of impedance,  $Z''$ , measured at 1 Hz, as function of time for irradiated and non-irradiated blood. The photon beam is activated after 40 s. No changes occurred in the real component,  $Z'$ .

It is known that some of the processes that show instabilities or oscillations in time are accompanied by spatial pattern formation. A thorough discussion of the subject can be found in [68]. What we will attempt here, is to describe a simplified model [69] capable of explaining such time instabilities.

The general equivalent circuit is shown in Fig. 45, and consists of a resistance  $R_e$  modeling the conduction in the bulk electrolyte and other external resistors, the capacitor  $C_{dl}$  modeling the diffuse double layer and a Faradaic impedance  $Z_f$  associated with the double layer at the electrode-electrolyte interface:

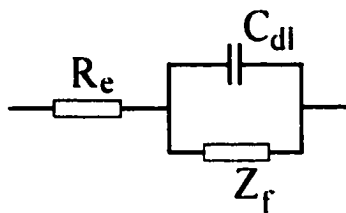


FIG. 45. Generic equivalent circuit used to model the dynamic instability.

The current  $i$  in the circuit is:

$$i = \frac{V - V_{dl}}{R_e} = i_c + i_f = C_{dl} \frac{dV_{dl}}{dt} + i_f, \quad (86)$$

where  $V$  is the applied voltage,  $V_{dl}$  is the potential across  $C_{dl}$ . A majority of our measurements were done under potentiostatic conditions, in which the generator output can be "balanced" in order to compensate for stray impedance or inequalities of the electrode impedance. The steady state solution  $dV_{dl}/dt|_{V_s=V_s} = 0$  (with  $V$  the constant applied voltage) leads to  $i_f = i = (V - V_s)/R_e$ . Assuming a small perturbation of the potential across the double layer in the steady state regime  $V_s = V_s + \delta V$ :

$$i_f(V) = i_f(V_s + \delta V) = i_f(V_s) + \left. \frac{di_f}{dV} \right|_{V=V_s} \delta V = i_f(V_s) + \frac{\delta V}{Z_f} \quad (87)$$

we can examine the stability of the stationary state described by Eq. (86):

$$C_{dl} \frac{d}{dt} \delta V = - \left( \frac{1}{Z_f} + \frac{1}{R_e} \right) \delta V, \quad (88)$$

which translates into  $Z_f > 0$ . The system becomes unstable if the right hand term becomes positive:  $Z_f < 0$  and  $|Z_f| < R_e$ . We should point out here that in the Solartron system, the measurement probe has build-in  $10 \text{ k}\Omega$  resistors in series with the electrodes, but that might not be enough for all situations encountered. In our blood measurements, the cell was about 12 cm wide and the electrodes were placed at the ends in order to place

them outside of the 10 x 10 cm radiation field and the conductivity of the electrolyte (serum) was fixed. Therefore, the usually available degrees of freedom in stabilizing the current-voltage relationship - repositioning the electrodes or increasing the electrolyte's specific conductivity - were not applicable. The faradaic current  $i_f$  can be expressed as:

$$i_f = nFAk(V_{dl})c_o \quad (89)$$

where  $n$  is the number of electrons involved in the charge-transfer process,  $F$ - Faraday's constant,  $A$  the electrode area,  $k(V_{dl})$  the heterogeneous rate constant and  $c_o$  the concentration of active species at the electrode-electrolyte interface. Knowing that  $Z_f^{-1} = di_f/dt$  and using the form for  $i_f$  given in Eq. (89), one can easily see how a negative  $Z_f$  can be obtained: a decrease of the available electrode area, a decrease of the electron transfer rate or a decrease of the concentration of electroactive species. The later is attributable to the double-layer effects. A quantitative analysis of the time measurement like those presented in Fig. 44 is extremely difficult given that, both with and without irradiation, the electrochemical system is far from thermodynamic equilibrium. We can only speculate, based on this model and on the fit parameters in Table IV, that changes, during the irradiation, of the resistance  $R_c$  and of the concentration of charge carriers and consequently of the double layer parameters moved the system from an oscillatory behavior to a bistable one.

### Conclusions

We have seen changes during the irradiation of the blood sample, both in the frequency and time domain. As seen in Table IV, the overall resistance of the sample, measured at low frequency, increases during the irradiation. The electrolyte resistance (serum)  $R_e$ , doesn't vary. Unlike the pulse radiolysis, where conductivity increase due to free radicals in a solution can be measured, in the continuous irradiation, the steady state concentration of free radicals is very small, unable to produce any significant changes. A major obstacle in detecting any change in conductivity due to free radicals is the fact that the conductivity of blood samples is significant even before the irradiation. The expected

change in  $\sigma$  is proportional with  $\sum_i \Delta c_i Z_i \lambda_i$  where  $\Delta c$  is change in the concentration of each ion,  $Z$  is the charge and  $\lambda$  is the equivalent conductance (ex.  $H^+$ : 314 S-cm<sup>2</sup>;  $OH^-$ : 172 S-cm<sup>2</sup>;  $Cl^-$ :65 S-cm<sup>2</sup>, etc.). Even though it is not obvious from the equivalent circuit (Fig. 41) the subcircuits reflecting the high frequency dispersion peak are  $R_1C_1$ , and  $R_2C_2DE_1$  for the low frequency one. In literature, erythrocytes are described as not having an  $\alpha$  (low frequency) dispersion, so we would be tempted to attribute the low frequency response to "electrode polarization". Due to the two electrode technique measurement, there are effects due to electrode polarization. We compared the blood samples with sea water, known to have properties close to the plasma serum and a powerful low frequency dispersion at about 2 Hz was evidenced, but not the double shoulder we can see in Fig. 43. One should to remember that these measurements were completed *during* the irradiation. Due to the uncertainty in attributing meaning to the low frequency impedance changes, we decided to change, for all the other tissue samples, both the technique - using exclusively four electrodes - and the timing of the measurements - the data acquisition started *after* the irradiation. No measurable changes during the irradiation, at frequencies associated with the cell membrane, were identified in blood.

### **Kidney tissue**

An extensive part of our study was done on kidney tissue. One of the reasons was the fact that even without elaborate preservation techniques, the kidney can be conserved up to 24 h with little or no deterioration. Another important reason is that it has long been recognized that kidney is quite sensitive to ionizing radiation, so we do expect to see this sensitivity also translated in changes of dielectric parameters. Reports showed that doses above 20 Gy regularly induced vascular and tubular injury that led to loss of functional tissue [70]. Histological studies of kidneys exposed to lower doses rarely showed signs of irreversible injury, although subtle changes in vascular endothelial cells could be detected.

A number of 7 kidney pairs were studied. We usually used the kidney pair harvested from the same animal in the following manner: one was kept in Krebs buffer in



an measurement cell, as a control sample, the other one being subjected to ionizing radiation in an identical cell. In general, our measurements were done either on tissue freshly excised, or kept at 5 °C in a refrigerator for 2-8 h. In both cases the organ was suspended in Krebs buffer. The tissue was irradiated with 6 MV photons; absorbed dose per fraction was 11.1 Gy. Four dose fractions were typically administered to all irradiated kidney samples. The effect of the excision was studied thoroughly, on kidney as well as on the other tissues. The temperature was actively stabilized at 22 °C. A four-terminal, (black Pt electrodes), measurement technique was used in order to minimize the polarization effects at low frequencies. To limit the temperature rise of the sample due to ohmic effects, we used (in the galvanostatic regime) a maximum current of 100  $\mu$ A. The controlled potential mode (potentiostatic regime) was also used.

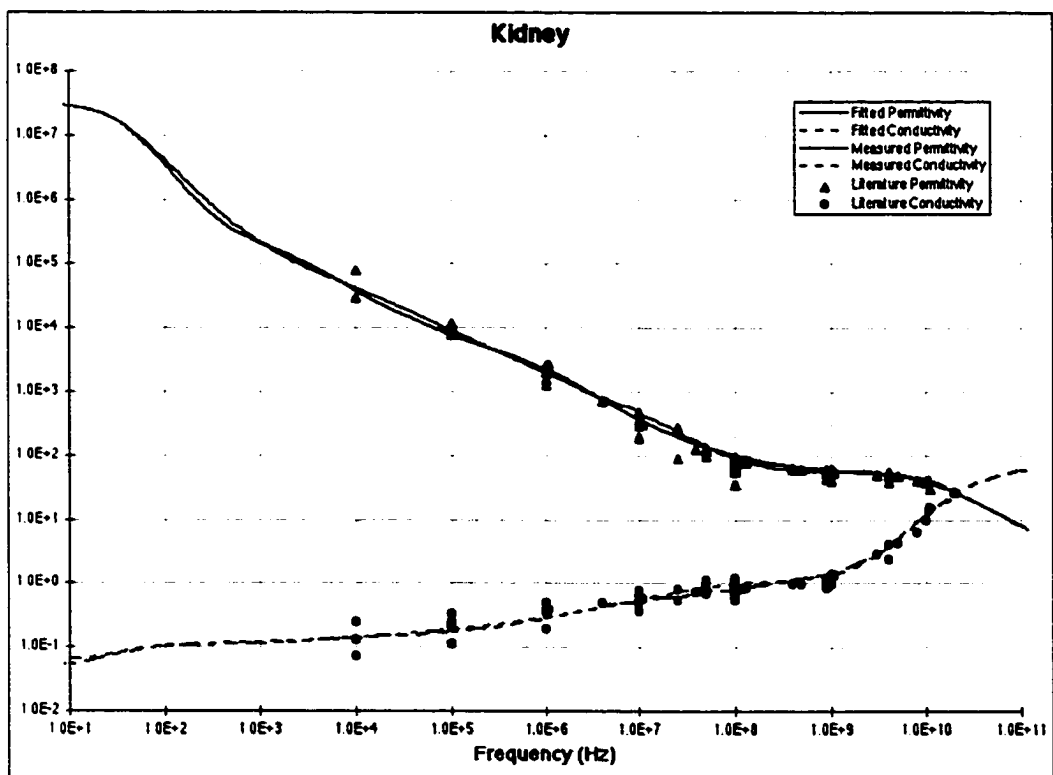


FIG. 46. Kidney data gathered from literature ([71])

The balanced generator helped reduce errors due to common mode voltages and dealt with difficult measurement situations where for instance the electrode impedances were not equal - a typical situation for bioimpedance measurements where it is difficult to obtain reproducible electrode contacts with the sample.

Driven shield cables were used to minimize the errors introduced by input and cable capacitance.

Thoroughly studied from dielectric point of view, the available information from literature was gathered by Gabriel [58] and Andreuccetti [59] and is summarized in Fig. 46 below and Table I in Appendix B. Should be noted that no experimental points are shown for frequencies lower than 10 kHz; on the other hand even the simple Cole-Cole model used by Andreuccetti predicts a low frequency dispersion in which we are particularly interested in our study.

Since our experiments were done on excised organs, it was very important to find out detailed information about the response of excised tissues. It is known that while the metabolism declines immediately after excision, the  $\beta$  dispersion declined noticeably only after metabolism has ceased and disappears in a few days. The changes are most prominent at low frequencies and it was suggested [72] that the response of the tissue after excision is a function of cellular damage, since freshly excised samples show responses similar with those obtained *in-vivo*.

Our data on excised samples, shown in Fig. 47, are typical for impedance spectra of organs during ischemia, as reported in the literature [73]. The main feature observed in  $Z' = \text{Re}(Z)$  is the increase of the impedance at low frequency, consistent with the closing of gap-junctions, cell swelling and accumulation of metabolic products. The dispersion peak in  $Z'' = \text{Im} Z(\omega)$  shows a displacement towards higher frequencies (from  $\sim 4$  kHz to 8 kHz). The six measurements displayed (in the order given in the legend) were recorded at  $t = 0, 837, 1539, 4227, 35098$  and  $36337$ s. For the first four, the low frequency resistance is increasing. The ion pumps at the membrane level have to stabilize the membrane potential and that requires energy, which is not supplied anymore by the blood carrying oxygen and nutrients.

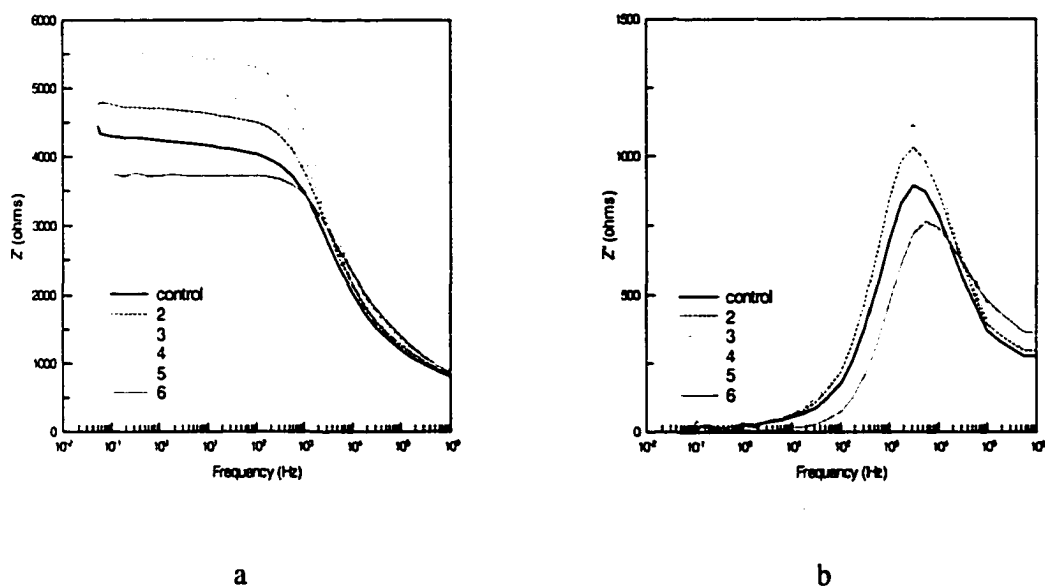


FIG. 47. Real (a) and imaginary (b) part of impedance for a kidney sample at different moments of time after excision. The samples were not irradiated. Times of measurement, starting with the control, are:  $t = 0, 837, 1539, 4227, 35098$  and  $36337$  s

Instead energy is gained anaerobically, and the cell swelling occurs as a result of intraintra-ionic ion production changing the osmolarity between the intra- and extracellular compartments.

The choice for the equivalent circuit shown in Figure 48, was suggested by the self-embedded micro architecture of the tissue [74]. In the case of an organ tissue, we are dealing with a very complex, highly structured environment. A modeling based on physico-chemical processes would be an extremely difficult enterprise. Instead, we chose to model the tissue using an equivalent circuit and to relate the circuit elements to these processes.  $C_1$  describes the interfacial polarization (due to the heterogeneous microstructure of the tissue) and its characteristic frequency is expected to be observed in the  $\beta$  region of the dispersion.

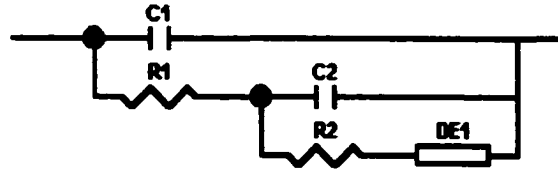


FIG. 48. Equivalent circuit for kidney samples

An expression for this capacitance is given in [75]:

$$C = \left( \frac{\pi kT}{\epsilon_0 c} \right)^{1/2} \frac{4\sigma^2}{\omega^2 L^2 e} \left[ 1 + \frac{\pi kT}{\epsilon_0 c} \frac{4\sigma^2}{\omega^2 L^2 e} (2 + \rho)^2 \right]^{-1} \quad (90)$$

where  $L$  is the specimen length,  $c$  is the concentration of charge carriers and  $\rho$  is a blocking parameter with values between 0 (complete blocking) and  $\infty$  (free passage of the charge -carrying species). Individual cells are surrounded by a membrane having low leakage, the interior containing cytoplasm with resistivity of the order of 3-400  $\Omega\text{cm}$ . The conduction pathway through the interstitial space is modeled by  $R_1$  and the membrane itself by the circuit  $C_2R_2$ . Given the complex structure of the tissue and the fact that not all cells have the same size/shape, they are not in the same cell cycle point, etc. we represented all these by the generic element DE (distributed element) in fact a Constant Phase Element characterized by the parameter DE-Phi in a series-parallel configuration with a resistor. In the expression of the impedance of the distributed element

$$Z_{DE} = \frac{R}{1 + (i \cdot \omega \cdot T)^{\text{Phi}}}$$

one can see the meaning of its parameters DE-R, DE-T and DE-Phi

plotted in the data analysis section.

The data on kidney were fit with the circuit shown in Fig. 47 and the numerical simulation for each set of data was extended to the frequency domain [ $10^{-3}$ ,  $10^8$ ] Hz in order to see clearly the behavior of the  $\alpha$  and  $\beta$  dispersion peaks. These numerical simulations are presented in Figure 49.

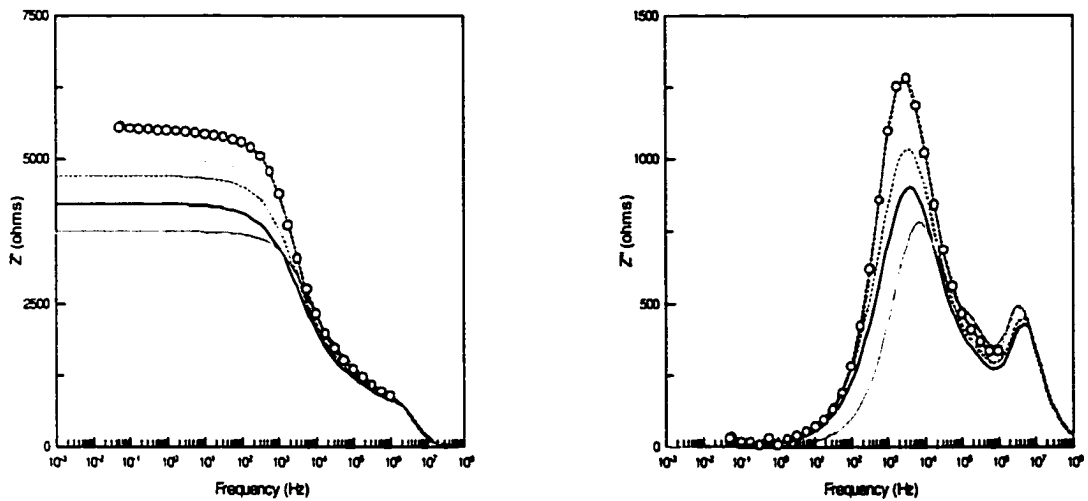


FIG.49. Numerical simulations of the equivalent circuit used to fit the kidney data (extended frequency domain). The experimental data (open circles) are shown only on one fit.

For the first four measurements, what we are seeing is basically cell swelling (and consequently a decrease of the extracellular pathways for current at low frequency) and the onset of oncosis.

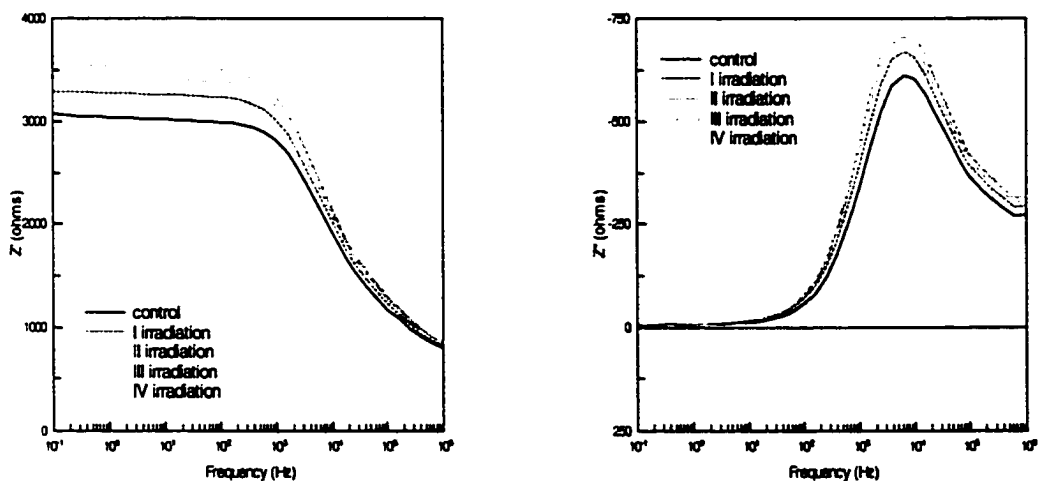


FIG. 50. Impedance spectra of irradiated kidney tissue samples.

Even though the kidney is known to be very resistant (can survive up to 24 h in a bucket with ice, in order to be transplanted) if one waits long enough (and given that the experiment was carried out at about 22°C), irreversible damage occurs, necrosis installs in the tissue, and the conductivity increases as a consequence of membrane breakdown. The slight shift in the  $\beta$  peak is probably due to the metabolically produced ions and an increase of the intracellular conductivity. To present the time dependence for all the model parameters we decided to use graphs, which are easier to interpret. The error bars are shown for each of the displayed parameters. For the irradiated samples, the values measured right after irradiation are marked by an arrow. For the non-irradiated excised tissue, only the first four measurements, which are in the same time frame as the irradiated tissues, are presented.

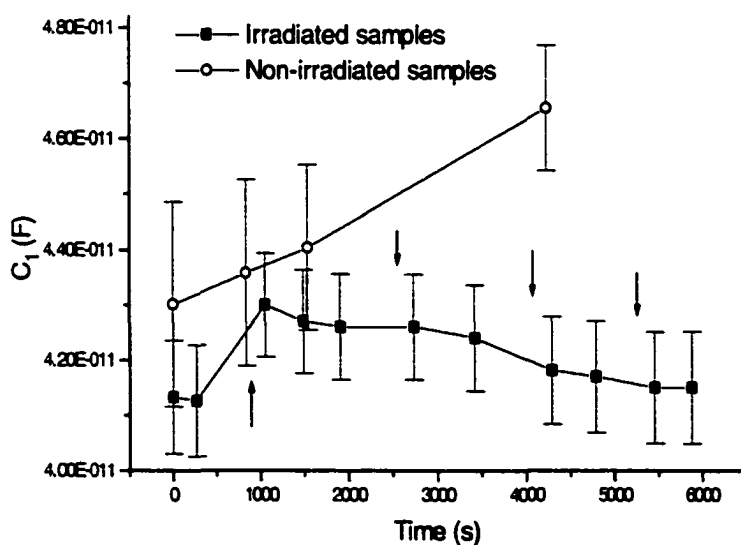


FIG. 51.  $C_1$  time dependence for non-irradiated kidney samples and irradiated samples.

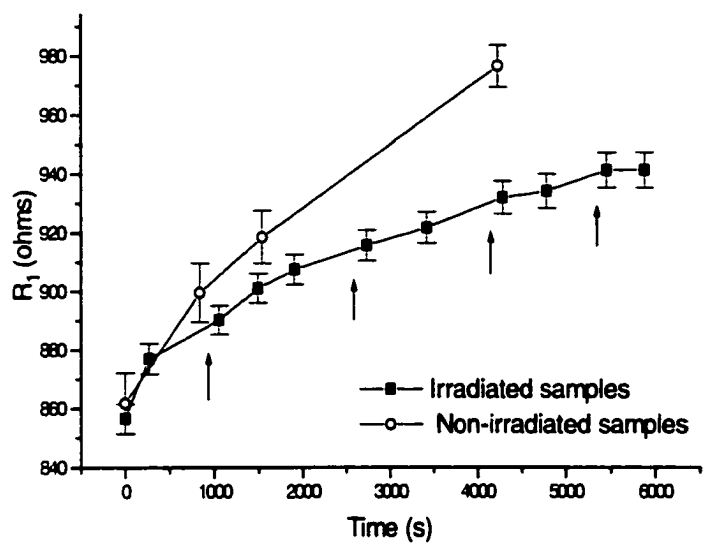


FIG. 52.  $R_1$  time dependence for non-irradiated and irradiated kidney samples.

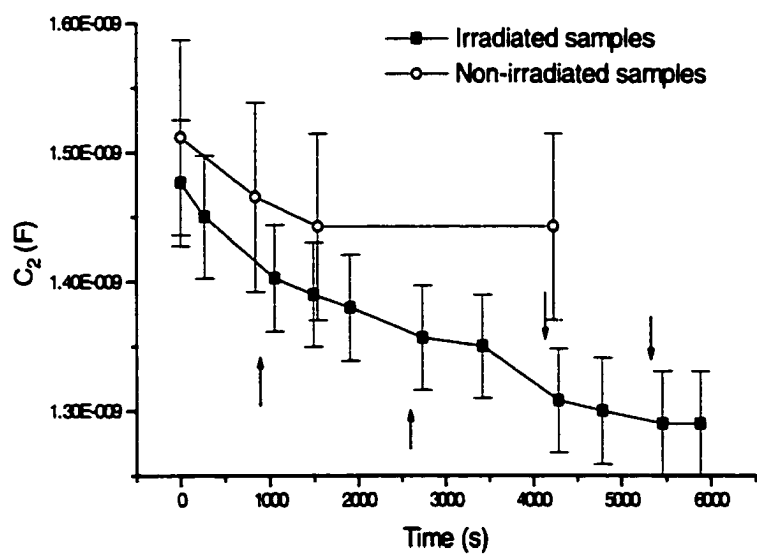


FIG. 53.  $C_2$  time dependence for non-irradiated samples and irradiated kidney samples.

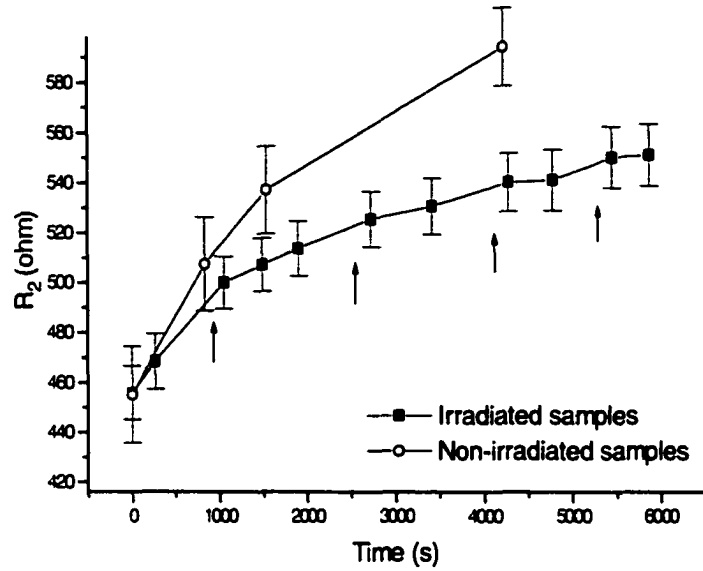


FIG. 54.  $R_2$  time dependence for non-irradiated kidney samples and irradiated samples.

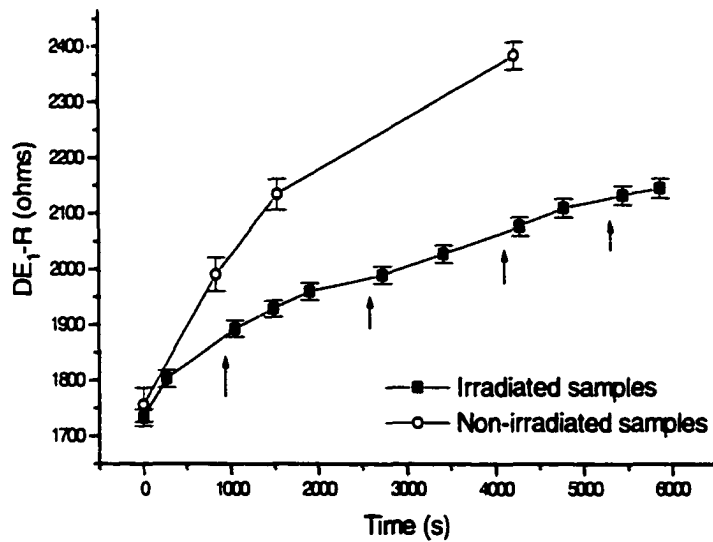


FIG. 55. DE-R Time dependence for non-irradiated and irradiated kidney samples.



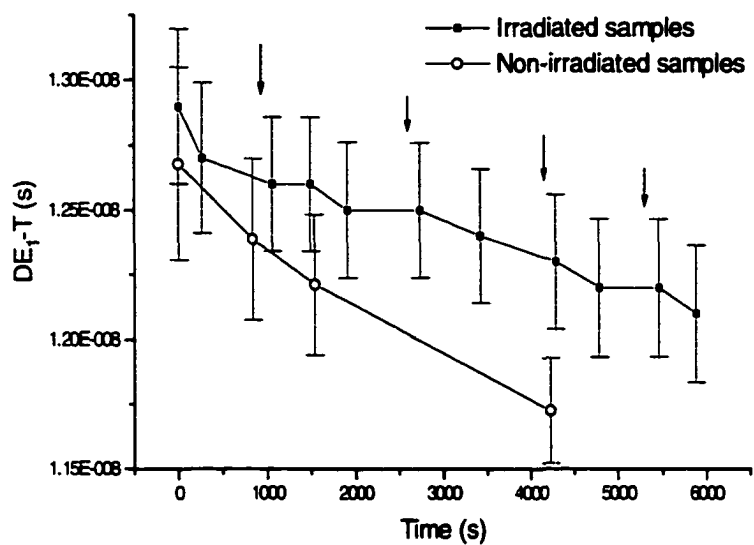


FIG. 56. DE-T time dependence for non-irradiated and irradiated kidney samples.

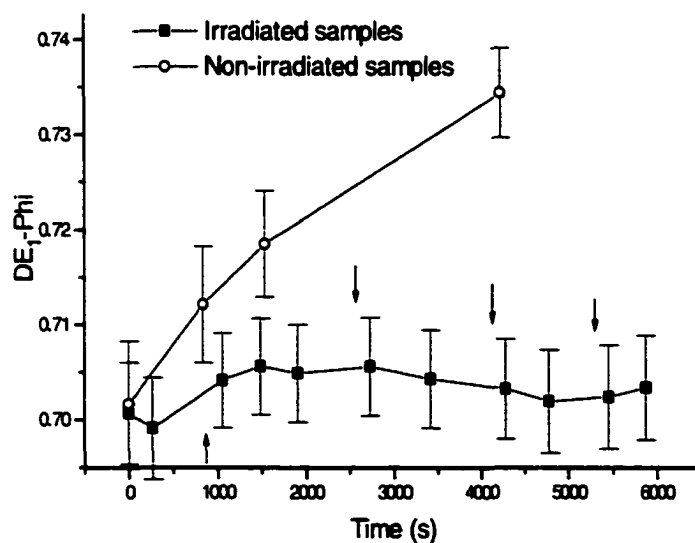


FIG. 57. Time dependence of the Phi parameter of the distributed element for non-irradiated kidney samples and irradiated samples.

Almost the rule in all these time dependencies is the fact that the values of the model parameters for the irradiated samples vary slower than for the others. The oncotic death, as explained in Chapter II, can occur simultaneously with apoptosis. The ischemia, causing oncosis, is concurrent with the apoptosis, likely induced by irradiation. The characteristics of the ischemic swelling can be recognized in the increase of  $C_1$  (as seen in Fig. 51 for the non-irradiated samples). For the irradiated sample we have an increase of  $C_1$  after the first irradiation (probably due to the initiation of lipid peroxidation, known to lead to increase of membrane capacitance), followed by a slow decrease of the membrane capacitance, consistent with the formation of apoptotic bodies. We have to remember that these measurements are on the whole tissue system, not on individual cells. Since the tissue samples were measured under the same conditions, the reduction of what was identified as oncotic swelling can be explain by the occurrence of a concurrent phenomenon, driving these parameters in the opposite direction. As discussed in the section on counterion polarization, the relaxation time, assuming the diffusion coefficient does not change, depends on the square of the radius of the particle [Eq. (54)], so the decrease of the characteristic frequency of the low frequency dispersion peak, reduced for the irradiated samples, can be accounted for the increase of the radius of the cells due to swelling. The onset of radiation induced apoptosis is characterized [15] by a reduction of plasma membrane function. The value of  $C_1$  practically stops increasing after the first dose and then exhibits a weak reduction as a function of both dose and time. It is not clear at this time whether the supplementary doses received by the tissue are at the origin of this behavior or a single dose followed by monitoring would have had the same effect. The resistance  $R_1$  associated with conduction in the extracellular space shows also smaller values for the irradiated samples. Given that the cell morphology associated with apoptosis is best described by shrinking and apparition of the apoptotic bodies, the reduction of both  $C_1$  and  $C_2$  in the irradiated samples can be explained by the apparition of a fraction of cell population characterized by lower radii and membrane depolarization. Since both tissues were measured at similar times after excision, the only explanation consistent with our findings is that we are observing, for the irradiated samples, both oncosis and apoptosis.

### Liver tissue

To demonstrate the link between radiosensitivity and impedance changes, we measured control and irradiated liver samples. Aside from its availability<sup>22</sup> the liver is very important through its multitude (it is thought their number is around 500) of metabolic and secretory functions accomplished in vertebrate organisms. The liver secretes bile, a digestive fluid, removes wastes and toxic matter from the blood, regulates blood volume, and destroys old red blood cells, metabolizes proteins, carbohydrates, and fats, stores glycogen, vitamins, and other substances, synthesizes blood-clotting factors, etc.

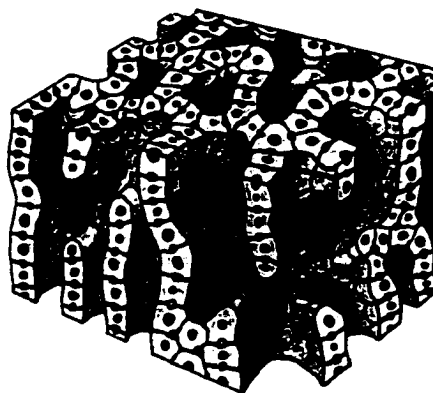


FIG. 58. Sample of liver tissue. Connective tissue and blood vessels are not shown.

Liver tissue consists of a spongy mass of cells organized in 'hepatic cell plates' (see Figure 58) tunneled through with blood vessels and bile ducts. Parenchymal cells constitute the bulk of liver tissue (about 90%) of the tissue and carry on more metabolic functions than any other group of cells in the body. A second group of cells, called Kupffer cells, line the smallest channels of the liver's vascular system and play a role in blood formation, antibody production, and ingestion of foreign particles and cellular debris.

---

<sup>22</sup> Our thanks go to Dr. Anca Dobrian from EVMS, which helped with the procurement of the rat tissue organs, and without whom little of the work presented here would have been possible.

The liver tissue is considered to have moderate sensitivity to radiation-induced damage. In the literature [70] it is known that immediately after irradiation, the morphology of the parenchymal cells is not changed, even though at microscopic inspection an accumulation of glycogen and lipids can be detected. At high doses (as opposed to the radiotherapeutic doses) necrosis occurs in the parenchymal cells, but at low and moderate doses, the changes in the cell population are small. More significant than metabolic changes induced by radiation are those due to dietary factors and hormonal regulation

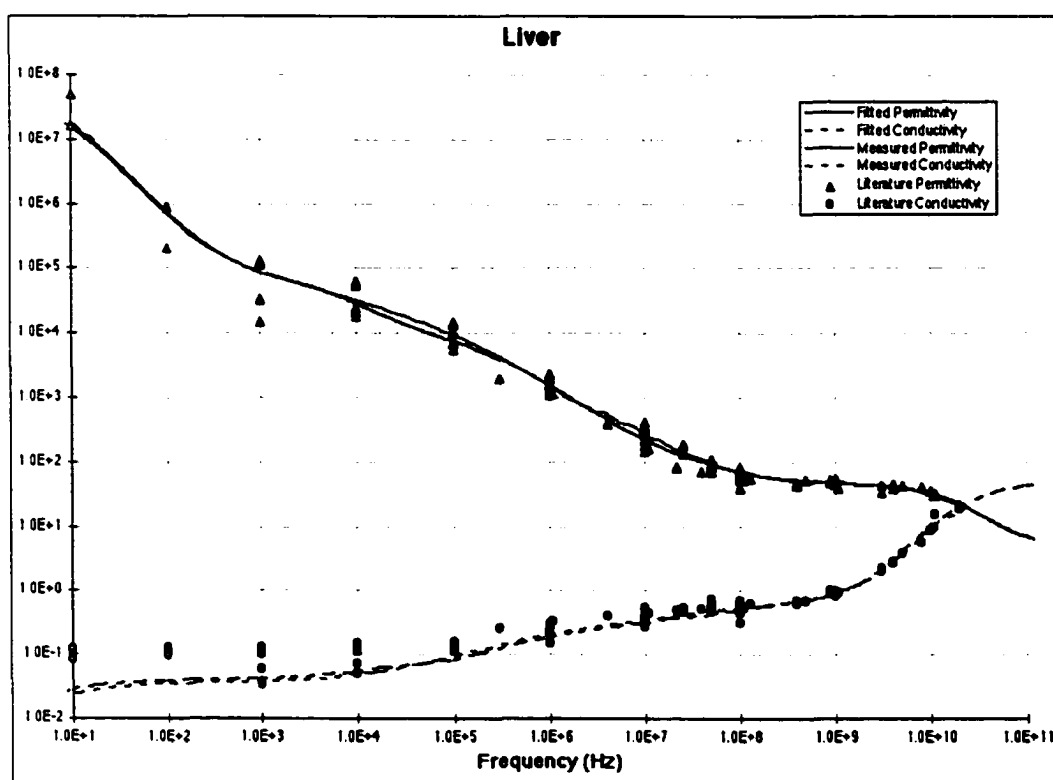


FIG. 59. Dielectric studies on liver tissue and fit [71]. The vertical logarithmic axis is common for  $\epsilon_r$  (value) and  $\sigma$  (S/m).

A common dogma is that since most normal cells in adult liver are in interphase and do not divide, when irradiated, the radiation injury becomes manifest only when the

cells are stimulated to divide<sup>23</sup>. Our results, presented in Figure 61, are consistent with reports from the literature, showing that the liver is relatively resistant to radiation injury. The literature results on liver, were gathered by Gabriel [71] and presented in Figure 59. As in the discussion on the kidney dielectric properties, we are not attempting to add another experimental point to the data existent, but to make the reader aware of the known behavior of these properties in the frequency domain we are studying.

As in the case of the kidney, we tried to alleviate the variability of the tissue by exploiting the existence of quasi-similar lobes of the liver. Thus, coming from the same animal, one lobe was used for measurements performed on non-irradiated tissue, while the other was measured after irradiation. We examined a number of 9 liver tissue organs. Temperature was kept constant at 22°C and the tissue was suspended in a Krebs solution. The same measurement protocol, used for the kidney, was repeated for the liver. We first conducted a study to detect the time dependence of impedance changes following excision without irradiation.

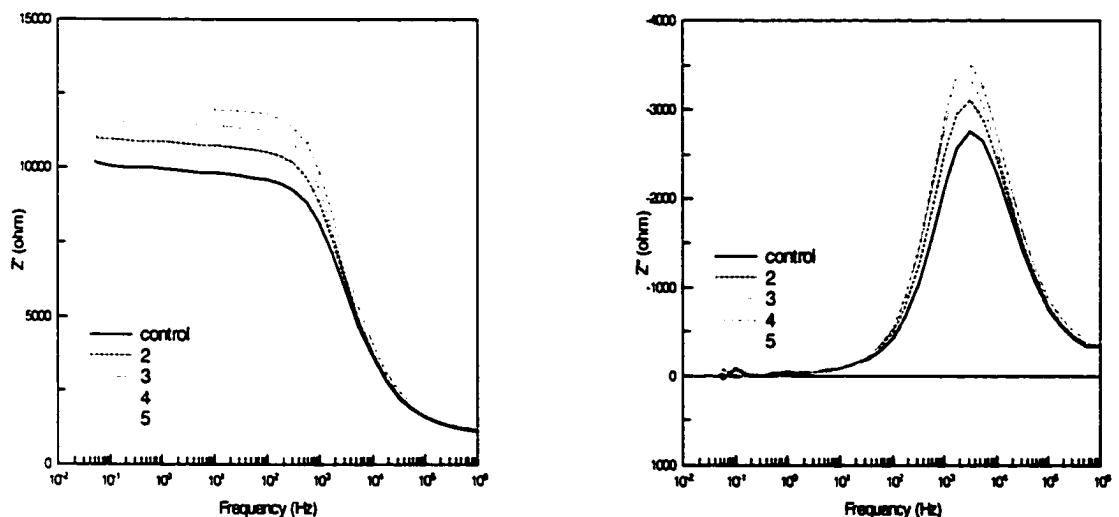


FIG. 60. Impedance spectra for fresh, non-irradiated liver: a)  $Z'(f)$  and  $Z''(f)$ ; b)  $Z'' = Z''$  ( $Z$ ). The time for the 5 measurements shown is: 0, 917, 1826, 12273, 13047 s.

<sup>23</sup> Extensive regeneration of the liver can occur when part of the organ is destroyed. For example, after the excision of 2/3 of the liver, the remaining parenchymal cells begin to divide 24-36 h later and the organ can be restored in 2-3 weeks.

The results are shown in Fig. 60. The pair lobe was then irradiated and measurements were done to control the state of the tissue before irradiation, as well as before and after each dose.

If one samples the real part of impedance  $Z' = \text{Re}(Z)$  in time, at a fixed frequency ( $f = 1 \text{ Hz}$ ), the following time dependence is suggested by the data:

$$Z' = Z_0' + A(1 - e^{-t/\tau}), \quad (91)$$

with  $Z_0' = 9800 \ \Omega$ ,  $A = 2300 \ \Omega$  and  $\tau = 1750 \text{ s}$ . Since the 'time constant' of this 'relaxation' process occurring in the tissue right after excision, is about 30 min, great care has to be taken in the data analysis, in order to remove any such trend, if present. In many of our experiments, the irradiation occurred a few hours after excision, during which the tissue was preserved in a Krebs buffer fluid, refrigerated at about 4-5°C.

The changes reported for freshly excised tissue (both liver and kidney) are consistent with data from the literature [72]: changes are pronounced in the low-frequency domain and  $\beta$  dispersion progressively declines hours after excision; shortly after excision a marked decrease in the conductivity was reported in several tissues (associated with the swelling of the cells due to ischemia) and over longer periods an increase in the conductivity was observed (explained by membrane breakdown). Surowiec [77] reports on measurements in the domain 20 kHz-100 MHz on liver and kidney. For liver, the relative permittivity does not change within the first 10 h following death. The relaxation time, relatively long for kidney compared with liver, decreases with time.

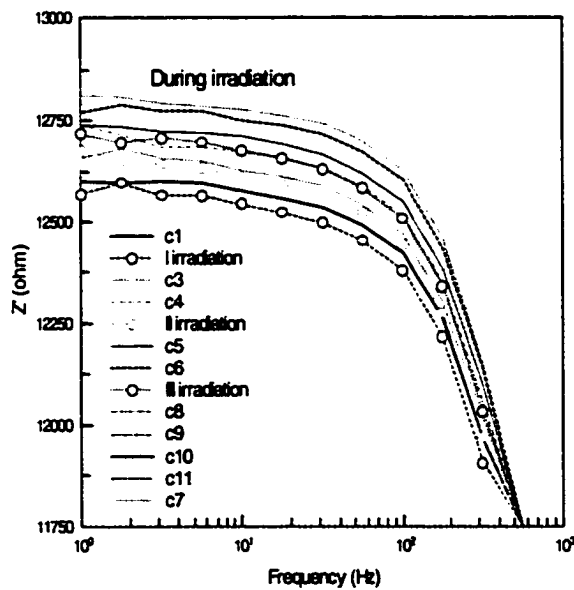
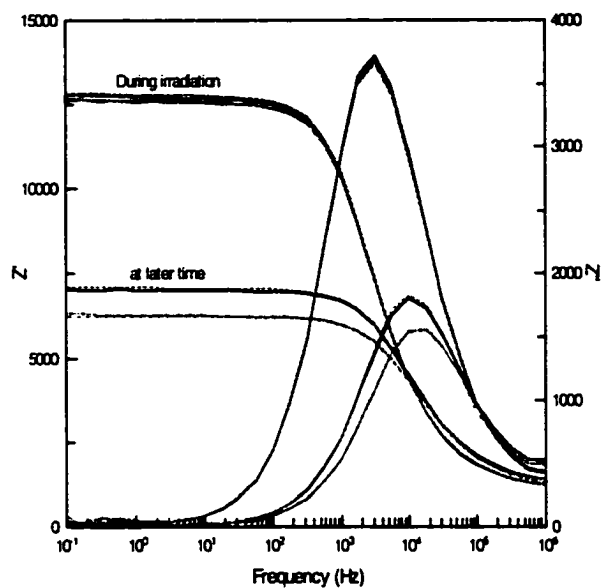


FIG. 61. Impedance spectra for irradiated liver samples. The last four are two sets of two measurements taken 18 h and respectively 23 h later. In b) a zoom of  $Z' = Z'(f)$  is shown to point out the small immediate radiation induced changes in impedance. The time of the 12 measurements is: 0, 973, 1524, 2137, 3390, 3924, 4420, 5555, 57600, 58320, 82800 and 84180 s.

The impedance spectra obtained after three irradiations, with controls taken before and after irradiations, are shown in Figure 61. After three doses of radiation (each 11.1 Gy), no impedance changes were observed immediately after each irradiation. Later changes were also assessed but due to the greater sensitivity of the liver to the lack of tissue perfusion respectively conclusions as to whether these are radiation-induced changes will be avoided. There are numerous dielectric studies of the liver, one of the most recent by Raicu *et al.* [76] in which a two shell model is used for the cell, nucleus and mitochondria measured in a frequency domain corresponding to the  $\beta$  dispersion.

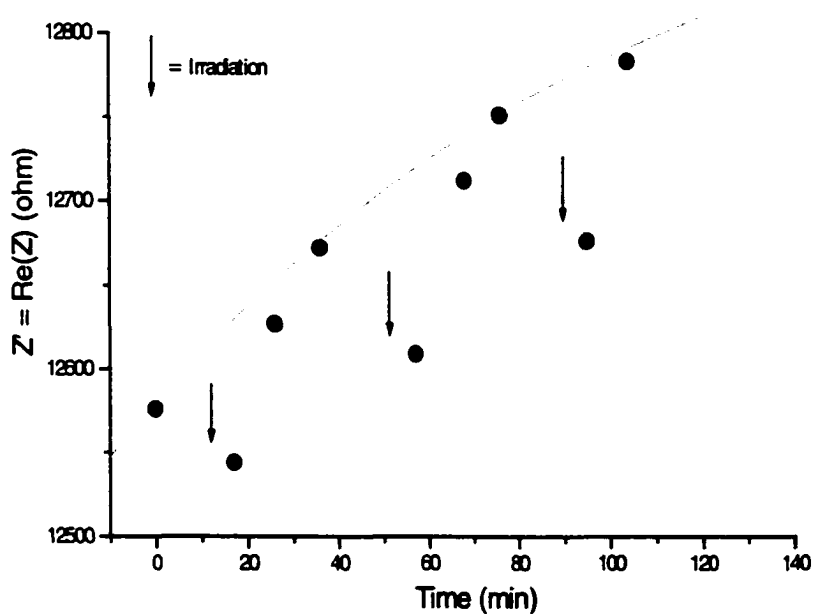


FIG. 62. Magnitude variation of  $Z' = \text{Re}(Z)$  during irradiation. The time of irradiation is shown with an arrow. The continuous curve shows the most probable variation of  $Z'$  without irradiation.

It is interesting to observe that even though the magnitude of the changes in the real part of the impedance at low frequency ( $f = 10$  Hz), are small, there is an remarkable



temporal pattern associated with decreases right after the irradiation with 999 MU (Monitor Units, about 11 Gy) followed by a 'recovery' sequence (see Fig. 62). This feature is also observed at other low frequencies and is preserved by the data set reconstructed in the extended frequency domain using the fitted parameters of the model. For fitting the data presented in Figure 61 we chose an equivalent circuit capable of mimicking the response of the system in the frequency domain investigated. At low frequency diffusion is expected to occur and given the fractality of the liver structure we used a Generalized Finite Warburg element (GFW). This is in fact the generalization or the extension of another more common element, the Finite-Length Warburg (FLW). The FLW is the solution of the one-dimensional diffusion equation of a particle, which is completely analogous to wave transmission in a finite-length RC transmission line. In the diffusion interpretation  $Ws-T = L^2/D$ , with  $L$  being the effective diffusion thickness, and  $D$  the effective diffusion coefficient of the particle). The difference, from a formal point of view, is the continuously varying exponent  $Ws-Phi$  ( $0 < Ws-Phi < 1$ ) instead of the fixed value  $Ws-Phi = 0.5$  for the FLW. The impedance  $Z$  of this element is described by the equation:

$$Z(\omega) = R \frac{\tanh(i\omega T)^{Phi}}{(i\omega T)^{Phi}} \quad (92)$$

where  $R$ ,  $T$  and  $Phi$  are the fit parameters of the element:  $Ws-R$ ,  $Ws-T$  and  $Ws-Phi$ . At very low frequencies,  $Z'$  approaches  $Ws-R$  and  $Z''$  goes to zero.

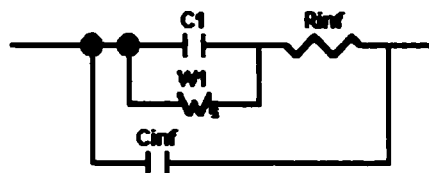


FIG. 63. Equivalent circuit for fitting the liver data.

The following graphs represent the time evolution of the model parameters for both irradiated and non-irradiated samples. The horizontal axis 'Index' refers to the chronological order, so is in fact a time axis. The last two measurements, for the non-irradiated samples and the last four for the irradiated ones are taken at much longer times,

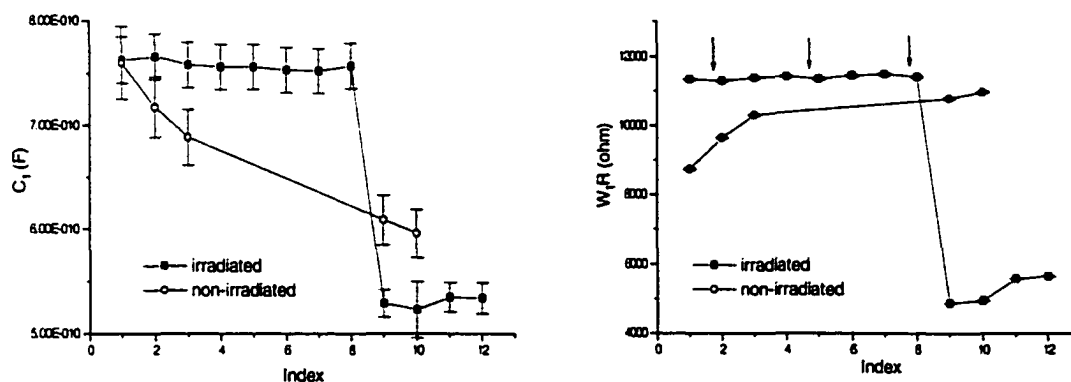


FIG. 64. Representation of the  $C_1$  and  $W_s-R$  parameters of the model. The index order is identical with that of the data presented in FIG. 61 and the data recorded immediately after irradiation is marked with an arrow.

and therefore their position in time is not proportional with their index. However, since a logarithmic representation would not have been suitable and a broken axis too cumbersome to reproduce in all the graphs, we decided to represent only their chronological order. Equal doses of 11.1 Gy were delivered just before measurements number two, five and eight (the arrows in Figure 64)

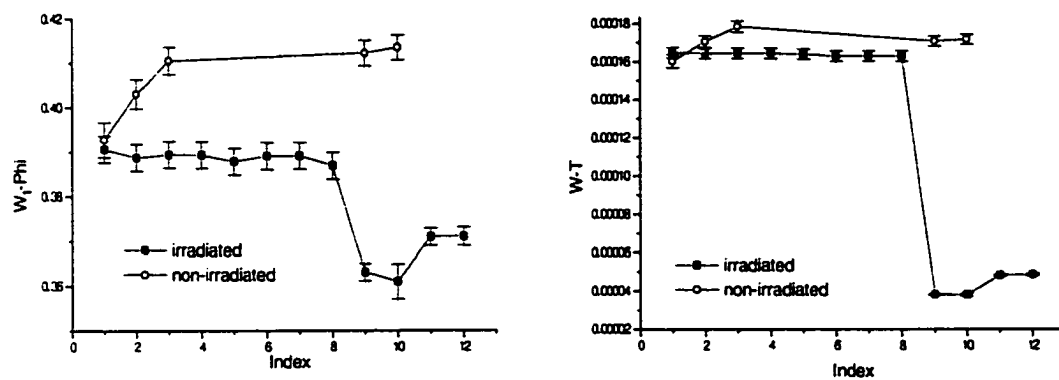


FIG. 65. Representation of the  $W_s-P$  and  $W_s-T$  parameters of the model. The index order is identical with that of the data presented in FIG. 61

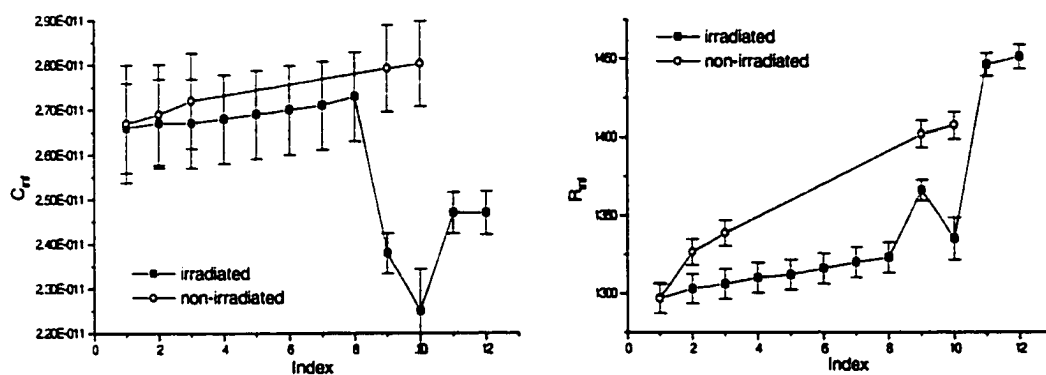


FIG. 66. Representation of the  $C_{inf}$  and  $R_{inf}$  parameters of the model. The index order is identical with that of the data presented in Figure 61.

The graphs of  $C_1$  and  $W-R$ , in Figure 64, representing the capacitance and membrane resistance, showed very little change during the irradiation session. Compared with the time evolution of the same parameters for the excised tissue samples, we notice an

increase of the capacitance, as well as a decrease of the membrane conductivity. As Bonincontro [78] and others have shown, the apoptotic death induced by free radical attack is correlated by a decrease of membrane conductivity, suggesting that one of the early events in the triggering of the apoptosis is an overall reduction of plasma membrane function. It is interesting to point out that even though the plasma membrane involvement in the events leading to mutagenesis or DNA repair, is not fully understood, recent studies [79] showed that membrane potassium  $K^+$  currents, activated by ionizing radiation, play a significant role in mutagenesis. The kinetics of the current induction is very rapid, occurring in few minutes after irradiation, with a relaxation time on the order of minutes. The mechanism of  $K^+$  current activation was proven to be due to free radicals [80].

In [81] a study of ischemia induced disturbances in rat liver was conducted using electrical impedance measurements. Their model emphasized three elements: the extracellular resistance  $R_e$ , the intracellular resistance  $R_i$  and the cell membrane capacitance  $C_m$ . The  $R_e$  value increased rapidly after excision (reaching a peak after 13 min at 36 °C), then decreases slowly, becoming constant after about 3 hours. The  $R_i$  decreased in an early stage, followed by no change and increase after approximately 4 hours. The  $C_m$  showed a similar pattern with  $R_e$ . The increase in  $R_e$  was probably due to an decrease of the volume of the extracellular fluid, a consequence of cell swelling and the onset of oncosis, which also explains the increase of  $C_m$ . The timing in the decrease of  $C_m$  is correlated with the increase in  $R_i$ , in a similar manner in which  $C_1$  is correlated with  $W-R$ , showing that cell lysis proceeds and that the flow of extracellular fluid into the cell begins at this time.

To conclude the section on liver tissue, we can state that little change in impedance occurred as result of irradiation. All parameters of the model reflect this trend for the first 8 measurements. Caution have to be exerted in the interpretation of the last four measurements because they reflect changes occurring in the tissue at very long times compared with those related to the monitoring *during* the irradiation session. Their importance is to provide a baseline for what supposedly represents necrosis and to allow a visual interpolation of the model parameters for the non-irradiated tissue at longer times.

### Lung tissue

Lungs are sponge-like structures containing about 300 million alveoli. With a surface of about  $80 \text{ m}^2$ , only about 10% of the lung is occupied by solid tissue, whereas the remainder is filled with air and blood. Anatomically, most of the alveolar wall is comprised of the capillary. Epithelial cells normally cover the entire surface of the alveolus. There are 2 basic types of cells: Type I (Membranous) and Type II (Granular) pneumocytes. The first ones cover about 95% of the surface area of the alveolar wall. Type I cells cannot regenerate and, when injured, fluid exudates and collects in airspaces. The granular pneumocytes cover about 3% of the alveolar surface but account for 60% of the epithelial cells, and are capable of regeneration and replacement of type I cells after injury.

The structure of lungs (bronchioles trees) can be modeled as a fat fractal [82] obtained by ballistic aggregation clustering. Fat fractals are not self-similar structures! When the volume of a fat fractal structure enclosed in a sphere of radius  $r$  is calculated, it follows a power law with an exponent that can be regarded as a quantity characterizing the scaling properties of the structure:

$$V(l) \propto V(0) + Ar^\beta, \quad (93)$$

where  $A$  is a constant and  $\beta$  the exponent quantifying the fractal properties.

Fractality is precisely the reason for which, from a dielectric point of view, the lung is among the few tissues exhibiting only Constant Phase Angle (CPA)-type dispersions [83]. Dissado [39] pointed out that CPA elements are likely to reflect hierarchically organized structures. Models leading to CPA elements are infinite networks of resistors and capacitors or charge transport in disordered systems.

The CPA frequency dependence is given by [83]:

$$\epsilon = \epsilon_\infty + \frac{\epsilon_0 - \epsilon_\infty}{2} \tau^{1-\beta} (i\omega)^{\beta-1} - i \frac{\sigma_\tau}{\omega}, \quad (94)$$

where  $\beta$  (with values between 0 and 1) is a parameter depending upon the specific relaxation mechanism involved and  $\tau$  is the characteristic relaxation time.

As far as radiation induced effects are concerned, two are well known: radiation pneumonitis and lung fibrosis. The first signs of early lung changes are seen almost immediately after irradiation. The reaction peaks after 5 to 6 months, then settles partially before 9-10 months. After about 9-10 months, the late changes become manifest and these are stable in most cases. A response begins almost immediately after the onset of acute lung injury in an attempt to repair the damage done to the alveolar wall. Inflammatory cell accumulation and the entry of plasma into the airspaces alter the alveolar microenvironment.

The radiation-induced effects on lung tissue were studied on 7 pairs of lungs, harvested from healthy rats used in another experiments at EVMS. After excision, the tissue was kept on dry ice temperatures, suspended in Krebs buffer. During the irradiation, the lung samples were given 3 doses of 5.3 Gy, 6 MV photon beam. The effect of the excision on non-irradiated samples was studied but we had problems comparing different samples between them. The lungs, even for small animals were larger than the sample holder, so we had to cut smaller pieces. Whether it was the cut through the lung lobe or simply the fractal behavior of the lung structure, it is still an open problem, but even for samples obtained from the same lung, we had problems normalizing the impedance measurements. These problems occurred only for lung and this is the reason for which results are only presented for irradiated lung tissue. A large number of controls were taken during the irradiation session, trying to compensate for the lack of the excision study.

The dielectric data gathered from literature is shown in Figure 67, below and a table with the values of permittivity and conductivity for the frequency domain of interest for us is presented in Appendix B. It is interesting to notice that even though there are no experimental data reported at frequencies less than 10 kHz, the crude Cole-Cole model used to model the data shows a low frequency dispersion, well evidenced in our study.

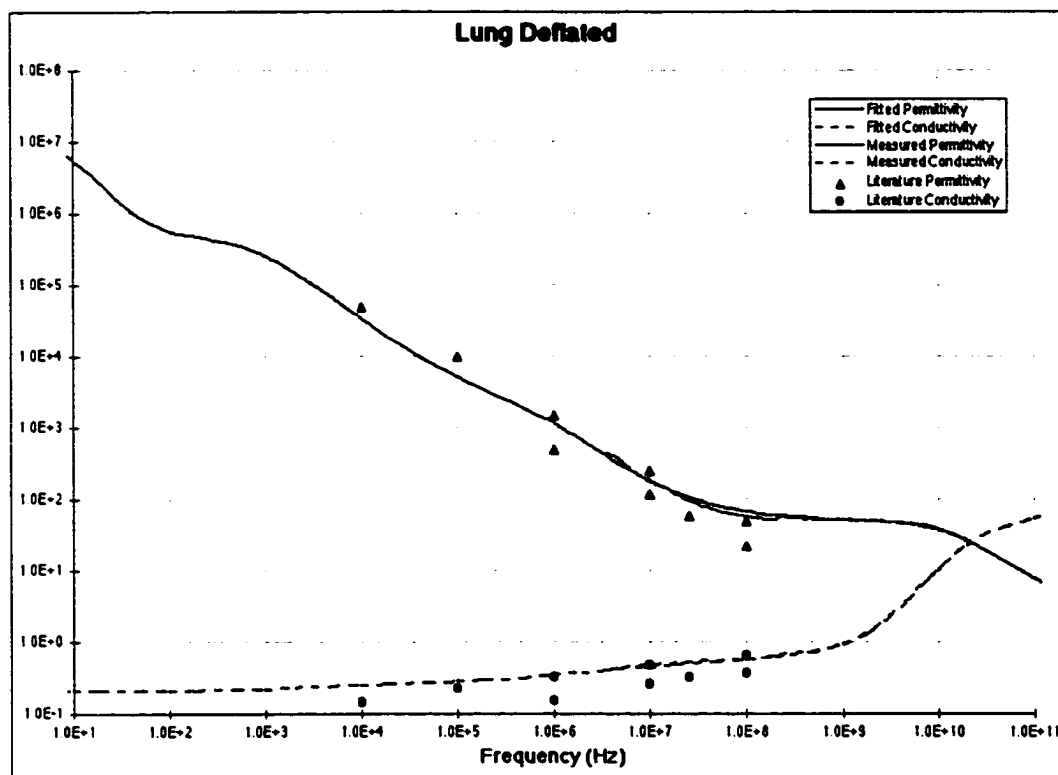


FIG. 67. Dielectric data on lung tissue gathered from literature [71].

In Fig. 68 and 69 are presented our primary results obtained on lung tissue. Eleven sets of measurements were carried out to monitor the response of the tissue during the irradiation session. The legend refers to c1-c11 as control measurements before or after irradiation, while the measurements taken immediately after the three irradiations - three equal doses, each of 5.3 Gy, photon beam of 6 MV - are labeled with the roman numbers I, II and III. After the irradiation session, the tissue was kept in the same conditions and monitored for another 24 h to assess any changes occurring as a result of the irradiation. All measurements were carried out at constant temperature  $T = 20.3\text{ }^{\circ}\text{C}$ , with a four Pt electrode configuration, in a constant potential mode ( $V = 10\text{ mV}$ ) with balancing of the source after each measurement. In Fig. 68 are presented the three measurements made at later times, together with the three measurements taken after each radiation dose was received. The legend is self-explanatory.

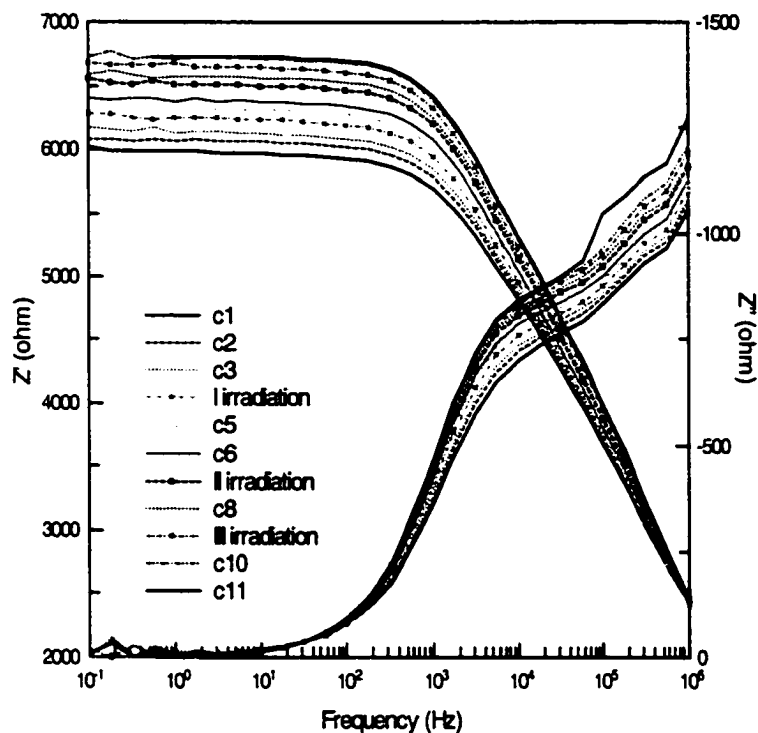


FIG. 68. Impedance measurements on lung tissue. All measurement are shown

The real part of impedance,  $Z'$ , displays a steady increase during the irradiation session. For easier identification, the measurements taken right after irradiation are shown with a dotted line. In the frequency dependence of  $Z''$  we can guess the existence of a second, broad dispersion at larger frequencies, not entirely covered by our measurements. The model utilized allowed us not only to perfectly fit the response in the domain from 50 mHz to 1 MHz, but to completely identify this second dispersion by extending the frequency domain up to 100 MHz. In Figure 69 is shown the impedance response immediately after irradiation, together with three other measurements taken more than 10 hours later.



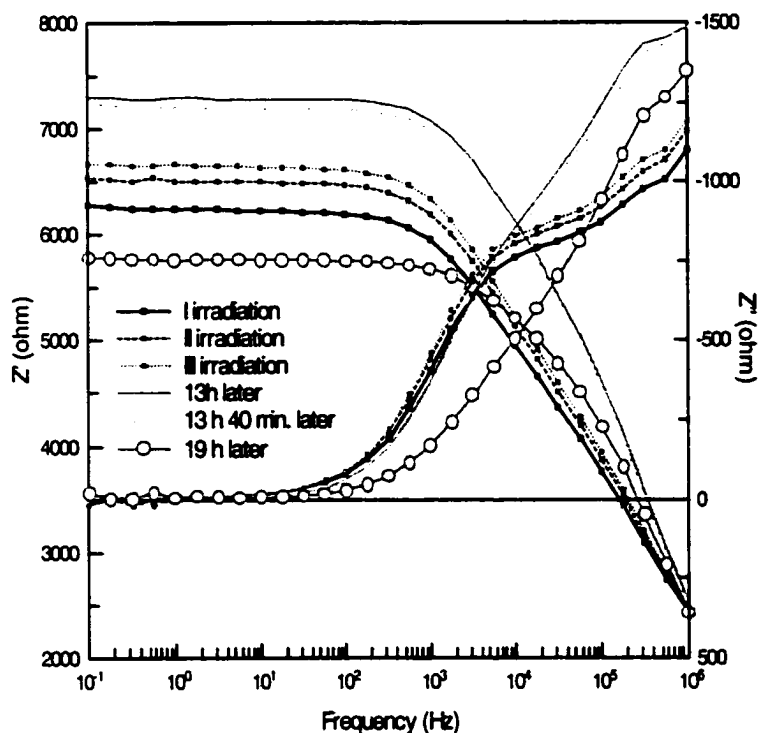


FIG. 69. Impedance measurements on lung tissue. Data sets taken during the irradiation session are shown for comparison with the three later measurements.

For reasons already discussed, related to the fractality of the lung structure, the impedance data for this tissue was fit with an equivalent circuit containing two CPA elements, each modeling one of the two dispersions that can be guessed in the impedance spectra:

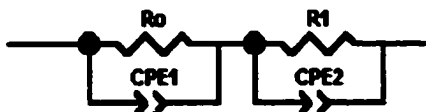


FIG. 70. Equivalent circuit used for fitting the lung data

The frequency dependence of a Constant Phase Element (CPE) is given by:

$$Z(\omega) = \frac{1}{T(i\omega)^P}, \quad (95)$$

where  $T$  and  $P$  are the parameters of the CPE. If  $P$  equals 1 then the equation is identical to that of a capacitor (a capacitor is, in fact, a constant phase element - one with a constant phase angle of 90 degrees). If  $P$  equals 0.5, a 45° degree line is produced on the Complex-Plane graph. When a CPE is placed in parallel to a resistor, a Cole-Element (depressed semi-circle) is produced. Often a CPE is used in a model in place of a capacitor to compensate for non-homogeneity in the system. For example, a rough or porous surface can cause a double-layer capacitance to appear as a constant phase element with a  $P$  value between 0.9 and 1. A CPE with a  $P$  value of 0.5 can be used to produce an Infinite Length Warburg element. A Warburg element occurs when charge carriers diffuse through a material. Lower frequencies correspond to diffusion deeper into the material. If the material is thin, low frequencies will penetrate the entire thickness, creating a Finite Length Warburg element. If the material is thick enough so that the lowest frequencies applied do not fully penetrate the layer, it must be interpreted as infinite.

To check how well the equivalent circuit describes the response of the real system, we performed a fit for the parameters of the circuit, using the data set c1. The non-linear fit is simultaneously done on both the real and imaginary part of  $Z$ , and the data is weighted, as suggested by MacDonald [84] by normalizing each point to its magnitude.

The results of the fitting procedure are shown in Fig. 71; the frequency domain for the fit curve being has been extended down to 1 mHz and up to 100 MHz, in order to check if the circuit response is physically meaningful (if a dispersion-like response occurs, if  $Z'$  becomes constant at very low frequencies and  $Z''$  tends to zero).

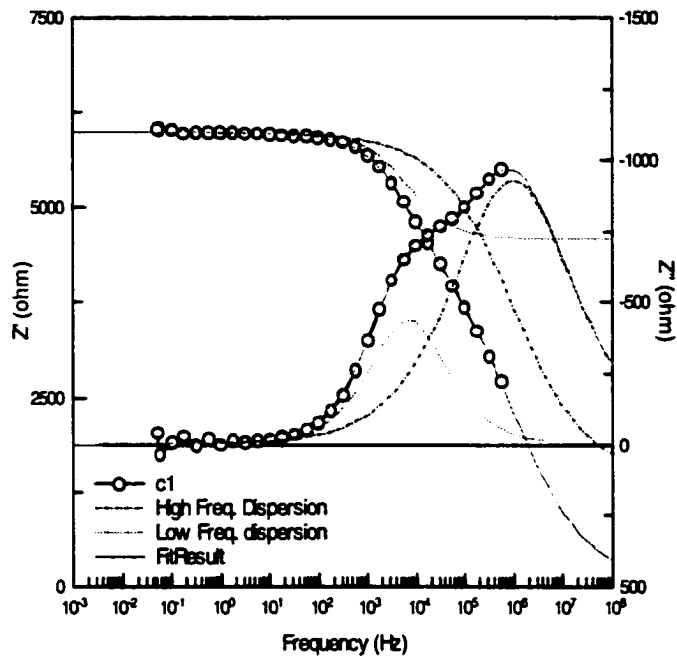


FIG. 71. Data and fitted impedance spectrum for c1 data set. The contribution of the two CPE elements (at low and high frequency) is shown separately.

Two dispersions are clearly evidenced by the analysis shown in Fig. 71, centered at  $f = 6.7$  kHz for the low frequency dispersion and  $f = 1047.1$  kHz, the high frequency one. The parameters  $P$  of the two CPEs are 0.71 and 0.49, respectively, showing a broader low frequency dispersion. The high frequency dispersion peak can be assigned to an interfacial Maxwell-Wagner mechanism. The low frequency cannot be attributed *a priori* to a single tissue component or single process occurring in the tissue, but taking the frequency as criteria, it is definitely involving the  $\alpha$  dispersion mechanisms.

The next step in our analysis was to decompose and plot the two dispersions for the first four measurements, including the response after the first radiation dose.

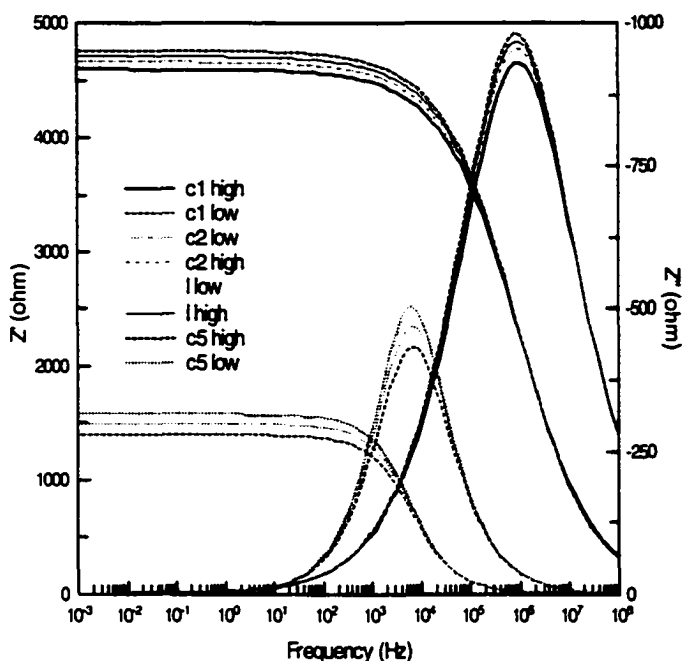


FIG. 72. The evolution of the two dispersion peaks during the first 4 measurements.

Both the  $\alpha$  and  $\beta$  dispersion peaks seems to increase in magnitude before the first irradiation. Curiously enough, it is only the low frequency response, which seems to be *stopped* from increasing, in both  $Z'$  and  $Z''$  coordinates. No changes in the characteristic frequency can be detected at this stage.

The same type of analysis and graphical presentation was completed for all samples and all determinations. We found relevant the plot of the first irradiation and its controls, before and after irradiation, together with measurements of the lung samples at longer time s after the irradiation (13 to 19 hours), shown in Fig. 73. For the low frequency dispersion,  $Z'$  increases at smaller and smaller rates during the irradiation, without a change of the characteristic frequency. After 13 hours, drops to values smaller than the initial control, just to reach, 6 hours later an increased value and a ten fold increase of the characteristic frequency.

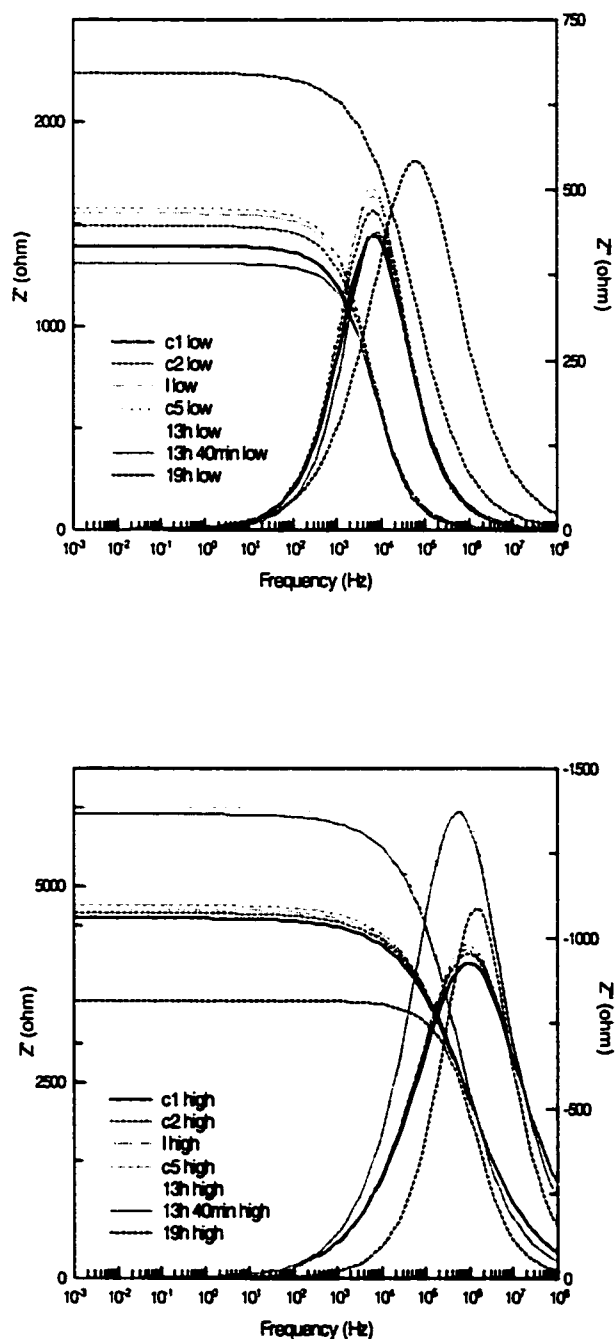


FIG. 73. Evolution of the two CPE dispersions after the irradiation. In a) are shown both  $Z'$  and  $Z''$  frequency dependence of the low frequency dispersion; b) similar plots for the high frequency dispersion.

The high frequency behavior is a bit different at longer times. During the irradiation session, no frequency change and only slight changes occurred in the magnitude of  $Z'$ . After 13 h,  $Z'$  is increasing noticeable, to drop after other six hours to values smaller than the initial control c1. The initial increase in  $Z'$  seems associated with a decrease of the peak frequency (from 1047 kHz to 560 kHz), while the final drop is associated with an increase from 1047 kHz to 1350 kHz.

Continuing the data analysis, the whole batch of data acquired during and after irradiation of samples, was fitted with the equivalent circuit from Fig. 70. The parameter values are presented graphically in Fig. 74-76. The index in the figures refers to the chronological order in which the data sets were acquired, with the last 3 taken at longer times after the irradiation. The data sets acquired right after the irradiations are marked with an arrow.

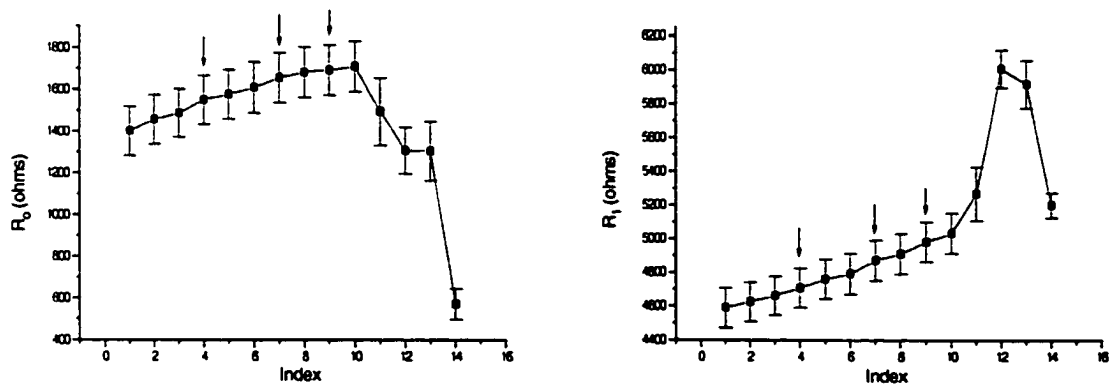


FIG. 74. Comparative evolutions of  $R_0$  and  $R_1$  of the equivalent circuit modeling the impedance response of lung tissue to radiation injury

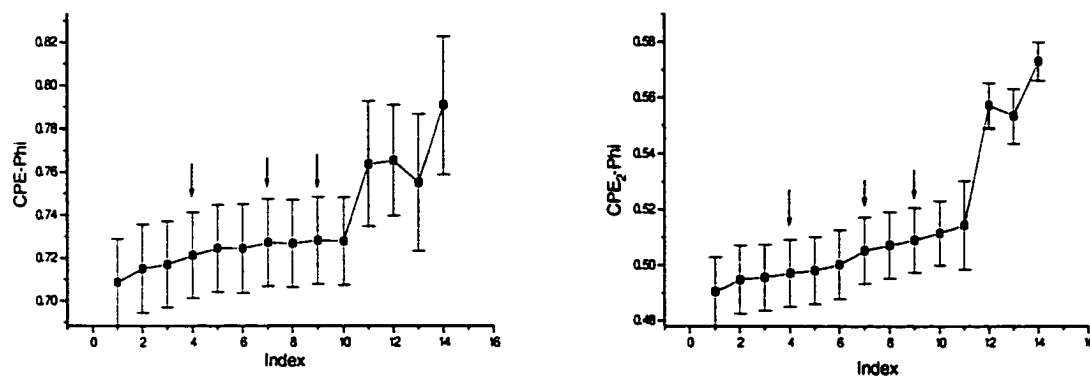


FIG. 75. Comparative evolutions of CPE-Phi elements of the equivalent circuit modeling the impedance response of lung tissue to radiation injury

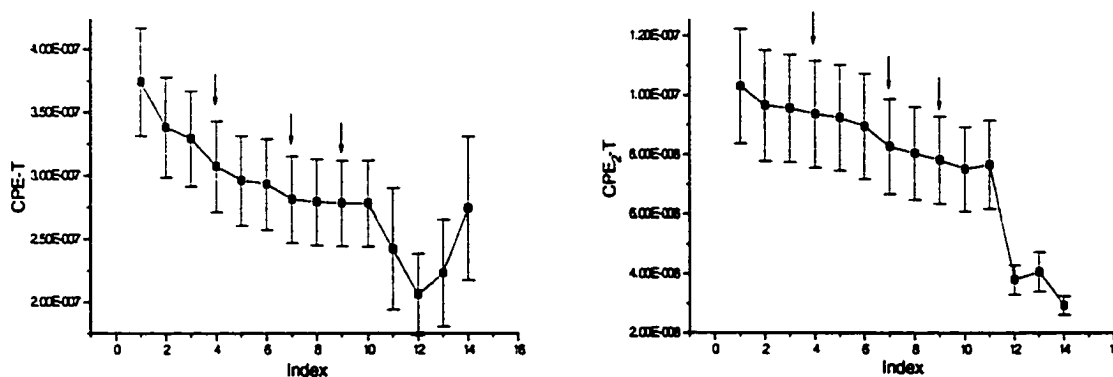


FIG. 76. Comparative evolutions of CPE-T elements of the equivalent circuit modeling the impedance response of lung tissue to radiation injury

As we already mentioned, the lung, more than other tissue specimens, shows a very powerful fractal character. Because of its relatively large size, we had to use smaller pieces than an integral lobe. The problem we encountered was that fact the for different tissue sizes, we obtained different conductivities and consequently, different impedances.

It is known that some of the fractal properties (conductivity included) scales with the size, which we think was the major problem in dealing with and comparing among samples of different sizes.

Interpreting the model parameters shown above is not easy. The high frequency dispersion can be in a straightforward manner related to the membrane resistance and capacitance. The decrease of the membrane conductivity (and implicitly its resistivity increase) is a known sign of apoptotic death [15]. At the end of this process, necrosis is marked by a sudden  $R_1$  decrease, signaling a membrane breakdown, at least of the cell fraction undergoing oncosis. Those two pathways, as described in Chapter II, cannot occur totally separated, and even though in radiation-induced effects we are mainly interested in apoptosis, our data on excised tissue shows that inflammatory death is part of the process. The formation of apoptotic bodies (smaller volumes than the initial cells) and swelling are probably the cause of the increased Phi parameter at large times, signifying a slight reduction of cell size distribution. The T parameter can be interpreted as an average time constant, which implicitly can be related to a membrane capacitance. The decrease of T in time during the irradiation session, as well as the drop at late times after irradiation can also be related to a reduction of membrane function.

The low frequency dispersion is not that straightforward in interpretation. In its discussion on radiation late effects on lungs, Alpen [9] points out that "pneumonitis is the result of altered characteristics of the alveolar surface with accompanying changes in fluid and gas transport across the alveolar subunit". On the other hand, we know that the  $\alpha$  dispersion occurs in connection with surface conductivity and counterion relaxation effects. The only drawback in matching the two concepts is the fact the pneumonitis is a late effect (onset time from three to six months), while our observations are at very early times after the irradiation. We recognize this as an open problem which needs further experimental work to be settled. Only long time *in-vivo* experiments will probably be able to validate a relation between the early changes we reported on the low frequency dispersion on lung tissue and the possible onset of pneumonitis.



## **Heart tissue**

The heart is a special muscle, fundamentally different from the skeletal muscles. Even though there is no special interest in irradiating the heart (except maybe as a concern in breast irradiation), we decided to analyze the radiation induced effects and their reflection in the dielectric properties, knowing that these properties are affected in some degree by the extracellular ions. The contractility of the heart is triggered by an action potential. This is a complex electrical event that involves the movement of ions across cell membranes which changes the concentrations of ions within and outside the cells, so the permeability of the membrane plays an important role. Since one of our working hypotheses is that the membrane itself is a target for radiation-induced changes, we decided to experiment with the heart tissue. Structurally, the walls of the heart consists of three distinct layers--the epicardium (outer layer), the myocardium (middle layer), and the endocardium (inner layer). It is the myocardial layer that causes the heart to contract; the bundles of muscle fibers are so arranged as to result in a wringing type of movement that efficiently squeezes blood from the heart with each beat. Coronary vessels supplying arterial blood to the heart penetrate the epicardium before entering the myocardium. This outer layer, or visceral pericardium, consists of a surface of flattened epithelial (covering) cells resting upon connective tissue. The myocardium consists of interlacing bundles of cardiac muscle fibers possessing the appearance of striated muscle (striped skeletal muscle) with intermittent dark plates crossing the fibers, but these highly specialized fibers differ fundamentally from those of skeletal muscle in the arrangement of nuclei and in the smaller caliber of the individual fiber. The nuclei are oval and situated along the central axis of the fiber, which may range in size from 12 to 21 micrometers in diameter. Each fiber consists of a bundle of smaller fibers, called myofibrils, each of which passes through the full length of the fiber and is covered by an external limiting membrane known as the sarcolemma.

The individual cardiac muscle cells are striped crosswise throughout, with alternating dark bands that are opaque to light and with light bands that permit the passage of light. Prominent plates of condensed dark bands called intercalated disks, crossing the muscle fiber at uneven intervals, are perhaps the most conspicuous features

unique to cardiac muscle. This is an interesting feature, which given the muscle behavior, depending on the angle between the direction of the current and that of the fibers, will direct us toward a certain model. The parameters of the dispersion, from the Cole model, expressed in terms of impedance as  $Z = R_{\infty} + \frac{R_0 - R_{\infty}}{1 + i(f/f_c)^{1-\alpha}}$ , are summarized in the

following table [85]:

TABLE V. Cole model parameters for in vivo muscle tissue impedance measurements

Tissue	$R_0/R_{\infty}$	$f_c$ (kHz)	$\alpha$
Muscle	$3.1 \pm 0.3$	$94.9 \pm 17.5$	$0.20 \pm 0.01$
Muscle $\perp$	$3.3 \pm 0.4$	$63.6 \pm 10.6$	$0.19 \pm 0.05$
Myocardium	$1.8 \pm 0.4$	$144.2 \pm 60.2$	$0.29 \pm 0.04$

Data collected from literature [58] is summarized in the Fig. 77:

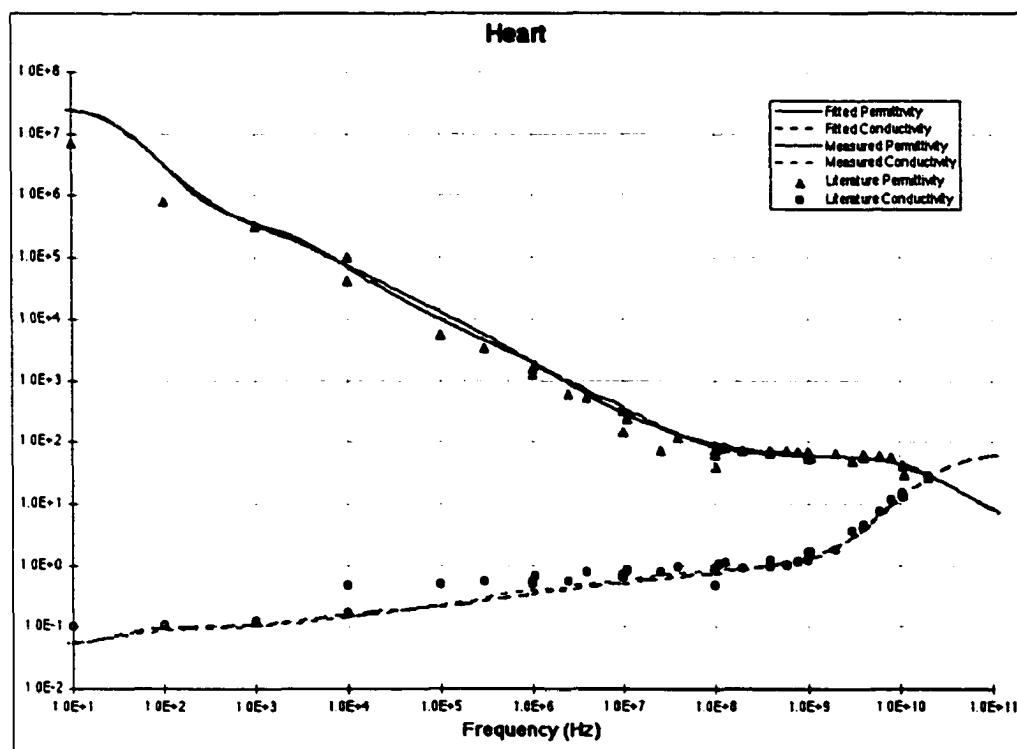


FIG. 77. Dielectric data on heart muscle, gathered from literature. On the vertical axis are represented both  $\epsilon_r$  (value) and  $\sigma$  (S/m)

We have studied a number of 6 rat heart tissue samples. Impedance measurements were conducted for both excised and non-irradiated tissue as well as for the irradiated samples. As all other tissues, right after excision, the tissue was preserved at 4-5 °C suspended in Krebs buffer. Sets of 15 measurements were carried out for the tissue samples analyzed in the next section. For irradiated tissue, four doses of 10 Gy each were administered just before measurements number 6, 9, 12 and 14. A four-electrode technique was used for all measurements, with the precautions described in the previous sections, for kidney, liver and lung tissues. The samples were analyzed in the potentiostat mode ( $V=10..25$  mV) in a frequency range from 50 mHz to 1MHz. The starting time of each frequency sweep (from high to low frequency) is  $t = 0,373, 791, 1231, 1771, 3015, 3500, 3974, 4596, 4879, 5299, 6516, 6822, 7557$  and  $7969$  s.

Results of our impedance measurements obtained on heart tissue are shown in Fig. 78.

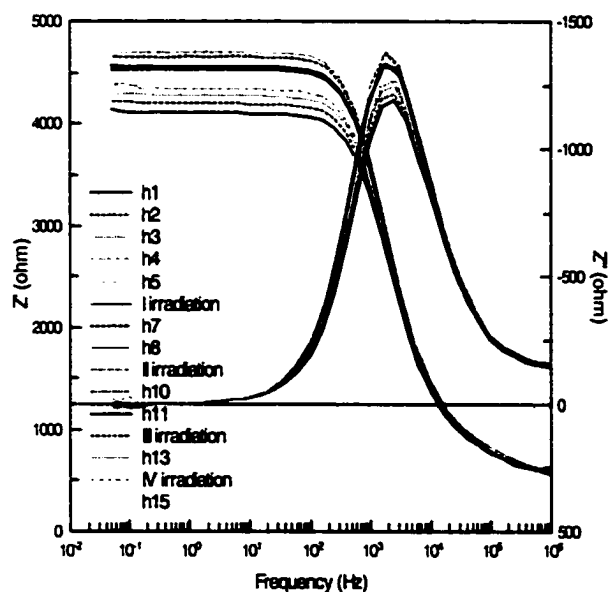


FIG. 78. a) Impedance,  $Z'$  and  $Z''$  vs. frequency plots on irradiated heart tissue.

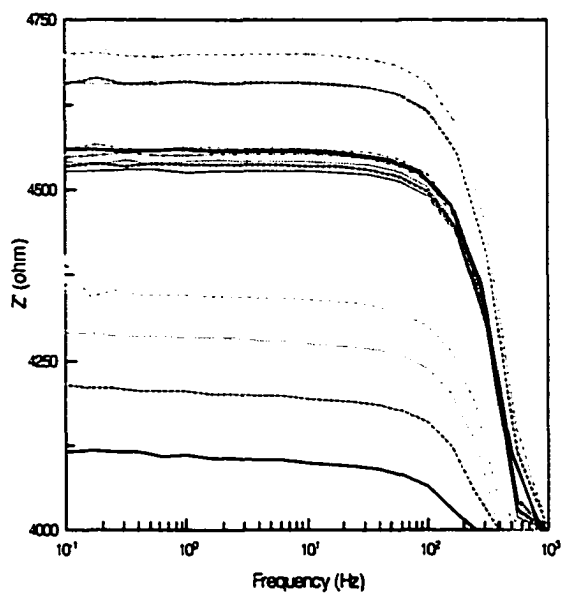


FIG. 78. Impedance,  $Z'$  and  $Z''$  vs. frequency plots on irradiated heart tissue. In b) a zoom of  $Z'$  is shown.

An elementary analysis of the complex plot, trying to identify a Cole-Cole response leads to the result shown in Figure 79. A second dispersion can be somehow guessed, but we did not go to high enough frequencies. The analyzer itself (Solartron 1260) has an upper limit of 32 MHz, but the constraint in this case was the interface (Solartron 1194) whose limit for high frequencies is only 1 MHz.

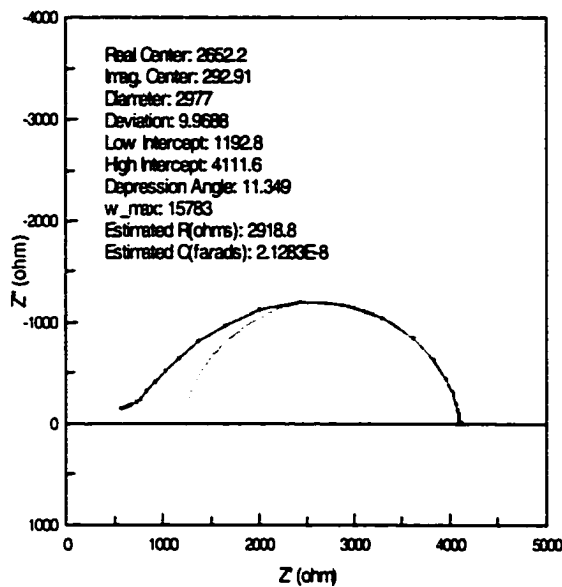


FIG. 79. Elementary analysis of the non-irradiated heart tissue impedance response. The semicircle represents the response of a simple Cole element and the deviation at high frequencies is evident.

We chose to model the impedance response with the circuit shown in Fig. 80, a series of two Warburg impedances.



FIG. 80. Equivalent circuit for heart tissue.

Myocardium has a "stringy" look compared to skeletal muscle. Skeletal muscle cells are large and lie next to each other in more or less parallel bundles. Cardiac muscle cells are small, butted together at their ends, irregularly shaped, and have numerous blood vessels between them. The effect is to create a network of fibers rather than a solid phalanx of muscle fascicles. The expected phenomenon is high frequency dispersion due to

interfacial polarization accompanied of low frequency lateral diffusion of counter-ions surrounding the membranes. The impedance  $Z$  of this element is described by:

$$Z(\omega) = R \frac{\tanh(i\omega T)^P}{(i\omega T)^P}, \quad (96)$$

where  $R$ ,  $T$  and  $P$  are the fit parameters of the element:  $W_s$ -R,  $W_s$ -T and  $W_s$ -P. At very low frequencies,  $Z'$  approaches  $W_s$ -R and  $Z''$  goes to zero. The response due to the two elements is shown separately in Fig. 81 a) and together, in an extended frequency range in Fig. 81 b).

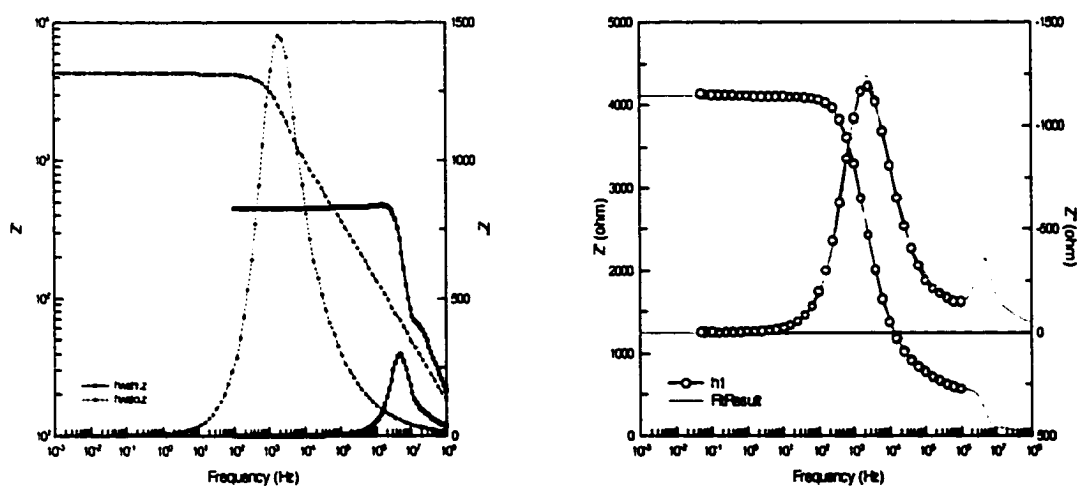


FIG. 81. a) Separate response of the two Warburg circuits. b) Data and extended fit with the equivalent circuit

Fitted parameters of the model for the non-irradiated and irradiated samples follow. As in other instances we are using the horizontal index axis to arrange the measurements chronologically, roughly simulating a time axis. The real times associated with the

indices 1-15 are:  $t = 0,373, 791, 1231, 1771, 3015, 3500, 3974, 4596, 4879, 5299, 6516, 6822, 7557$  and  $7969$  s.

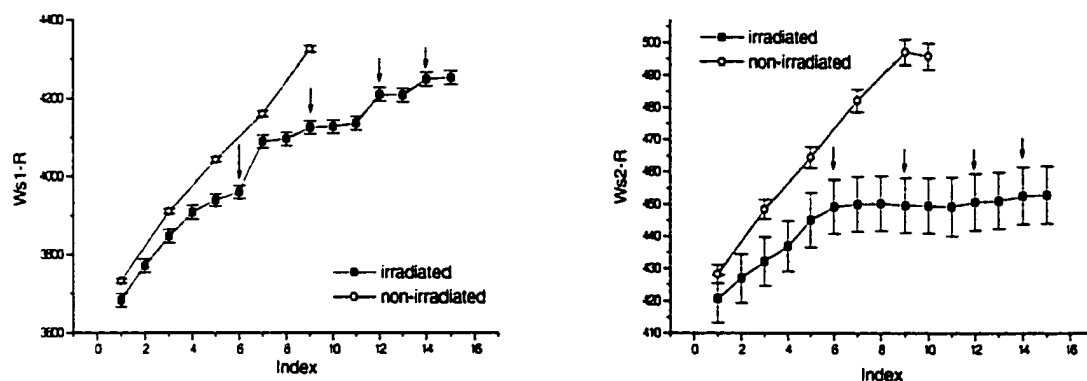


FIG. 82. Evolution of the Ws1-R and Ws2-R parameters for irradiated and non-irradiated samples

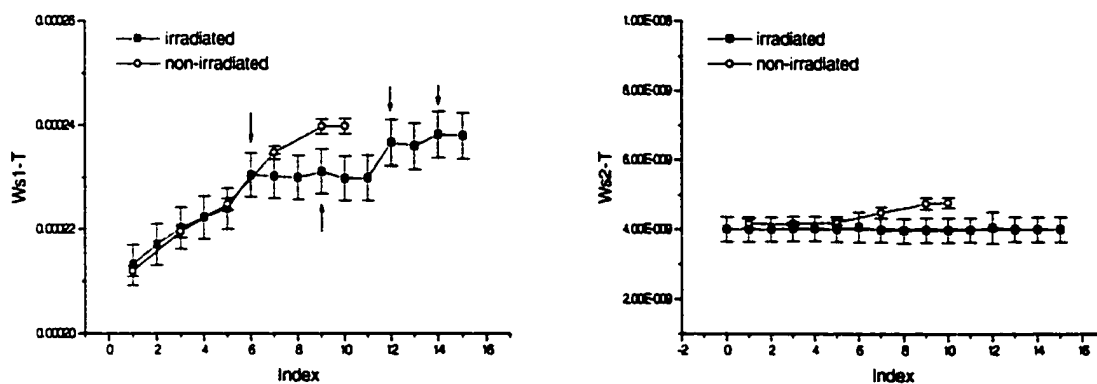


FIG. 83. Evolution of the Ws1-T and Ws2-T parameters for irradiated and non-irradiated samples

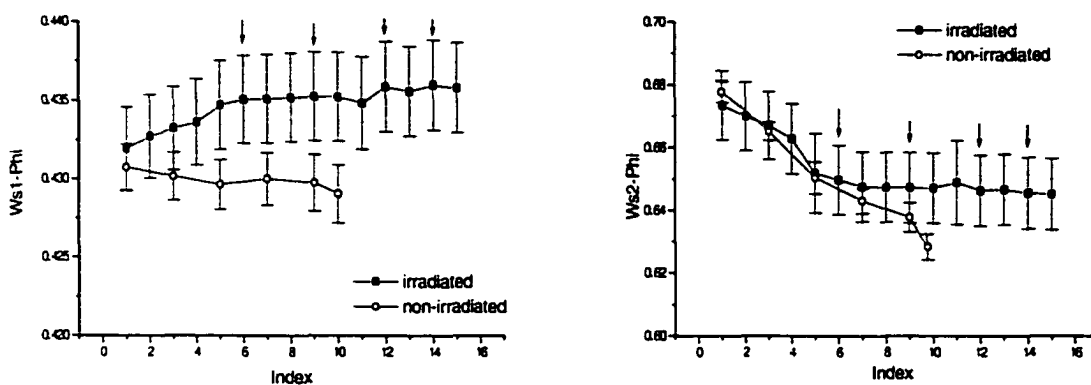


FIG. 84. Evolution of the  $Ws1$ - $\Phi$  and  $Ws2$ - $\Phi$  parameters for irradiated and non-irradiated samples.

Some of the model parameters have the property that for the irradiated and non-irradiated sample, they appear to diverge even before the first irradiation. The excision and the irradiation effects were studied on different samples. Even though they came from healthy animals and have similar sizes, the variability of impedance parameters was still a problem, especially for non-pair organs like the heart. We would like to stress once again that these studies are of importance with respect to changes in impedance and impedance based models *in the same organism (tissue)*, after the irradiation, with respect to the *before* situation. We are not seeking to establish any absolute values from which the deviation to be interpreted. The study of different tissue samples should only be seen in this context as a proof for consistent behavior, with the limits imposed by the biological variability.

A particularity of this tissue system is the very tightly cell packaging in a structure which has an obvious hierarchical character. Examining the graphs, we can see that the radiation induced changes in the R and T parameters of the first Warburg element are quite clearly marked. One reason for which they do not appear so well defined in the second Warburg element can be simply its relatively reduced contribution to the overall response. While from the start we tried to associate the response of this system at low frequencies with diffusion across the membrane, the interpretation of each of the model



parameters by relation to physical entities in the tissue is difficult.  $R$  is obviously a resistance in the limit  $\omega \rightarrow 0$  and  $T$  is a diffusion related quantity ( $\sim L^2/D$ ). It seems that the first radiation dose is really changing the course of time evolution for all parameters, while subsequent irradiation bring little contribution. The reduction of the distance over which the diffusion seems to take place, seen in  $W_{s1-T}$ , can be explained by proposing a mechanism in which the injection of charge and the creation of free radicals leads to an increased barrier layer capacitance and a subsequent reduction of the diffusion length. A continuation of such reasoning is given in the next chapter, in which an attempt is made to explain all the dispersions measured in the frame a 'universal' mechanism.

## **CHAPTER VII**

### **CONCLUSIONS**

This chapter is devoted to the ambitious and complex task of proposing a unitary interpretation of the data presented and analyzed in the precedent chapter. The difficulty comes from a number of sources:

- The theory of dielectric phenomena at low frequencies (LFD), our domain of interest, is itself a work in progress, with quite some debate on what the involved mechanisms are and how they should be presented in a unified frame (see the 'universal' dielectric dispersion - Jonscher). We will attempt to give a consistent explanation for the data collected, involving hopping conductivity in fractal systems.
- When the LFD measurements have as a subject biological tissue, the model's degree of complexity increases dramatically; the cell is a complex structure and an active, dynamic environment. A multitude of processes are taking place and the challenge is to restrict the analysis to those that are relevant for our goal.
- Irradiation of semiconductors and non-polar liquids [86] is rarely studied from a dielectric point of view. The first study of which we are aware on the dielectric properties [87], of irradiated tissues appeared after our first proposal submission to NIH, in 1998, and it is emphasizing only the long term effects in muscle, thus likely connecting necrosis with changes in conductivity and permittivity.

Our final goal is to be able not only to understand and quantify the dielectric changes in irradiated tissues but to use these changes in order to assess, both qualitatively and quantitatively the type of death occurring as a results of irradiation. As seen in Chapter II - Cell death, what we are looking for, are ways (or markers) for discriminating between oncosis and apoptosis, this being the focus of much of the today's search for new cancer treatments. Inducing apoptosis in tumor cells is the final goal of many chemotherapies, so if we can prove that the impedance measurements can detect the subtle signs of apoptosis, it is likely the method can be applied in a much larger context then radiation therapy.

One of the dogmas in the application of ionizing radiation to the cancer treatment is that the killing of the cells occurs as result of direct damage to the DNA. There is now convincing evidence that a significant target for radiation is also the plasma membrane [87]. Relatively recently, proof was brought [88] that extranuclear (cytoplasmic) and extracellular targets, in a free radical mediated process, can also lead to radiation-induced damage in living matter. The so-called *bystander* effect [89, 90] refers to the killing effect, on non-irradiated cells, of the medium in which irradiated cells were incubated. It was also evidenced, as another contributing mechanism, that cell-cell communication over the extracellular space triggers various kinds of intracellular signal transduction processes in the receptors cells. Little is known about the nature of the signaling molecules. It is though interesting to point out (and, in the same time, to move toward pathways which might be significant for cell's dielectric properties) that even though the plasma membrane involvement in the events leading to mutagenesis or DNA repair, is not fully understood, recent studies [79] showed that membrane potassium  $K^+$  currents, activated by ionizing radiation, play a significant role in mutagenesis<sup>24</sup>. The kinetics of the current induction is very rapid, occurring in a few minutes after irradiation, with a relaxation time of the order of minutes. The mechanism of  $K^+$  current activation was proven to be due to free radicals. Consistent with our findings, apoptotic death induced by free radical attack is correlated with a decrease of membrane conductivity [15], suggesting that one of the *early events* in the triggering of apoptosis is an overall *reduction of plasma membrane function*.

In general, changes in the dielectric properties of the membrane are reported in literature as occurring early after irradiation [89]. The electrical capacitance of lipid membranes may increase [90] by up to 50% on exposure to ionizing radiation. This is the consequence of lipid peroxidation induced by primary or secondary radicals of water radiolysis in the presence of oxygen. The polar products of this process give rise to an increase in the dielectric constant of the membrane. This in turn leads to the observed increase in the membrane capacitance.

Before discussing dielectric properties further, we will give an overview of possible dielectric responses:

---

<sup>24</sup>the process leading to a mutation, a change of the hereditary information, an alteration of genes.

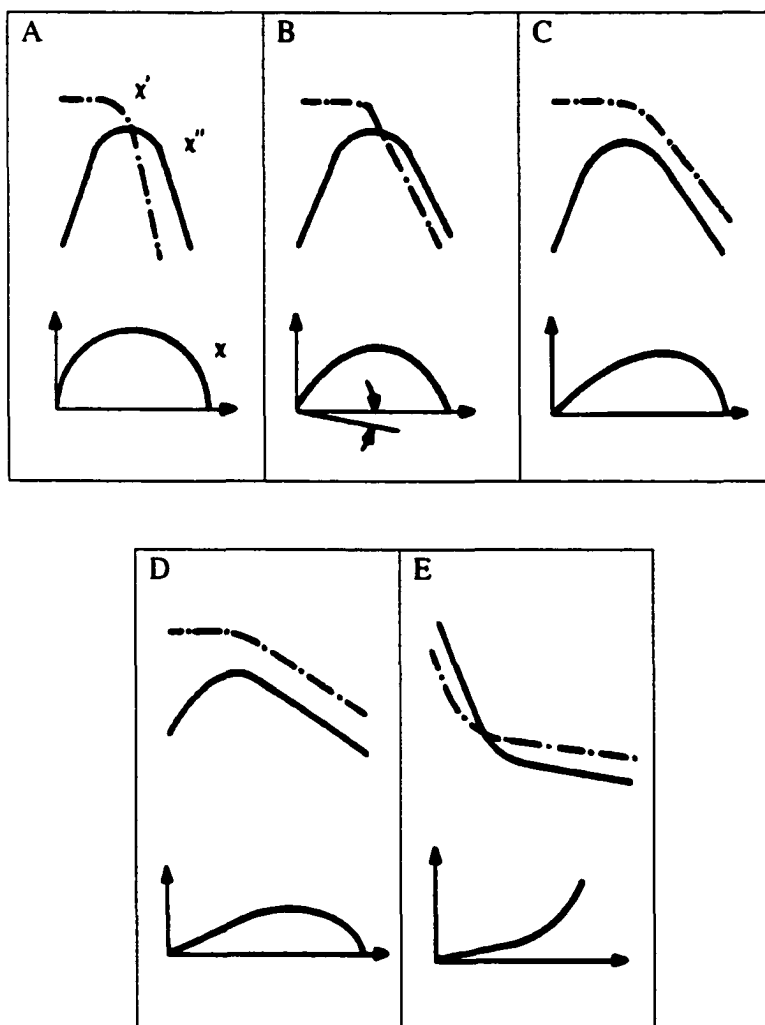


FIG. 85. A representation of different types of dielectric responses. The two upper curves of each representation are the plots of the real and imaginary components of the susceptibility (in logarithmic scale). The lower curve is the complex plot of the same two quantities. In A is represented the Debye mechanism, the response (almost inexistent) of a collection of non-interacting dipoles. B, usually occurring in liquids, implies short, nearest-neighbor interactions, such the both  $\epsilon'$  and  $\epsilon''$  are proportional with  $\omega^n$  ( $n < 0.3$ ); C represents also a response in a system with the same type of interactions as B, but characterizing the low frequency dispersion with  $n \sim 0.5$ ; in D a higher frequency response is shown, typically observed in polymers,  $n > 0.6$ ; in E, the mechanism of relaxation is due to hopping charges and the interactions are of the 'many-body' type. Characteristic to ionic conductors or high-density carrier systems,  $n < 0.3$  (adapted from [91])

In analyzing and interpreting dielectric data, one has a number of choices, based on different parameters and strategies:

- a phenomenological approach, often obtained by fitting  $\epsilon = \epsilon(f)$ .
- an equivalent circuit model. This approach was taken in Chapter VI, where each tissue was discussed based on a model. Has the advantage that parameters can be interpreted if the model is physically interpretable.
- a direct interpretation of the primary data:  $Z$ ,  $M$ ,  $R_{\text{echiv}}$  or  $C_{\text{echiv}}$  as functions of frequency.
- an interpretation of the tissue system as a fractal or disordered system. The electrical excitation, conduction and polarisation can then be interpreted as random walks, variation of trapping and release time of the mobile charge carriers, changes in the conductive bonds density, etc.

Each tissue type was previously discussed based on an equivalent circuit model. We are giving now another point of view; a phenomenological approach, recently proposed by Raicu [92]. None of the Debye-type models (including Cole-Cole and Cole-Davidson models) or the "universal" one, proposed by Jonscher [93], and represented by the fractional power laws, are able to completely describe the dielectric response of the biological tissue. The broadening of the Debye dispersion peaks has been related to some distribution of the relaxation times, expressed by the  $\alpha$  coefficient in the Cole-Cole model:

$$\epsilon' = \epsilon_{\infty} + \frac{\epsilon_0 - \epsilon_{\infty}}{1 + (i\omega\tau)^{1-\alpha}}, \quad (97)$$

respectively  $\beta$  in the Cole-Davidson one:

$$\epsilon' = \epsilon_{\infty} + \frac{\epsilon_0 - \epsilon_{\infty}}{(1 + i\omega\tau)^{\beta}}. \quad (98)$$

Raicu [92] introduces yet another phenomenological expression, combining the Debye-type models with the power law (or CPA-type) models:

$$\varepsilon^* = \varepsilon_\infty + \frac{\varepsilon_0 - \varepsilon_\infty}{\left[ (i\omega\tau)^\alpha + (i\omega\tau)^{1-\beta} \right]^\gamma} + \frac{\sigma_0}{i\omega}, \quad (99)$$

where  $\alpha, \beta, \gamma \in [0..1]$ ,  $\tau$  is the characteristic relaxation time,  $\varepsilon_0$  and  $\varepsilon_\infty$  are the limiting values of the permittivity at low and high frequencies respectively, and  $\sigma_0$  is the low frequency conductivity. While we can recognize the power laws in the asymptotic behavior:

$$\varepsilon - \varepsilon_\infty \propto \omega^{-\alpha} \text{ for } \omega < 2\pi/\tau, \quad (100)$$

and

$$\varepsilon - \varepsilon_\infty \propto \omega^{\beta-1} \text{ for } \omega > 2\pi/\tau, \quad (101)$$

it is certainly difficult to assign any physical meaning to the coefficients. It was recently shown [94] that for ionic materials (and biological tissue falls into this category), the exponents of the power laws depend on the dimensionality of the conduction pathway. Among other models used to describe the frequency dependence of the conductivity - the distribution of the energy barriers, the inter-ion interaction or correlated motion - only those using percolation systems and random walks in a fractal system achieved power law dispersion with exponents depending on dimension. Conductivity is proportional with the diffusion constant:

$$\sigma = \frac{e^2 n}{kT} D, \quad (102)$$

and diffusion can be simulated using random walkers<sup>25</sup>:

After a long time  $t$ , the mean square displacement of all walkers,  $\langle r^2 \rangle$  is related to the diffusion coefficient  $D$  as:

---

<sup>25</sup>  $D = \lim_{t \rightarrow \infty} \langle r^2(t) \rangle / 2dt$

$$D \propto \langle r^2 \rangle / t. \quad (103)$$

In a Euclidian lattice, the mean square displacement increases linearly with time  $\langle r^2 \rangle \propto t$ , and therefore  $D$  is constant in time (normal, Fick diffusion). In a fractal lattice the diffusion coefficient increases slower than  $t$  and the diffusion is said to be anomalous:

$$\langle r^2 \rangle \propto t^{2/D_w}, \quad (104)$$

where  $D_w$  is the fractal dimension of the walker and  $D_w > 2$ . For a carrier of charge  $q$  and concentration  $n$ , the conductivity can be related to the  $\langle r^2 \rangle$  by the equation:

$$\sigma(f) \approx -\frac{nq^2 4\pi^2 f^2}{6kT} \int_0^{\infty} \langle r^2 \rangle e^{-i2\pi ft} dt. \quad (105)$$

However, in spite of numerous attempts to relate the exponents of the power laws to some fractal dimensions of the system, no consistent theory exists in present.

In a series of analytical studies using deterministic circuit models, Dissado [95] showed that the fractional power law ( $\epsilon' \propto \epsilon'' \propto \omega^{n-1}$ ) or the Constant Phase Angle (CPA) response occurs because sub-circuits on different levels contribute in self-similar ways to the response of the whole hierarchy, stressing the fact that the exponent  $n$  carries the information about the whole ensemble, the isolation of sub-circuits is impossible and the whole has to be represented by a unique frequency dependent circuit element. The tissue however, is not a deterministic fractal, the self-similarity is only present on average, and thus the fractal is called stochastic.

One of the most elusive phenomena, the dielectric dispersion of biological tissue at low frequency, can be thus explained by using the similitude with a percolation system. The extracellular path consists mainly of the extra-cellular plasma. Due to cell packing (some tissues are more compact than others, for example cardiac muscle is more compact than liver tissue) a three dimensional conducting maze is formed by the extracellular plasma (for completeness, one should also consider the gap junction network and the

possible proton conduction in glycocalyx). The tightly packed regions can be considered as poorly conducting bonds connecting clusters of cells. It was shown [95] that such systems are described by a combination of two fractional power laws, a high-frequency response with  $n > 0.5$  and a low frequency one  $n < 0.5$ . The qualitative explanation is that at high frequency, the mobile charges explore the highly connected clusters and the exponent  $n$  is in some relation with the cluster dimension  $d_f$ . A critical frequency will define the rate at which the charge will jump from one cluster to another. At frequencies lower than the critical frequencies, the carriers will explore the weakly conducting bonds. An intercluster and intracluster motion are thus separated and each seems to be described by one of the two power laws:

$$\begin{aligned}\chi' &\propto \chi'' \propto (\omega/\omega_c)^{n-1} & \omega > \omega_c \\ \chi' &\propto \chi'' \propto (\omega/\omega_c)^{-p} & \omega < \omega_c.\end{aligned}\tag{106}$$

An analytical expression for the complex susceptibility is given [96]:

$$\chi(\omega) = \chi(0) \left( \frac{\omega_c}{\omega_c + i\omega} \right) {}_2F_1 \left( 1-n, 1+p; 2-n; \frac{\omega_c}{\omega_c + i\omega} \right)\tag{107}$$

where  ${}_2F_1(\dots)$  is the Gaussian hypergeometric function defined by the relation:

$$\int_0^{\infty} \frac{x^a}{1+zx^b} dx = \frac{1}{z(b-a-1)} {}_2F_1 \left( 1, \frac{b-a-1}{b}; 1 + \frac{b-a-1}{b}; -\frac{1}{z} \right)\tag{108}$$

The results of our experiments on fresh kidney are shown in Figure 86:



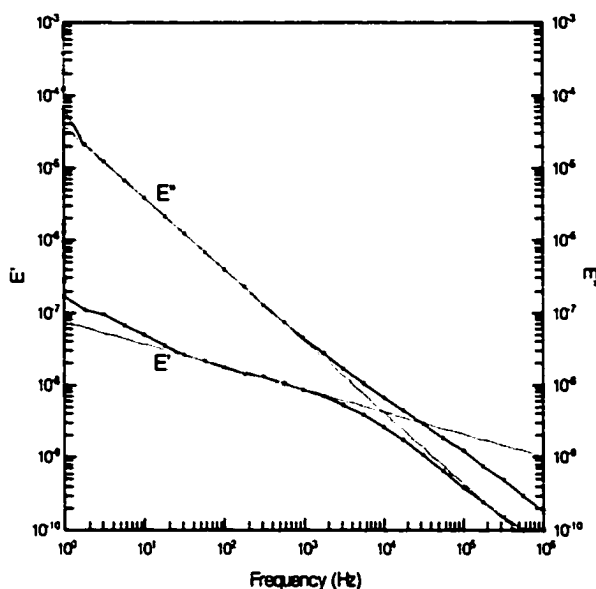


FIG. 86. Dielectric response of freshly excised kidney tissue. The power law frequency dependence of  $\epsilon'(\omega)$  and  $\epsilon''(\omega)$  (straight lines in log-log representation) are shown. The tissue was not irradiated.

The exponents of the  $\epsilon'$  and  $\epsilon''$  vs.  $\omega$  are extracted for the non-irradiated samples and presented in the table below (the errors in these coefficients are smaller than 0.002). The exponents refer to  $n$  and  $p$ , discussed in Eq. (106); the only difference between electrical susceptibility and permeability is shown in the expression for the real and imaginary part  $1 + \chi' = \epsilon'/\epsilon_0$ ,  $\chi'' = \epsilon''$ .

If these coefficients are related, as discussed before, to the dimensionality of the processes governing the  $\alpha$  (at low frequency)  $\beta$  (high frequency) dispersion, the interpretation is clear and straightforward related to the oncotic swelling of the cells following excision.

TABLE VI. The fractional exponents of the power laws describing the dielectric response of kidney tissue at high respectively low frequency.

Time	$\epsilon'$ Low Freq	$\epsilon'$ High Freq	$\epsilon''$ Low Freq	$\epsilon''$ High Freq
0	0.357	0.858	1.000	0.780
837	0.348	0.852	1.000	0.777
1539	0.340	0.845	1.000	0.775
4227	0.319	0.832	1.000	0.772
35098	<b>0.284</b>	<b>0.752</b>	<b>1.000</b>	<b>0.796</b>
36337	<b>0.283</b>	<b>0.746</b>	<b>1.000</b>	<b>0.797</b>

It is interesting to notice, that the same coefficients, this time analyzed from the irradiated samples dielectric response, exhibit very little variation:  $\epsilon'$  at low frequency is between 0.295 and 0.290, and  $\epsilon'$  at high frequency starts at 0.815 to decrease to 0.787.

Table VII. The fractional exponents of the power laws describing the dielectric response of irradiated kidney tissue at low frequency

Type	$\epsilon'$ Low Freq	$\epsilon'$ High Freq
Control	0.295	0.815
I irradiation	0.292	0.798
II irradiation	0.290	0.793
III irradiation	0.293	0.789
IV irradiation	0.294	0.787

Given that the tissues were measured in the same conditions, the lack of morphological changes can only be interpreted in the simultaneously presence of oncosis and apoptosis. One can see that in spite of the different slopes that can be attributed to different linear portions of these curves, there is much resemblance between them. A mention on the numerical values on these graphs is worthwhile. The permittivity is extracted from the impedance data by using an additional parameter, the capacitance of the empty measurement cell  $C_0$ . Since we were only interested in relative values, this parameter was

set to zero.

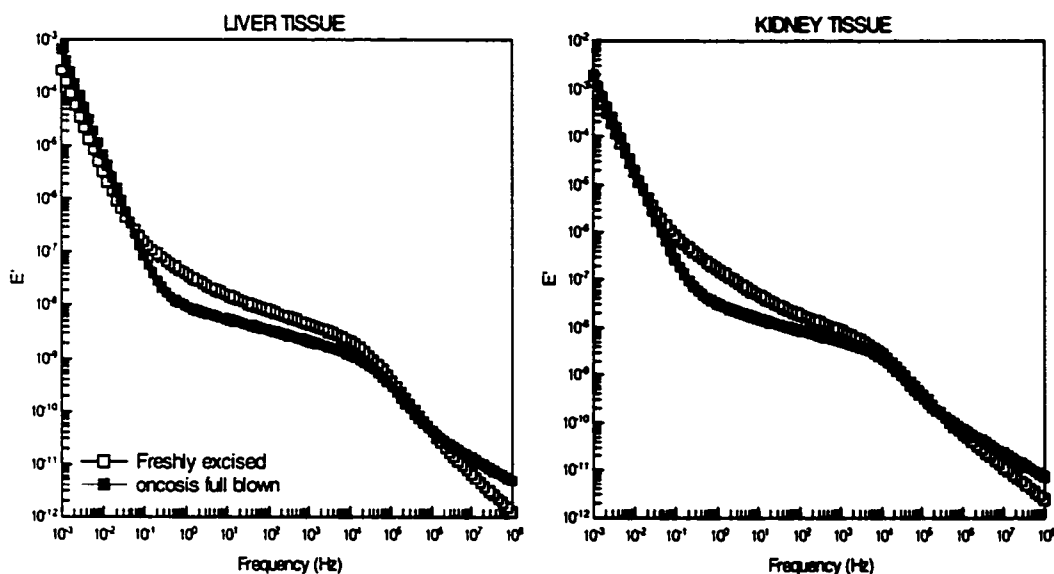


FIG. 87. Permittivity,  $\text{Re}(\epsilon)$  vs. frequency for liver and kidney tissue

However, for our measurement cell, the capacitance was about  $10^{-12}$  F, which means that all the values represented on these graphs should be shifted with  $10^{12}$ . For a better comparison all four tissue types are shown, in the next graph (Fig. 88), for both,  $\text{Re}(\epsilon)$  and  $\text{Im}(\epsilon)$ .

As we can see from these graphs, the tissues, when examined in terms of electric permittivity vs. frequency, exhibit a 'universal' response. The disadvantage of such representation is that all the intricacies of the dielectric phenomena are 'compressed' in one number, the slope of the straight line representing in fact the exponent of the frequency from the proportionality  $\epsilon' \sim \epsilon'' \sim \omega^n$ . If we would be able to give a precise meaning to this exponent and to detect any changes, that would turn into an advantage. Right now, we consider that the modeling of tissues with an equivalent circuit and the impedance analysis of the data gives a more rich and interpretable information.

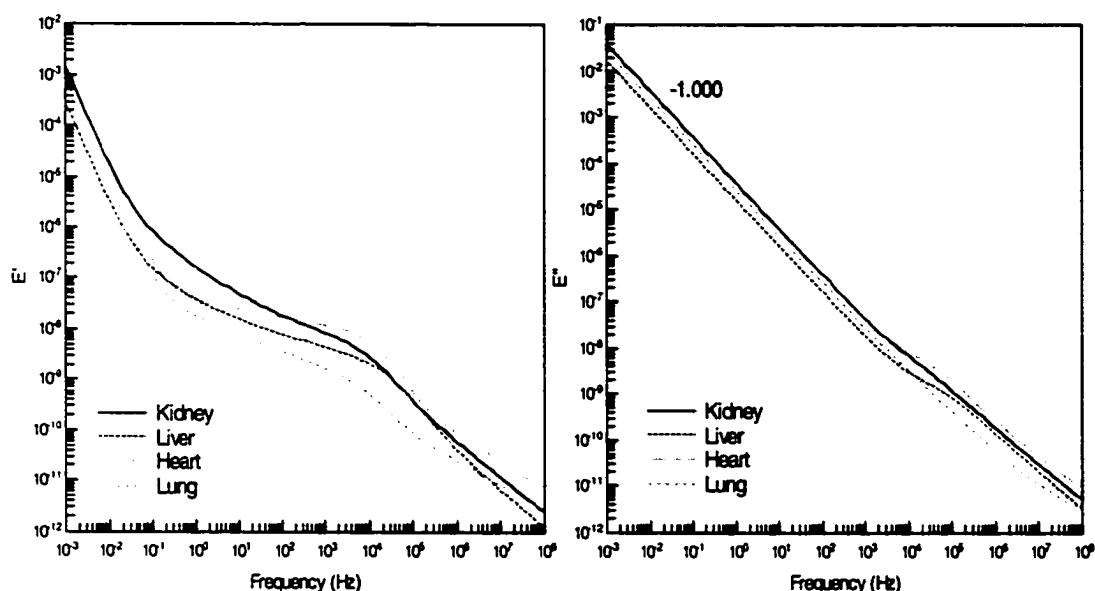


FIG. 88. Representation of  $\epsilon' = \text{Re}(\epsilon)$  and  $\epsilon'' = \text{Im}(\epsilon)$  versus frequency, a 'universal' response of tissues.

To conclude our study we can state, based on our experimental data on excised tissue, that impedance measurements in the frequency domain from 50 mHz to 1 MHz seems to have the potential to distinguish between different death mechanisms at the level of the tissue. The extent of what we detected as apoptosis or oncosis still remains to be confirmed by additional experiments. The study also proves the existence of a correlation between the known radiosensitivity of a certain tissue and the magnitude of the radiation-induced impedance changes (see for example in Chapter VI, liver vs. kidney). Without doubt, a very interesting feature seems to be the examination of the transient changes at the level of membrane, which according to recent studies, might precede the onset of apoptosis.

The use of electrodes, which might exhibit a lack of spatial sensitivity in a real application, might be very conveniently replaced by MRI and simultaneous current

injection, which would allow the imaging of conductivity with submillimeter resolution. What our goal was in this study, was to prove that electrical impedance can represent a sensitive marker to subtle radiation-induced changes. We believe that there is an enormous potential for such a method to become a routine determination during the radiation treatment.

## REFERENCES

- [1] C.C. Ling *et al.*, *Int. J. Radiat. Oncol. Biol. Phys.* **47**(3), 551-560 (2000).
- [2] P. Debye, *Polar Molecules* (The Chemical Catalog Company, Inc. 1929).
- [3] J.H. Van Vleck, *Electric and magnetic Susceptibilities* (Oxford, London, 1932).
- [4] H. Frohlich, *Theory of dielectrics* (Oxford, London, 1949).
- [5] K. Beravs, A. Demsar, F. Demsar, *J. of Mag. Res.* **137**, 253-257, (1999).
- [6] I. Sersa, *et al.*, *Mag. Res. in Med.*, **37**, 404-409, (1997).
- [7] M.D. Scott Fields *et al.*, "*Electrical impedance imaging of the Breast*" exhibit presented at the Radiological Society of North America Convention, Chicago, Illinois. 29 November (1998).
- [8] R.D. Evans, *The atomic nucleus* (McGraw-Hill Book Company, Inc. 1955).
- [9] E.L. Alpen, *Radiation Biophysics*, 2<sup>nd</sup> edition, (Academic Press, 1998).
- [10] H.A. Bethe and J. Ashkin, in *Experimental Nuclear Physics*, edited by E. Segre, (Wiley, New York, 1953), Vol. 1, p. 166.
- [11] A. Mozumder and J.L. Magee, *Rad. Res.*, **28**, 203, (1966).
- [12] V.V. Balashov, *Interaction of particles and radiation with matter* (Springer-Verlag, 1997).
- [13] B.F. Trump and I.K. Berezevsky, *Biochim. et Biophys. Acta*, **1313**, 173-178 (1996); in *When Cells Die- A Comprehensive Evaluation of Apoptosis and Programmed Cell Death*, edited by R.A. Locksmith, Z. Zakeri and J.L. Tilly (John Wiley & Sons, New York, Singapore, Toronto, 1998), p. 57.
- [14] G. Majno and I. Joris, *Amer. J. of Path.*, **146**, 1 (1995).
- [15] A. Bonincontro, C. Cametti, A. Rosi and L. Sportelli, *Int. J. of Rad. Biol.*, **52**, 447-457 (1987).
- [16] D.J. Canaday *et al.*, *New York Academy Of Sciences*, **720**, 153-159 (1994).
- [17] J.C. Edwards, D. Chapman, W.A. Cramp and M.B. Yatvin, *Prog. In Biophys. and Mol. Biol.*, **43**, 71-93 (1984).
- [18] E. Grzelinska, A. Bartkowiak, G. Bartosz and W. Leyko, *Int. J. of Rad. Biol.*, **41**, 473-481 (1982).

- [19] P. Santana, *et al.*, *Cell*, **86**, 189-199 (1996).
- [20] M. Valkonen and T. Kuusi, *J. of Lipid Res.*, **38**, 823, (1997).
- [21] H. Fricke, *Phys. Rev.*, **26**, 678 (1925).
- [22] E.H. Grant, R.J. Shepard and G.P. South, *Dielectric behavior of biological molecules in solution* (Clarendon Press, Oxford 1978).
- [23] A. Chelkowski, *Dielectric Physics* (Elsevier Scientific Publishing Company 1980).
- [24] K.S. Cole and R.H. Cole, *J. Chem. Phys.*, **9**, 341 (1941).
- [25] K.S. Cole and R.H. Cole, *J. Chem. Phys.*, **10**, 98 (1942).
- [26] P. Debye, *Polar Molecules* (Dover Publications, Inc. 1929).
- [27] L. Onsager, *J. Am. Chem Soc.*, **58**, 1486 (1936).
- [28] J.G. Kirkwood, *Trans. Faraday Soc.*, **42A**, 7 (1946).
- [29] L.A. Dissado and R.M. Hill, *Nature*, **279**, 685 (1979).
- [30] H.P. Schwan, in *Advances in Biological and Medical Physics* (Academic Press, New York 1957), Vol. 5, p.147.
- [31] H.P. Schwan, *et al.*, *J. Phys. Chem.*, **66**, 2626 (1962).
- [32] R. Pethig, *Dielectric and Electronic properties of biological materials* (John Willey & Sons, New York 1979).
- [33] K.W. Wagner, *Arch. F. Electrotechnik*, **2**, 271 (1914).
- [34] T. Hanai, K. Asami and N. Koizumi, *Bull. Inst. Chem. Res. Kyoto Univ.*, **57**, 297, (1979).
- [35] C.T. O'Konski, *J. Phys. Chem.*, **64**, 605-19 (1960).
- [36] G.A. Schwartz, *J. Phys. Chem.*, **66**, 2636-42 (1962).
- [37] L. Onsager, *Science*, **166**, 1359-64 (1969).
- [38] R.M. Hill, C. Pickup, *J. of Mat. Sci.*, **20**, 4431-4444, (1985).
- [39] L.A. Dissado, *Phys. Med. Biol.*, **35**(11), 1487-1503 (1990).
- [40] T. Kaplan, and L.J. Gray, *Phys. Rev.* **B32**, 7360-6 (1985).
- [41] B. Bianco, A. Chiabrera, S. Giordano, *Bioelectromagnetics* **21**, 145-149 (2000).
- [42] A. Szent-Györgyi, *The living state and cancer* (Marcel Dekker, Inc., New York and Basel, 1978).
- [43] R. Pethig; in *Modern Bioelectrochemistry*, edited by F. Gutmann and H. Keyzer (Plenum Press, New York, 1986), p.199.

- [44] P.E. Wellstead, Solartron Technical Report 010/83, on Frequency Response Analysis, 1990
- [45] Schwan, H.P., in *Physical Techniques in Biological Research*, (Academic Press Inc1963), Vol IV, Part B, p.323.
- [46] McAdams, E.T. and Jossinet, J., *Innov. Tech. Biol. Med.*, **12**(1), 11-20 (1991); *IEEE Trans. Biomed. Eng.*, **41**(5), 498-500 (1994).
- [47] Simpson R.W., Berberian J.G. and Schwan, H.P., *IEEE Trans. On Biomed. Eng.* **BME-27**(3), 166 (1980).
- [48] Craig, D.Q.M., in *Dielectric Analysis of Pharmaceutical Systems* (Taylor & Francis, 1995).
- [49] Raicu, V. Saibara, T., Irimajiri, A., *Bioelectrochemistry and Bioenergetics*, **47**, 325-332 (1998).
- [50] Faiz Khan, *The Physics of Radiation Therapy* (Williams & Wilkins 1984, 1998).
- [51] Varian Associates, Radiation Division, Clinac Equipment Specifications (1999).
- [52] J.R. Macdonald, *Impedance Spectroscopy. Emphasizing solid materials and systems.* (John Wiley & Sons, New York, 1987).
- [53] H.A. Kramers, *Phys. Zeit.* **30**, 52 (1929).
- [54] R. de L. Kronig, *J.Opt.Soc. Am.* **12**, 547 (1926).
- [55] A.K. Jonscher, *Nature*, **267**, 673-679 (1977).
- [56] J.R. MacDonald, *Complex Nonlinear Least Squares Immitance Fitting Program LEVM, V7.0*, (1997).
- [57] W.J., Adelman., and D.E. Goldman, *The biophysical approach to excitable systems* (Plenum Press 1981).
- [58] C. Gabriel, S. Gabriel, E. Corhout, *Phys. Med. Biol.*, **41**, 2231-2249 (1996).
- [59] D. Andreuccetti, C. Petrucci and R. Fossi, the ITALIAN NATIONAL RESEARCH COUNCIL, Electromagnetic Wave Research Institute, "Nello Carrara" - Florence (Italy); Internet document; URL: <http://sparc10.iroec.fi.cnr.it/tissprop/> (1999)
- [60] M. Benderitter, *et al.*, *Int. J. Radiat. Biol.*, **75**(8),1043-53 (1999).
- [61] K.I. Altman, G. B. Gerber, *Radiation Biochemistry* (Academic Press, 1970), Vol. II, p.37.



- [62] A. Bonincontro, C. Cametti, A. Rosi and L. Sportelli, *Int. J. Radiat. Biol. Relat. Stud. Chem. Med.*, **52**(3), 447-457 (1987).
- [63] E.J. Hall, *Radiobiology for the Radiologist* (Harper & Row, Publishers, Inc. 1973), p. 192.
- [64] F. Ellinger, *Medical Radiation Biology* (Thomas, Springfield, Illinois, 1957).
- [65] V. Hlavaty, M. Zak, and P. Jirounek, *Nature*, 1057, (1965).
- [66] R. Pethig, *Ferroelectrics*, **86**, 31 (1988).
- [67] J.R. MacDonald, *J. Appl. Physics*, **58**, 1955-1970 (1985).
- [68] K. Krischer, in *Modern aspects of electrochemistry*, **32**, 1-138 (1999).
- [69] M.T.M., Koper, *Electrochimica Acta*, **37**, 1771-1778 (1993).
- [70] K.I. Altman, G.B. Gerber and S. Okada, *Radiation Biochemistry* (Academic Press, New York and London, 1970).
- [71] C. Gabriel and S. Gabriel: "Compilation of the Dielectric Properties of Body Tissues at RF and Microwave Frequencies", Internet document; URL: <http://www.brooks.af.mil/AFRL/HED/hedr/reports/dielectric/home.html>
- [72] Foster, K.R., Schwan, H.P., in *Handbook of Biological effects of electromagnetic fields*, 2<sup>nd</sup> edition (CRC Press, 1996).
- [73] M. Gheorghiu, E. Gersing and E. Gheorghiu, *Ann. New York Acad Sci.* **873**, 65-72 (1999).
- [74] A.A. Pilla, in *Bioelectrochemistry: Ions, Surfaces, Membranes*, edited by M. Blank, Vol. 188, (1980).
- [75] J. J. Ackerman, and M.A. Seitz, *Crit. Rev. in Biomed. Eng.*, **11**(4), 281-311, (1989).
- [76] V. Raicu, T. Saibara, H. Enzan and A. Irimajiri, *Bioelectrochemistry and Bioenergetics*, **47** (2), 333 (1998); **47** (2) 325 (1998)
- [77] A. Surowiec, S. S. Stuchly and A. Swarup, *Phys. Med. Biol.*, **30**(10); 1131-41 (1985).
- [78] A. Bonincontro, A. Icaoangeli, G. Melluci-Vigo and G. Risuleo, *Biosci. Rep.*, **17**(6), 547-56 (1997).
- [79] A.H. Saad, L. Y. Zhou, E.K. Lambe and G. M. Hahn, *Mut. Res.*, **324** (4), 171-176 (1999).

- [80] U. Zeidler, M. Wilhelm and G. Stark, *Biochim. Biophys. Acta*, **1281**(1), 73-9 (1996).
- [81] Y. Konishi, Y. Morimoto and T. Kinouchi, *Res. Exp. Med. (Berl)*, **195**(4): 183-92 (1995).
- [82] P.M. Iannaccone and M. Khokha, (editors), *Fractal geometry in Biological systems* (CRC Press, 1995).
- [83] V. Raicu, *Phys. Rev. E*, **60**, 4, 4677-4680 (1999).
- [84] J.R. McDonald, *Journal of Chem. Phys.*, **102** (15), 6241-50 (1995).
- [85] O. Casas, *et al.*, *Ann. New York Acad. Sciences*, **873**, 51-59 (1999).
- [86] W.F. Schmidt, *Liquid state electronics of insulating liquids* (CRC Press 1997).
- [87] K.D. Paulsen, K.S. Osterman and P.J. Hoopes, *Rad. Res.* **152**, 41-50 (1999).
- [88] L. J. Wu, *et al.* *Proc. Natl. Acad. Sci. USA*, **96**, 4959-4964 (1999).
- [89] H. Zhou, *et al.*, *Proc. Natl. Acad. Sci. USA*, **97**, No 5, 2099-2104 (2000).
- [90] C. Mothersill, *British J Cancer*, **82**(10), 1740-6 (2000).
- [91] U. Zeidler, M. Wilhelm and G. Stark, *Biochim. Biophys. Acta*, **1281**(1):73-9 (1996).
- [92] M. Strassle, M. Wilhelm and G. Stark, *Int. J. Radiat. Biol.*, **59**(1):71-83 (1991).
- [93] K.L. Ngai, A.K. Jonscher and C.T. White, *Nature*, **277**, 185-189 (1979).
- [94] V. Raicu, *Phys. Rev. E*, **60**(4), 4677-80 (1999).
- [95] A.K. Jonscher, *Nature* **267**, 673-679 (1977).
- [96] D. L. Sidebottom, *Phys. Rev.Lett.*, **83**(5), 983-986 (1999).
- [97] L.A. Dissado, *Phys. Med. Biol.* **11**, 1487-1503 (1990).
- [98] L.A. Dissado, R.M. Hill, *J. Chem. Soc. Faraday. Trans.*, **80**(2), 291-319 (1984).

## APPENDIX A

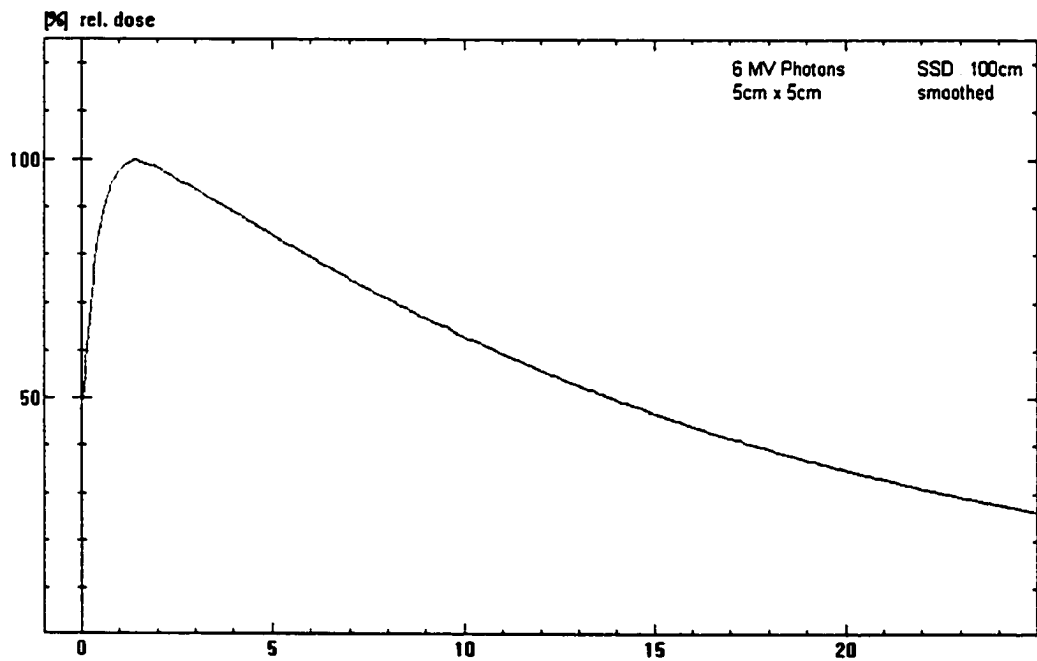
DEPTH DOSE AND ISODOSE DISTRIBUTIONS FOR 6 MV  
PHOTONS.

Figure 89A. Plot of absorbed dose in water as a function of depth for 5MV photons in a  $(5 \times 5)$  cm<sup>2</sup> field.

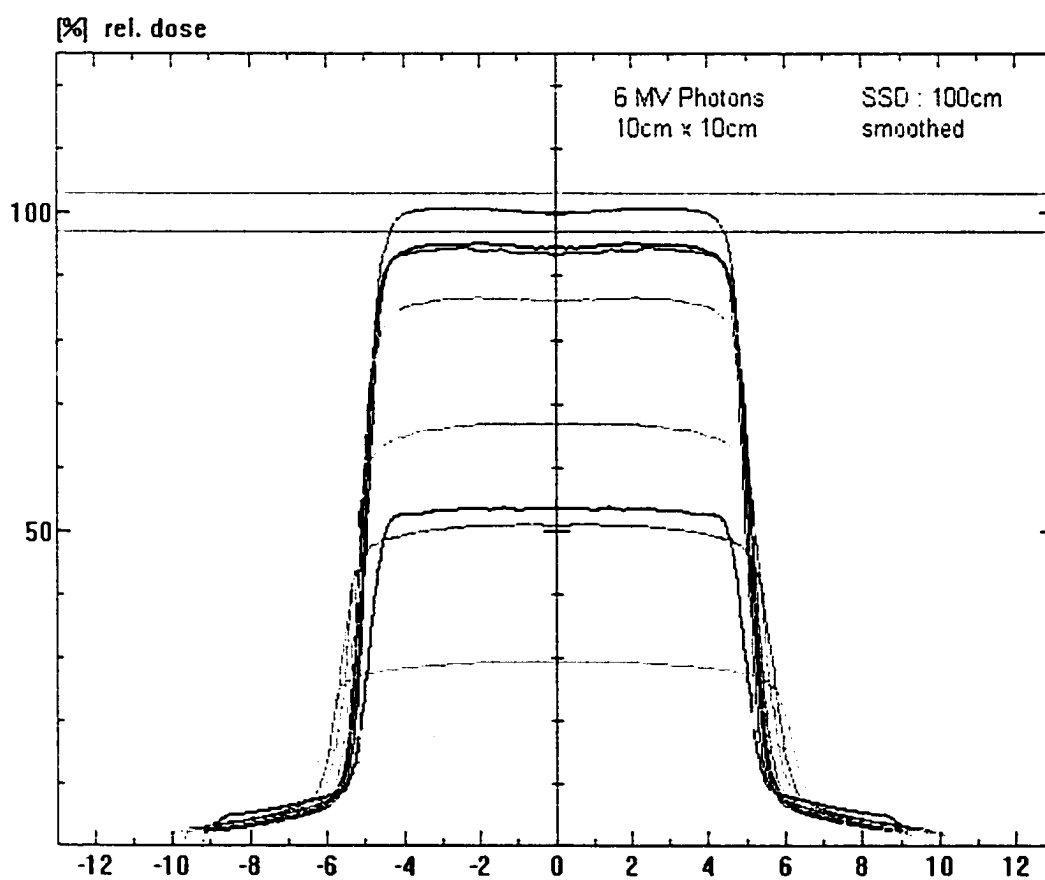


Figure 90A. Depth dose variation across the field for 6 MV photons, SSD=100cm, field of  $(10 \times 10) \text{ cm}^2$ , depth of 3 cm.

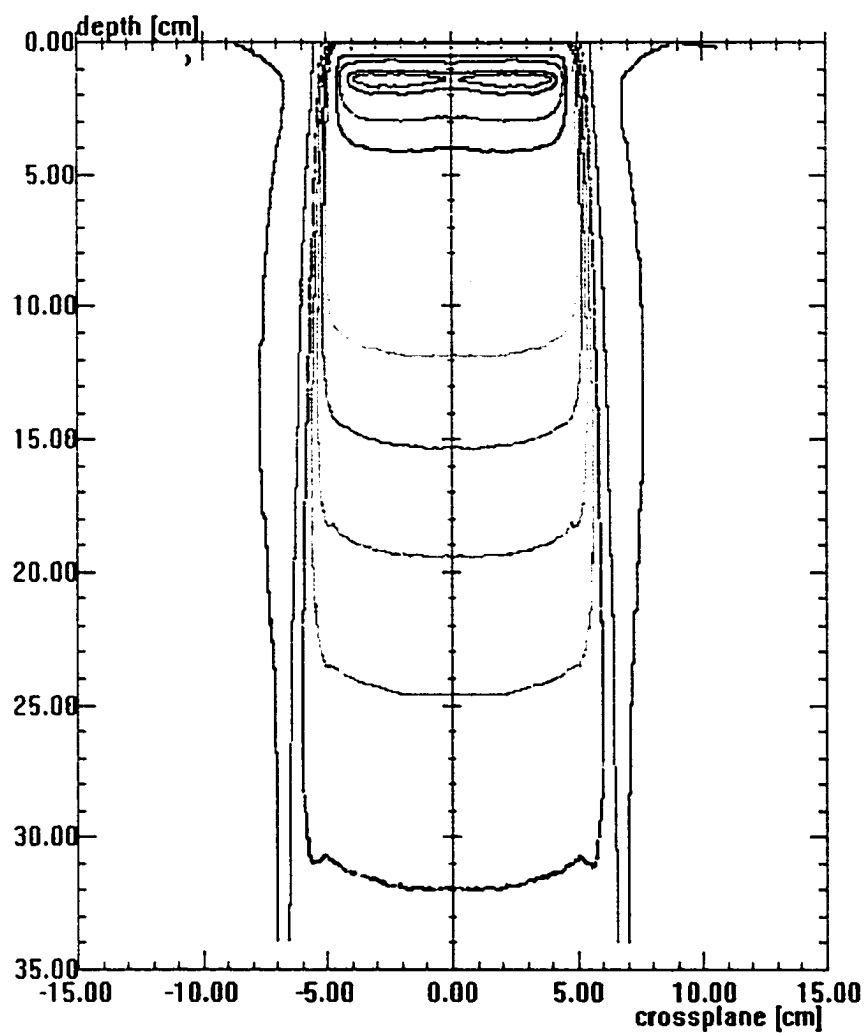


Figure 91A. Isodose distribution for 6 MV photons in a (10 x 10) cm<sup>2</sup> field, SSD=100 cm

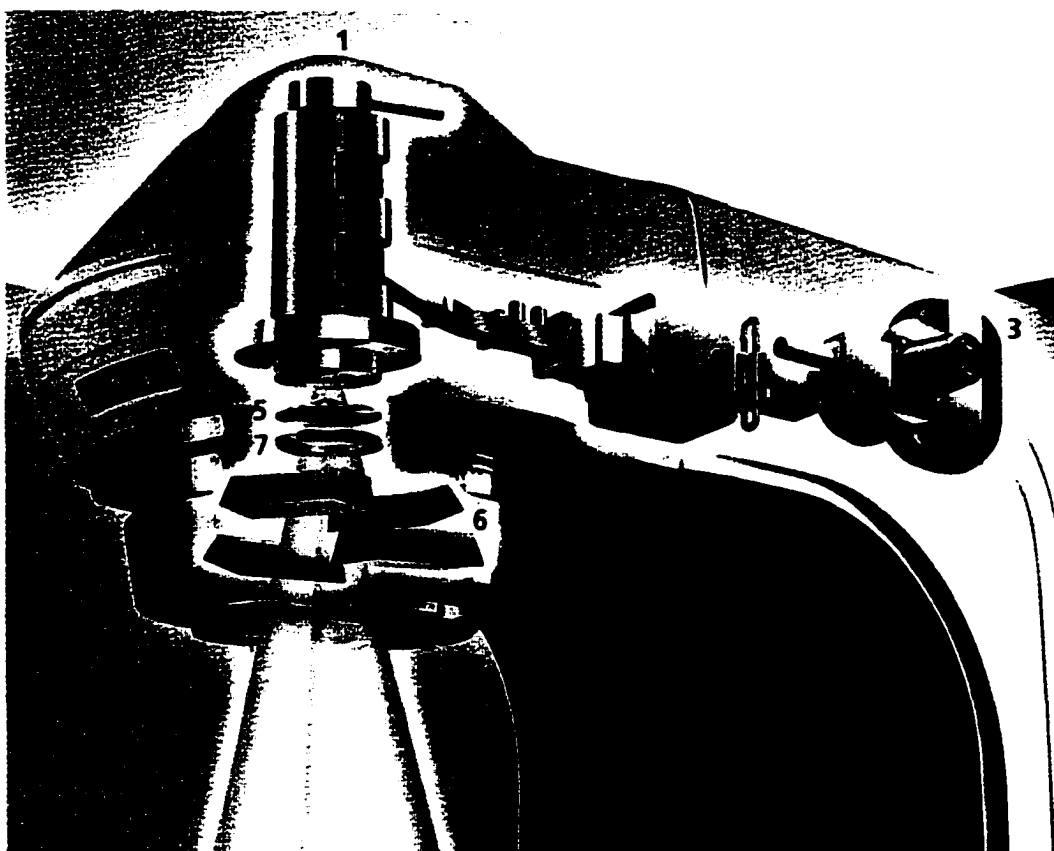


Figure 92A. An artist's view of the Clinac 600 series. 1-electron gun characterized by a circular electron emitting surface; 2- standing wave generator; 3-magnetron, generates the high power microwaves used to accelerate electrons in the wave guide; 4-port circulator, damps the reflected microwaves into a passive waterload, in order to protect the magnetron; 5-photon field flattener; 6-asymmetric jaws; 7-pair of two separately sealed ionization chambers for monitoring of dose rate, integrated dose and field symmetry.



**Figure 93A. The Clinac 1800 at Virginia Beach General Hospital. Right under the treatment head, the white parallelepiped is the thermal case of the electrolytic cell. On the treatment couch can be seen the Solartron Frequency Analyzer 1260, the Dielectric Interface 1294, the home made thermostat, other devices, the laptop doing the data acquisition and the large monitor replacing the LCD screen.**

## APPENDIX B

### PARAMETRIC MODEL AND TABLES

A parametric model, based on data gathered from literature, was created by Gabriel *et al.* [58]. In this model the complex permittivity is considered to be the sum of up to six Debye or Cole-Cole terms:

$$\epsilon(\omega) = \epsilon(\infty) + \sum_n \frac{\Delta\epsilon_n}{1 + (i\omega\tau_n)^{(1-\alpha_n)}} + \frac{\sigma_{ionic}}{i\omega\epsilon_0}$$

Based on this model, Andreuccetti *et al.* developed an application [59] where the calculations can be carried out for a specific tissue, for specific conditions (frequency range). The output of the program which models permittivity and conductivity for the tissue studied in our experiments, as function of frequency, are shown in Table II-VI.

The parameters of the model for  $n = 4$  are shown in the table below:

Table VIII B. Numerical values of the parametric model for blood, kidney, heart, lung, liver and muscle.

Tissue Type \	Parameter	$\epsilon(\infty)$	$\Delta_1$	$\tau_1$ (ps)	$\alpha_1$	$\Delta_2$	$\tau_2$ (ns)	$\alpha_2$	$\sigma$
Blood		4.000	56.00	8.377	0.100	5200	132.629	0.100	0.700
Heart		4.000	50.00	7.958	0.100	1200	159.155	0.050	0.050
Kidney		4.000	47.00	7.958	0.100	3500	198.944	0.220	0.050
Liver		4.000	39.00	8.842	0.100	6000	530.516	0.200	0.020
Lung (Deflated)		4.000	45.00	7.958	0.100	1000	159.155	0.100	0.200
Lung (Inflated)		2.500	18.00	7.958	0.100	500	63.662	0.100	0.030
Muscle		4.000	50.00	7.234	0.100	7000	353.678	0.100	0.200

Tissue Type \	Parameter	$\Delta_3$	$\tau_3$ ( $\mu$ s)	$\alpha_3$	$\Delta_4$	$\tau_4$ (ms)	$\alpha_4$
Blood		0.00E+0	159.155	0.200	0.00E+0	15.915	0.000
Heart		4.50E+5	72.343	0.220	2.50E+7	4.547	0.000
Kidney		2.50E+5	79.577	0.220	3.00E+7	4.547	0.000
Liver		5.00E+4	22.736	0.200	3.00E+7	15.915	0.050
Lung (Deflated)		5.00E+5	159.155	0.200	1.00E+7	15.915	0.000
Lung (Inflated)		2.50E+5	159.155	0.200	4.00E+7	7.958	0.000
Muscle		1.20E+6	318.310	0.100	2.50E+7	2.274	0.000



Table IXB. Dielectric parameters for blood in the frequency domain from 10 Hz to 10 MHz.

Frequency [Hz]	Conductivity [S/m]	Relative permittivity	Loss tangent	Wavelength [m]	Penetration depth [m]
10	0.7	5260	239220	1195.2	190.22
15.849	0.7	5260	150940	949.39	151.1
25.119	0.7	5259.9	95235	754.13	120.02
39.811	0.7	5259.9	60090	599.02	95.339
63.096	0.7	5259.9	37914	475.82	75.731
100	0.7	5259.8	23923	377.95	60.156
158.49	0.7	5259.7	15094	300.21	47.784
251.19	0.7	5259.6	9524.1	238.46	37.957
398.11	0.7	5259.4	6009.6	189.41	30.151
630.96	0.7	5259.1	3792	150.45	23.951
1000	0.7	5258.6	2392.8	119.5	19.026
1584.9	0.7	5257.9	1510	94.908	15.115
2511.9	0.7	5256.8	952.93	75.373	12.009
3981.1	0.70001	5255.1	601.46	59.853	9.5417
6309.6	0.70002	5252.4	379.69	47.519	7.5829
10000	0.70004	5248.2	239.77	37.716	6.0278
15849	0.70009	5241.4	151.49	29.922	4.7937
25119	0.70022	5230.3	95.805	23.72	3.8147
39811	0.70052	5211.6	60.692	18.78	3.0387
63096	0.70124	5178.9	38.576	14.84	2.4239
100000	0.70292	5120	24.678	11.688	1.9371
158490	0.7068	5011.5	15.996	9.1576	1.5514
251190	0.71546	4810.7	10.643	7.1175	1.2442
398110	0.73363	4450	7.4437	5.4723	0.99578
630960	0.76785	3856.5	5.6723	4.1617	0.78934
1e+06	0.82211	3026.3	4.8831	3.1504	0.61449
1.5849e+06	0.8906	2106.3	4.7957	2.3999	0.46982
2.5119e+06	0.95897	1318.6	5.2044	1.8519	0.35677
3.9811e+06	1.0164	777.75	5.9006	1.4449	0.27222
6.3096e+06	1.0612	456.88	6.6172	1.1335	0.2097
1e+07	1.0967	280.03	7.04	0.88962	0.16312

Table XB. Dielectric parameters for heart tissue in the frequency domain from 10 Hz to 10 MHz.

Frequency [Hz]	Conductivity [S/m]	Relative permittivity	Loss tangent	Wavelength [m]	Penetration depth [m]
10	0.053677	2.3562e+07	4.095	3824.6	775.24
15.849	0.05829	2.1194e+07	3.1193	2810.1	613.04
25.119	0.066566	1.6948e+07	2.8107	2054.3	463.34
39.811	0.077496	1.1344e+07	3.0846	1535.1	336.04
63.096	0.087314	6.3236e+06	3.9337	1188	243.16
100	0.093565	3.1637e+06	5.3162	941.52	180.66
158.49	0.096851	1.5894e+06	6.9111	750.99	138.06
251.19	0.098693	890070	7.9349	596.43	107.64
398.11	0.10029	585780	7.7302	469.2	84.958
630.96	0.10254	440940	6.6254	364.66	67.455
1000	0.1063	352850	5.4152	279.81	53.509
1584.9	0.11227	280860	4.5335	212.5	42.093
2511.9	0.12068	213770	4.04	160.68	32.675
3981.1	0.13106	153690	3.8505	121.75	25.053
6309.6	0.1425	105290	3.8556	92.765	19.082
10000	0.15421	70054	3.957	71.06	14.523
15849	0.16587	46157	4.0758	54.62	11.084
25119	0.17752	30566	4.1561	42.035	8.4908
39811	0.18939	20534	4.1645	32.335	6.5282
63096	0.20178	14064	4.0874	24.828	5.0348
100000	0.21511	9845.8	3.9272	19.009	3.8923
158490	0.22992	7048.7	3.6995	14.495	3.0132
251190	0.24714	5147.6	3.4358	10.995	2.3318
398110	0.26827	3799.9	3.1877	8.292	1.7971
630960	0.295	2780.4	3.0227	6.2301	1.3724
1e+06	0.32753	1967.3	2.9926	4.6892	1.0363
1.5849e+06	0.36303	1335.4	3.0832	3.5545	0.77821
2.5119e+06	0.39811	888.12	3.2078	2.7124	0.58676
3.9811e+06	0.432	596.28	3.2713	2.0743	0.44613
6.3096e+06	0.46594	411.45	3.2262	1.5833	0.34192
1e+07	0.50137	293.47	3.071	1.2034	0.26379

Table XIB. Dielectric parameters for kidney tissue in the frequency domain from 10 Hz to 10 MHz.

Frequency [Hz]	Conductivity [S/m]	Relative permittivity	Loss tangent	Wavelength [m]	Penetration depth [m]
10	0.05441	2.7988e+07	3.4945	3722.5	785.77
15.849	0.059944	2.5147e+07	2.7036	2707.3	618.78
25.119	0.069868	2.0053e+07	2.4934	1963.1	461.94
39.811	0.082971	1.3329e+07	2.8107	1461.6	329.66
63.096	0.094723	7.3068e+06	3.6933	1131.5	235.34
100	0.10216	3.5181e+06	5.2198	899.51	173.19
158.49	0.10596	1.6339e+06	7.3551	721.1	131.43
251.19	0.10786	802300	9.6206	576.81	101.84
398.11	0.10913	448960	10.975	458.42	79.91
630.96	0.11057	293000	10.751	361.42	63.12
1000	0.11274	212900	9.5189	282.61	49.951
1584.9	0.11604	160000	8.226	219.46	39.431
2511.9	0.12054	117870	7.3183	169.76	30.962
3981.1	0.12595	83493	6.8111	131.26	24.182
6309.6	0.13179	57254	6.5579	101.64	18.83
10000	0.13774	38748	6.3898	78.817	14.66
15849	0.14369	26412	6.1701	61.129	11.433
25119	0.14973	18419	5.8171	47.337	8.9395
39811	0.15607	13267	5.3118	36.533	7.0112
63096	0.16309	9905.7	4.6905	28.044	5.5152
100000	0.17134	7651.6	4.0252	21.363	4.3481
158490	0.18179	6067.2	3.3983	16.114	3.428
251190	0.19596	4870.7	2.8791	12.021	2.6898
398110	0.21582	3884.7	2.5085	8.8823	2.0854
630960	0.24314	3017.4	2.2956	6.5349	1.5875
1e+06	0.27823	2251.4	2.2215	4.8203	1.1867
1.5849e+06	0.31946	1611.9	2.2477	3.5819	0.87757
2.5119e+06	0.36429	1120.3	2.3271	2.683	0.64825
3.9811e+06	0.41089	768.96	2.4127	2.0208	0.48145
6.3096e+06	0.4587	529.92	2.466	1.5256	0.36046
1e+07	0.50808	371.15	2.4608	1.1509	0.27216

Table XIIB. Dielectric parameters for liver in the frequency domain from 10 Hz to 10 MHz.

Frequency [Hz]	Conductivity [S/m]	Relative permittivity	Loss tangent	Wavelength [m]	Penetration depth [m]
10	0.027714	1.5056e+07	3.3087	5175.8	1109.5
15.849	0.031215	9.2948e+06	3.8089	3948.6	814.72
25.119	0.03406	5.055e+06	4.8218	3084.3	603.13
39.811	0.035996	2.574e+06	6.3144	2441.3	454.92
63.096	0.037256	1.2993e+06	8.1691	1940.4	348.93
100	0.03813	678470	10.102	1541.3	270.8
158.49	0.038811	377810	11.651	1221.5	211.81
251.19	0.039409	228850	12.323	965.16	166.58
398.11	0.039991	152000	11.88	759.9	131.55
630.96	0.04062	110150	10.506	595.64	104.25
1000	0.04138	85673	8.6821	464.13	82.866
1584.9	0.04241	69802	6.8911	358.8	65.99
2511.9	0.043928	57911	5.4283	274.69	52.508
3981.1	0.046199	47560	4.386	208.25	41.552
6309.6	0.049407	37825	3.7213	156.83	32.553
10000	0.053495	28930	3.3239	117.88	25.237
15849	0.058193	21542	3.0638	88.693	19.456
25119	0.063288	16007	2.8294	66.696	15.01
39811	0.068906	12133	2.5643	49.911	11.624
63096	0.075638	9454.4	2.2792	36.997	9.0136
100000	0.084568	7498.9	2.0272	27.114	6.9407
158490	0.097101	5918.1	1.8609	19.71	5.2469
251190	0.11433	4527.9	1.8069	14.327	3.8681
398110	0.1361	3300.4	1.862	10.506	2.7959
630960	0.16085	2290.5	2.0006	7.8041	2.0094
1e+06	0.18665	1535.7	2.1848	5.865	1.4538
1.5849e+06	0.21236	1015.1	2.3727	4.4407	1.0648
2.5119e+06	0.23779	673.55	2.5264	3.3733	0.7899
3.9811e+06	0.2633	454.23	2.6173	2.5627	0.59247
6.3096e+06	0.28943	313.77	2.6279	1.943	0.44854
1e+07	0.31671	223.12	2.5516	1.4676	0.34241

Table XIIB. Dielectric parameters for lung in the frequency domain from 10 Hz to 10 MHz.

Frequency [Hz]	Conductivity [S/m]	Relative permittivity	Loss tangent	Wavelength [m]	Penetration depth [m]
10	0.20279	5.4971e+06	66.312	2203.9	356.1
15.849	0.20399	3.3425e+06	69.219	1746	281.93
25.119	0.20484	1.86e+06	78.807	1385.3	223.29
39.811	0.20531	1.0807e+06	85.777	1099.7	177.07
63.096	0.2056	724840	80.808	872.57	140.6
100	0.20588	567080	65.261	691.61	111.77
158.49	0.20635	489090	47.851	547.22	88.931
251.19	0.20723	436230	33.995	431.9	70.791
398.11	0.20887	383740	24.576	339.8	56.327
630.96	0.21162	321940	18.727	266.46	44.733
1000	0.21567	252050	15.381	208.45	35.402
1584.9	0.22078	183070	13.678	162.99	27.906
2511.9	0.22642	124820	12.981	127.59	21.932
3981.1	0.2321	81752	12.819	100.05	17.215
6309.6	0.23759	52691	12.846	78.559	13.514
10000	0.2429	34044	12.826	61.711	10.617
15849	0.24816	22305	12.618	48.466	8.3491
25119	0.2535	14912	12.166	38.034	6.5714
39811	0.25907	10202	11.467	29.811	5.1763
63096	0.26504	7153.5	10.555	23.324	4.0804
100000	0.27161	5145.3	9.4891	18.204	3.2187
158490	0.27914	3793.8	8.3452	14.162	2.5402
251190	0.28825	2855	7.2249	10.969	2.004
398110	0.2999	2166.9	6.2493	8.4509	1.5773
630960	0.31521	1622.9	5.5334	6.4813	1.2347
1e+06	0.33438	1170.5	5.1351	4.9642	0.95879
1.5849e+06	0.35586	806.15	5.0066	3.813	0.74006
2.5119e+06	0.37743	539.91	5.0026	2.9407	0.57085
3.9811e+06	0.39805	362.71	4.9551	2.2725	0.44195
6.3096e+06	0.41799	250.57	4.7524	1.7541	0.34403
1e+07	0.43799	180.32	4.3661	1.3488	0.2694

## APPENDIX C

### BIOLOGICAL VARIABILITY STUDY

On the biological variability of the kidney tissue reflected in the key parameters of the fresh and irradiated samples.

As already explain in detail in the data analysis section, we tried to alleviate the problem of the biological variability by using pair organs (or multiple lobes). Even though the kidney tissue used in the measurement on the excised tissue and of the radiation-induced effects was harvested from the same animal, we encountered problems normalizing or comparing different tissues. Similar problems were encountered for other tissues: the heart was particularly difficult as the only unpaired organ studied, but we also have problems with lung tissue, who's dielectric properties seems to scale with its size. We already emphasized the fact that this study doesn't attempt to establish any *absolute* values in terms of what a normal response (in time or magnitude) of a given tissue would be to radiation. Instead, we are trying to find certain patterns, or trends, and then measure and interpret the *relative* changes in the dielectric properties, after the radiation exposure, relative to "before".

It was suggested that we would present a study to confirm the trends for a given type of tissue (organ) in the presence of biological variability. Such analysis and especially its graphical representation is extremely cumbersome. We are presenting in the next four graphs the evolution of two key parameters  $R_1$  and  $C_1$  of the model used for kidney (see Figure 48 in Chapter VI), for the freshly excised samples as well as for the irradiation with 6 MV photon beam of excised kidney tissue. The samples were collected from 7 animals over a time interval of several months. The samples labeled with the same number in the non-irradiated and irradiated group are in fact two kidney lobes coming from the same animal.

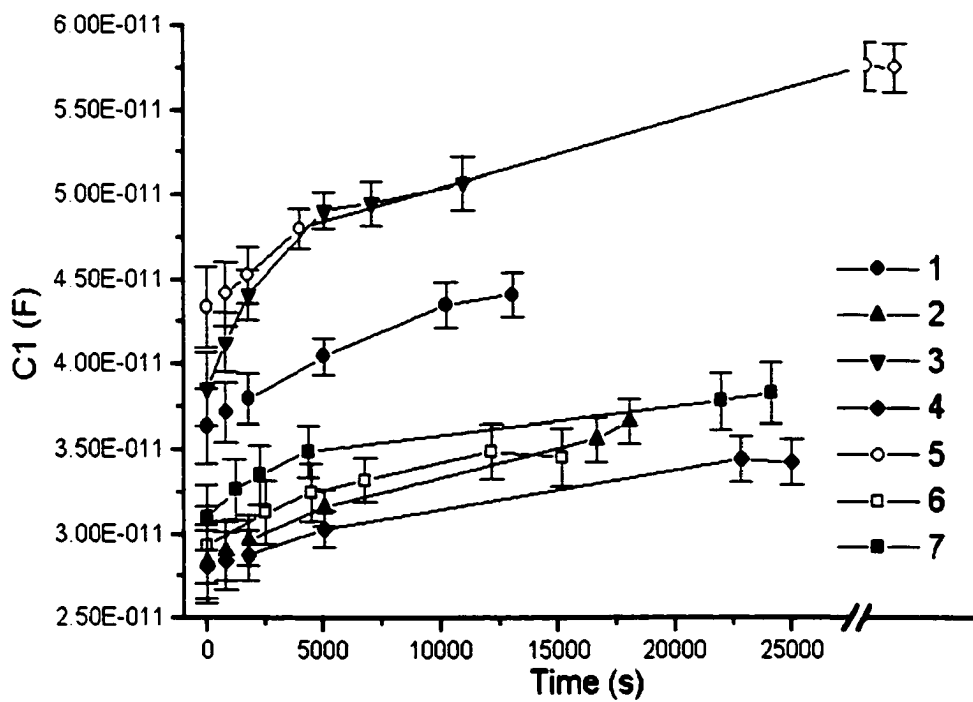


Figure 94C. Parameter  $C_1$  of the equivalent model circuit used for freshly excised kidney tissue.

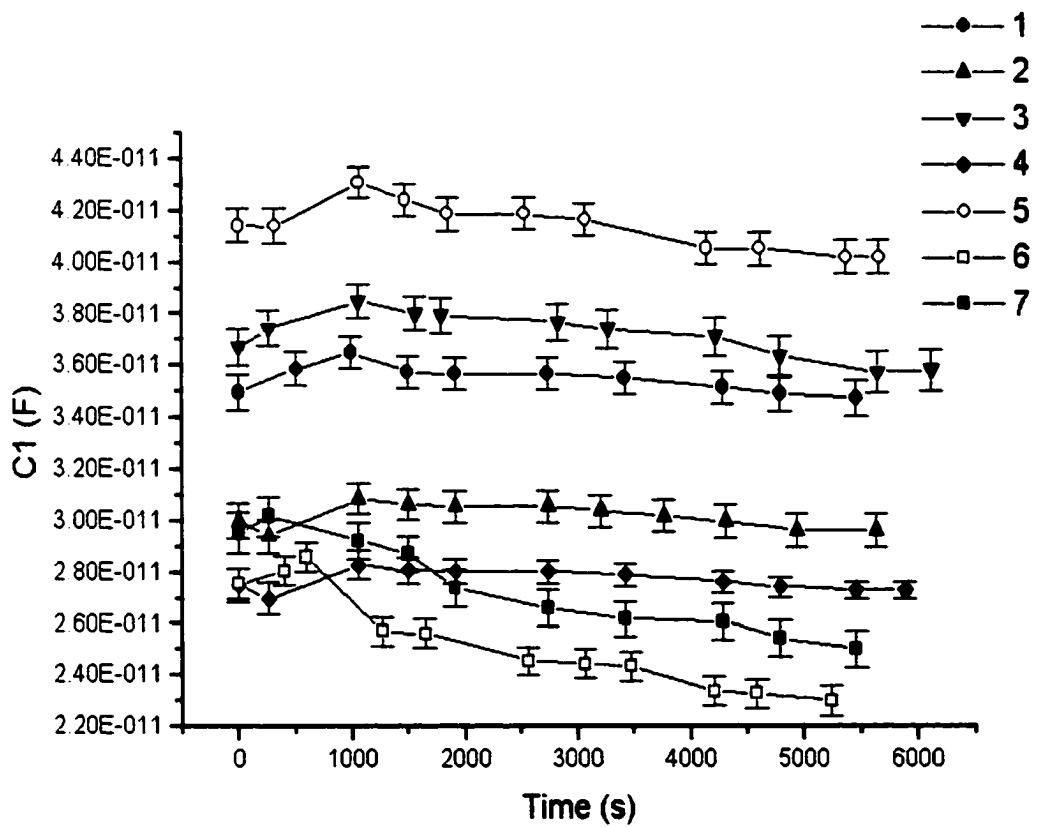


Figure 95C. Parameter  $C_1$  of the equivalent model circuit used for irradiated kidney tissue. Equal doses of 10.1 Gy were delivered before measurements no. 3, 6 and 9



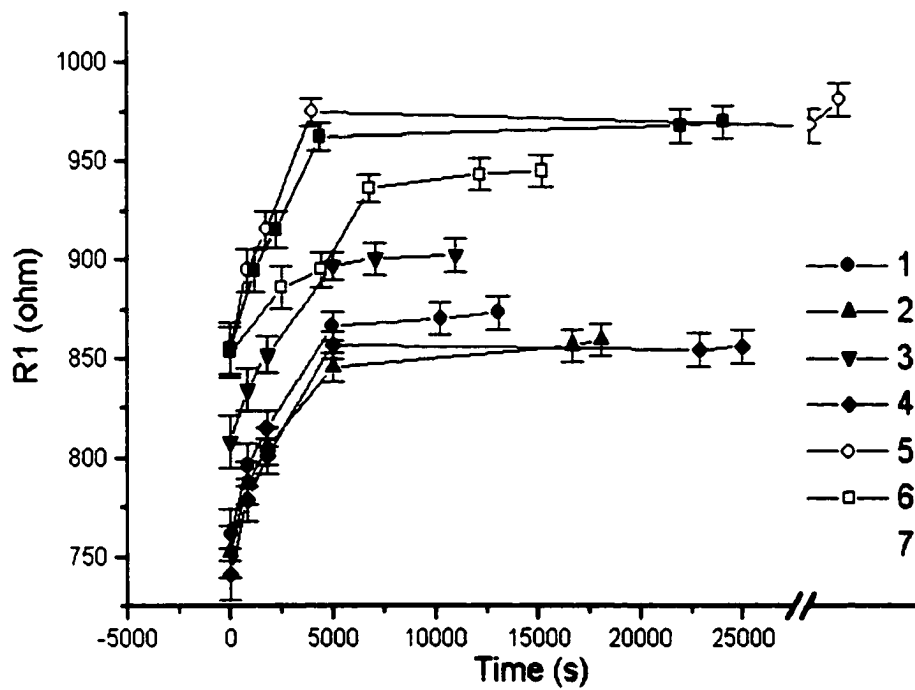


Figure 96C. Parameter  $R_1$  of the equivalent model circuit used for freshly excised kidney tissue.

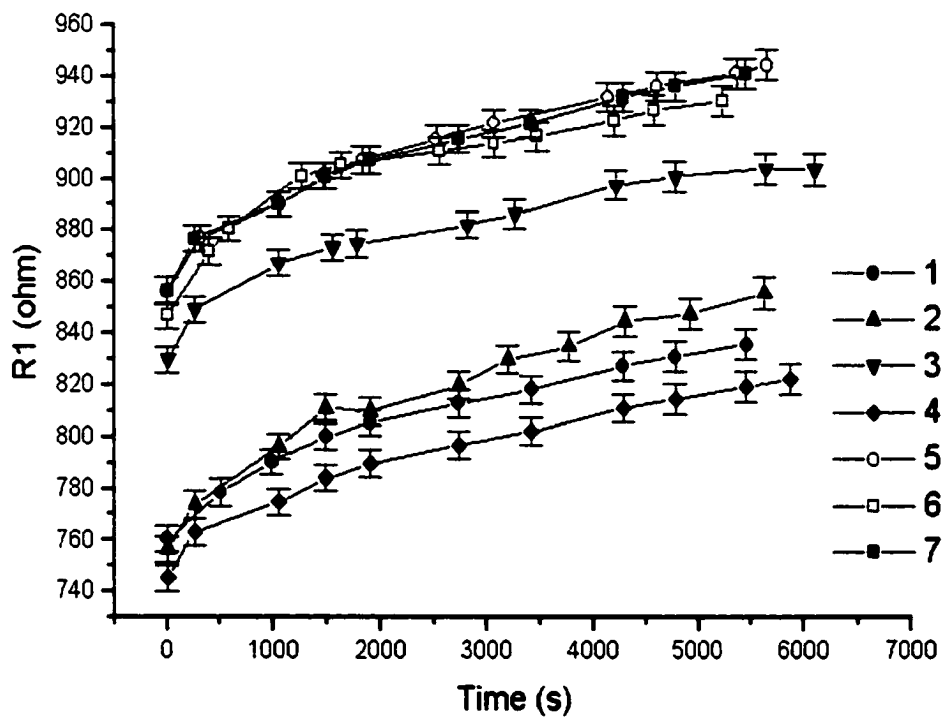


Figure 97C. Parameter  $R_1$  of the equivalent model circuit used for irradiated kidney tissue.

## VITA

**Date and Place of Birth:** December 18, 1961, Alba-Iulia, Romania.

**Address:** Old Dominion University, Department of Physics, 4600 Elkhorn Avenue, Norfolk, VA 23529.

### Education

- 1995-2000     Doctoral studies with the Department of Physics at Old Dominion University in Norfolk, Virginia.
- 1993, 1994     Research stages within the frame of European Communities Concerted Actions, MATFORSK Institute, Ås, Norway.
- 1992, 1994     College on Medical Physics - International Center for Theoretical Physics, Trieste, Italy.
- 1981-1986     B.S. Faculty of Physics, University of Bucharest - Romania.  
Specialization in Automation, Control and Measurement Techniques.

### Professional Memberships

American Physical Society (APS),  
Institute of Electrical and Electronics Engineers (IEEE),  
IEEE Engineering in Medicine and Biology Society,  
IEEE Computer Society,

### Recent Publications and Presentations

**Non-invasive Method for Tissue Response Detection to Ionizing Radiation Treatment**, D. Todor, G. Copeland, R. Wu, to be published in *IEEE Engineering in Medicine and Biology Society Magazine*, proceedings of the XX-th IEEE-EMBS Conference, Atlanta, 25-29 October, 1999.

**Monitoring Dielectric Properties in Tissue - A Possible Paradigm Shift in Radiation Therapy?** D. Todor, R. Wu, G. Copeland, in *Medical Physics*, August issue, 1999, dedicated to the 41st Annual Meeting of the American Association of Physicists in Medicine (AAPM), July 25-29, 1999.

**Novel Method for in -Vivo Detection of Tissue Response to Radiation**, D. Todor, G. Copeland, R. Wu, in proceedings of the American Physical Society Centennial Meeting, Atlanta, GA, March 20-26, 1999.

**Dielectric Methods for the detection of Tissue Response to Radiation**, D. Todor, G. Copeland, in *Critical Reviews<sup>TM</sup> in Biomedical Engineering*, Vol. 26, No 5&6, 1998.

**Electrical Impedance Tomography: An Improved Model For Solving The Forward Problem**, D. Todor, G. Copeland, L. Cheran, *Physica Medica*, Vol 13, No. 1, p.358-61, Dec. 1997.

**Linear Prediction and Singular Value Decomposition in NMR Signal Analysis**, M. Lupu, D. Todor, Chapter 8 in *Signal Treatment and Signal Analysis in NMR* edited by D. N. Rutledge; Elsevier Science Publishers, 1996.